

Beam Loss Patterns at the LHC Collimators

—

Measurements & Simulations



Master Thesis

By Till Tobias Böhlen

Supervisors:

Prof. Dr. Norbert Pietralla

Institut für Kernphysik

Technische Universität Darmstadt

Dr. Bernd Dehning & Dr. Rüdiger Schmidt

CERN AB-BI-BL, Geneva

Email: Till.Tobias.Bohlen@cern.ch

October 2007 – September 2008



Abstract

The Beam Loss Monitoring (BLM) system of the Large Hadron Collider (LHC) detects particle losses of circulating beams and initiates an emergency extraction of the beam in case that the BLM thresholds are exceeded. This protection is required as energy deposition in the accelerator equipment due to secondary shower particles can reach critical levels; causing damage to the beam-line components and quenches of superconducting magnets.

Robust and movable beam line elements, so-called collimators, are the aperture limitations of the LHC. Consequently, they are exposed to the excess of lost beam particles and their showers. Proton loss patterns at LHC collimators have to be determined to interpret the signal of the BLM detectors and to set adequate BLM thresholds for the protection of collimators and other equipment in case of unacceptably increased loss rates.

The first part of this work investigates the agreement of BLM detector measurements with simulations for an LHC-like collimation setup. The setup consists of one LHC collimator and three LHC BLM detectors mounted in the Super Proton Synchrotron (SPS). The geometry is modeled in the Monte Carlo particle code FLUKA. The impact scenario of the beam during the measurements is determined for simulations, and the measured BLM detector signals are compared with the simulated signals. This procedure results in a determination of an overall accuracy for the prediction of the BLM signals, and thus also for the prediction of BLM thresholds, by simulations. It includes an assessment of BLM-signal deviation due to simplifications and misalignment of the geometry in the simulation, physics parameters of the simulation, and uncertainties for the beam impact scenario. At the same time this study is an integral check for the BLM electronics and the data acquisition system. The relative agreement of measurements and simulations ranges between 20% and 70%, depending on the detector type.

The second part of this work is devoted to the prediction of BLM detector signals for the actual LHC collimation geometry and a larger set of collimator types. Again, FLUKA was employed as simulation tool. The relation between the BLM signals and energy deposition in the collimators – as the crucial scaling variable for damage to the collimators – is investigated. The study focuses on the variation of the BLM signals and the BLM signal-to-energy deposition ratio due to misalignment, and different beam impact scenarios. It results in ratios of BLM signal to energy deposition in the collimator which allow to predict BLM thresholds at collimators for given damage limits of the collimators.

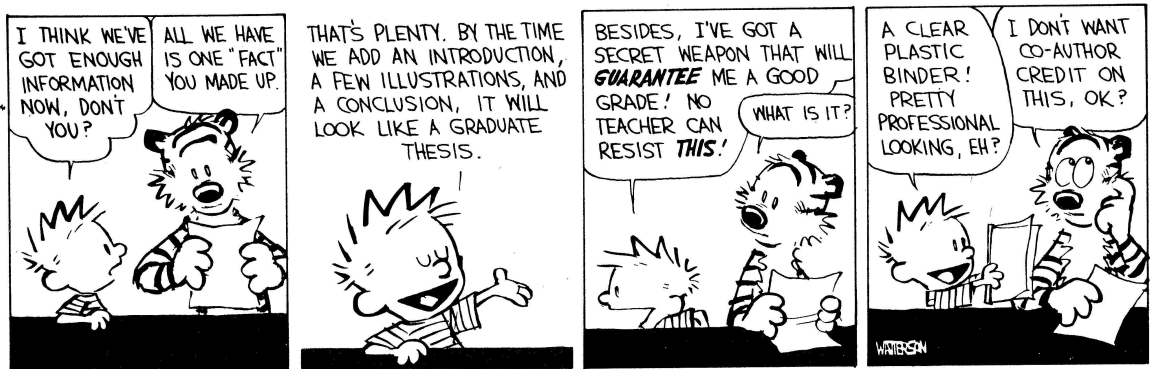
Kurzfassung

Strahlverluste des Large Hadron Colliders (LHC) werden von dem Beam Loss Monitoring (BLM) System observiert. Im Falle von überschrittenen BLM-Grenzwerten initiiert das BLM-System eine sichere Strahlextraktion zum Schutz der Beschleunigerkomponenten. Dieser Schutz ist vonnöten, da die Energiedeposition von sekundären Schauerteilchen kritische Werte erreichen kann, welche eine Beschädigung der LHC-Bestandteile verursachen oder zum Quenchen von supraleitenden Magneten führt.

Kollimatoren sind robuste und bewegliche Elemente der LHC-Strahlführung, welche die Aperturlimitationen des Beschleunigers bilden. Durch ihre exponierte Lage sind Kollimatoren dem Großteil der verlorenen Strahlteilchen und deren Schauern ausgesetzt. Die Struktur von Strahlverlusten an den LHC-Kollimatoren muss bestimmt werden, um das Signal der BLM-Detektoren interpretieren zu können und daraufhin angemessene BLM-Grenzwerte zum Schutz der Kollimatoren und anderer LHC-Apparatur zu setzen.

Der erste Teil dieser Arbeit vergleicht die Messungen von BLM-Detektoren mit Simulationen für einen Aufbau, welcher der LHC-Installation gleicht. Der experimentelle Aufbau besteht aus einem LHC-Kollimator und drei BLM-Detektoren, die im Super Proton Synchrotron (SPS) aufgestellt sind. Die Geometrie ist in dem Monte Carlo Teilchen Code FLUKA modelliert. Das Strahlimpaktszenario während der Messungen wird für die Simulationen rekonstruiert und die gemessenen BLM-Detektor Signale werden mit den simulierten Detektor Signalen verglichen. Dieser Vergleich gibt ein Maß für die generelle Genauigkeit der Vorhersage von BLM-Detektor Signalen – und damit auch der Bestimmung von BLM-Grenzwerten – durch Simulationen. Die Studie beinhaltet eine Abschätzung der Fehler der Simulation, die durch die Vereinfachung der Geometrie, die Fehlausrichtung der Komponenten und den Unsicherheiten des genauen Strahlimpaktszenarios hervorgerufen werden. Außerdem ist die Studie ein integraler Test für die BLM-Elektronik und das BLM-Daten Akquisitionssystem. Die relative Übereinstimmung zwischen Messung und Simulation ist zwischen 20% und 70%, abhängig von dem Typ des BLM-Detektors.

Der zweite Teil dieser Thesis bestimmt BLM-Detektor Signale für die LHC Kollimationsgeometrie für verschiedene Typen von Kollimatoren. FLUKA wurde wieder für die Simulationen benutzt. Das Verhältnis zwischen BLM-Signalen und der Energiedeposition in den Kollimatoren – als aussagekräftige Größe für die Schadensgrenze der Kollimatoren – wird untersucht. Im Besonderen beschäftigt sich die Studie mit der Variation von BLM-Signalen und dem Verhältnis von BLM-Signal zu Energiedeposition in dem Kollimator aufgrund von Fehlausrichtung und unterschiedlichen Strahlimpaktszenarien. Das Ergebnis sind Verhältnisse von BLM-Signal zu Energiedeposition, die es zusammen mit gegebenen Schadensgrenzen für die Kollimatoren ermöglichen BLM-Grenzwerte an Kollimatoren abzuschätzen.



by Bill Watterson

Acknowledgment

First of all, I would like to thank my supervisor, Dr. Bernd Dehning, for detailed discussions, for his helpful and constructive instructions on the topic, and for his marvelous just-in-time management – which made me from time to time a little nervous, but always worked out in the end. Moreover, with his accurate corrections he probably used up three CERN pens (all four colors!) correcting my print-outs. Thanks!

Further, I want to thank my second supervisor, Dr. Rüdiger Schmidt, which was my initial link to CERN. He took much interest in the progress of this thesis, motivated, and was always there for a MIGROS-discussion session during lunch time.

I am grateful to my university supervisor, Prof. Dr. Norbert Pietralla, for the flexible and uncomplicated way of dealing with his “outpost student”, being 600 km away, and for making this master thesis possible.

I want to thank the FLUKA team for the introduction to their code and for their cooperation, providing some detailed geometry models. Special thanks goes to Markus Brugger for advice and helping along the year with smaller and bigger peculiarities of FLUKA.

Thanks as well to the Collimation team, in particular Stefano Redaelli and Thomas Weiler, for operation of the collimators and useful discussions.

Of course, I want to thank all people from CERN who have contributed to the completion of this thesis with advice, discussion, and encouragement.

Further, I am grateful to all those who have read these pages and commented upon them, especially, Rüdiger, Markus, Aurélien, Stefano, and Zoë.

I would like to thank the BLM team for the harmonious working atmosphere and countless coffee. It was a pleasure working with them!

Special thanks goes to my 865-1-B01 office mates, Aurélien Marsili, Daniel Kramer, and Dariusz Bocian, for enriching this thesis with technical discussion on the topic, for discussions just about everything off the topic (especially tea), and for enabling me to enter in advanced spheres of “office dart warfare”, assuring always a certain tension when entering the room. Further, it was a great mental support in the last days being not the only stressed guy in this office writing a thesis.

My deep gratitude belongs to the girl which triggered the thought about going to CERN in the first place. She makes me wonder and learn – again and again – what is possible in life. It was a wonderful year here. Gracias Ilaria.

Last, I want to thank my parents for supporting me during my studies, taking so much interest in them, encouraging me in what I am doing, and always being there for me.

Contents

Introduction	1
1. The Large Hadron Collider and its Protection Systems	3
1.1. The Ring and its Experiments	3
1.1.1. General Layout	3
1.1.2. Experiments	3
1.1.3. Preaccelerator Chain	5
1.2. Protection System for the LHC	6
1.2.1. Collimation System	7
1.2.2. Beam Loss Monitoring System	11
2. Particle–Matter Interaction	13
2.1. Probability of Interaction	14
2.2. Energy Loss due to Electromagnetic Processes	15
2.3. Multiple Coulomb Scattering	17
2.4. Nucleon-Nucleon Interactions	18
2.5. Electromagnetic Showers	18
2.6. Hadronic Showers	19
3. Simulation Techniques for Particle-Matter Interaction	21
3.1. Structure of a Particle Transport Code	21
3.2. Modeling of Particle Interactions	22
3.3. Introduction to FLUKA – a Multi-Purpose Monte Carlo Particle Code	23
3.3.1. Physics of FLUKA	24
3.3.2. Biasing Techniques and Particle Thresholds	24
4. Technical Implementation of the Beam Loss Monitoring System	26
4.1. Principles of Ionization Chambers	26
4.2. Principles of Secondary Electron Emission Detectors	27
4.3. Detectors and Electronics of the BLM System	27
5. Beam Losses at the LHC Collimator mounted in the SPS	33
5.1. Description of the Experimental Setup	33
5.2. Preparation of the Simulation	34
5.2.1. Implementation of Geometry and Materials	34
5.2.2. Recorded Quantities	36
5.2.3. Returning Beam Protons	36
5.2.4. Monte Carlo Statistics, FLUKA Physics Settings, and Biasing	38
5.2.5. Variation Studies	38

Contents

5.2.6.	Impact Parameter Scan at 26 GeV	39
5.2.7.	Particle Spectra in the BLM Detectors	40
5.3.	Measurements	40
5.3.1.	SPS Beam Conditions and Acquired Data	40
5.3.2.	Overview of Data Analysis	41
5.3.3.	Calculation of the Beam Profile at the Collimator with a Wire Scanner	44
5.3.4.	Measuring of the Horizontal Beam Profile by Scraping	46
5.3.5.	Calibration and Uncertainties of the Beam Impact Parameter	49
5.3.6.	Impact Parameters for Continuous Scraping	51
5.3.7.	Normalized Detector Signal for Direct Dumping	56
5.3.8.	Normalized Detector Signal for Continuous Scraping	58
5.4.	Evaluation of the Simulation	60
5.4.1.	Simulation of Direct Dumping	60
5.4.2.	Simulation of Continuous Scraping	61
5.5.	Comparing Measurements with Simulations – Results from the SPS Experiment	63
6.	Simulations for the LHC Collimation Setup	64
6.1.	Shower Cross-talks	64
6.2.	Modeling Approach	65
6.3.	Preparation of the Simulation	65
6.3.1.	Implementation of Geometry and Materials	65
6.3.2.	Recorded Quantities	66
6.3.3.	Monte Carlo Statistics, FLUKA Physics Settings, and Biasing	66
6.3.4.	Variation Studies	66
6.3.5.	Particle Spectra in the BLM Detectors	67
6.3.6.	Comparison with the SPS Simulations and the IR7 Implementation	68
6.4.	Predictions of BLM Signals	68
6.4.1.	BLM Signal Changes due to Different Cell Geometries	70
6.4.2.	Scan of the Impact Parameter	70
6.4.3.	Scan of the Beam-Jaw Angle	73
6.4.4.	Peak Energy Deposition	74
6.4.5.	Secondary and Higher Order Particle Halos	74
6.5.	Results	76
6.5.1.	Example of a BLM Threshold Value Calculation	76
	Conclusions	78
	A. Acronyms	81
	B. Hadronic and Intra Nuclear Interactions	83
	C. Random Numbers	86
	D. Gaussian Distributions	88
	E. Collimator Positions in the LHC Ring	89
	F. Conversion of the BLM Detector Signals	90

Contents

G. Beam Optics and TWISS Functions	91
H. Beam Profile by Scraping: Dispersive Case	93

Introduction

The Large Hadron Collider (LHC), constructed at CERN (European Organization for Nuclear Research near Geneva, Switzerland), is the world's most advanced particle physics instrument. With a maximum envisaged beam energy of 7 TeV it surpasses existing accelerators by a factor of seven. Its envisaged nominal beam intensity is by a factor of about 30 higher than other operating colliders. For the guidance of the beam particles superconducting magnets at cryogenic temperatures are used.

Each of the two counter-circulating proton beams of the LHC is designed to store an energy of 362 MJ. Small fractions of the circulating particles impacting at machine apertures can cause superconducting magnets to undergo a transition from the superconducting state to the normal conducting state, commonly referred to as quenching. Moreover, particle losses can result in severe damage to sensitive equipment. Thus, to ensure safe operation of the LHC up to nominal intensities, a sophisticated protection system for its machine components is needed [Sch06].

Requirements for the safe operation necessitate the early detection of failures within the equipment, and an active surveillance of beam losses throughout the ring. The latter is mainly accomplished by the Beam Loss Monitoring (BLM) system, detecting increased loss rates in crucial positions close to sensitive LHC machinery.

The BLM detectors measure the energy deposition by secondary particle showers which are induced by lost beam particles. The correlation between the energy deposited in sensitive LHC components, corresponding to a temperature increase, and the signal seen by the BLM detectors, installed along the ring, enables to set individual thresholds for the BLM detectors in order to protect the machinery. When the signal of the detectors exceeds the thresholds of the BLM system, an extraction of the beam is triggered. The BLM detectors mounted in the LHC are mainly installed outside the cryostats of the magnets and in the two "collimation insertions" of the LHC ring. Robust and movable beam-pipe elements installed in these insertions, the so-called collimators, define with their jaws the minimal aperture of the LHC ring. Thus, they see the excess of lost beam protons. There are many failure scenarios that can lead to beam loss and damage. Depending on the type of failure, the scenario of impact on the collimator can vary considerably.

This thesis investigates the energy deposition of beam losses on LHC collimators and the corresponding BLM detector signals. For the modeling of particle showers in the relevant beam line geometries the multi-purpose Monte Carlo cascade code FLUKA [Fas03, Fas05] was chosen.

The first part of this work determines the accuracy of predicting BLM detector signals in collimation regions by simulations. To do so, it compares simulations of the BLM detectors to experimental data acquired from an LHC-like setting mounted in the Super Proton Synchrotron (SPS) tunnel. This facilitates the determination of systematic errors made when calibrating BLM thresholds by simulations. At the same time, it is a check for the BLM detection system in an LHC-like condition.

Introduction

In the second part of the thesis, FLUKA simulations with the actual LHC collimation geometry¹ study relations between energy deposition in the collimator, as a crucial value for damage limits, and signal seen by the BLM detectors. Both peak energy deposition and total energy deposition in the collimator are considered. The variation of these ratios for different scenarios, such as particle impact depth in the collimator jaw, and misalignment of components, is investigated. This is done for an isolated collimator-BLM detector cell with the collimator types from the LHC cleaning insertions² in different positions (horizontal, vertical, skew). These simulations aim to assess BLM threshold settings for the LHC collimators.

- ★ Chapter 1 provides an introductory summary of the essential features of the LHC, its experiments, and its protection systems.
- ★ Chapter 2 presents an overview on particle interaction with matter with a focus on relevant physical processes for the description of the LHC collimation setup. Some general features of particle showers are described.
- ★ Chapter 3 explains fundamentals of Monte Carlo simulations and sketches its application in high-energy physics. Further on, it gives some details about the Monte Carlo particle code FLUKA.
- ★ Chapter 4 is devoted to the description of particle detectors employed for the BLM system and the general setup of the system itself with a special regard to the electronic implementation of the acquisition system.
- ★ The first part of Chapter 5 presents the experimental setup in the SPS, its implementation in FLUKA, including a sensitivity study for not precisely known variables, the measurements and their analysis. The second part of Chapter 5 is dedicated to the evaluation of the simulation, a comparison with the experimental data, and finally, the results.
- ★ In Chapter 6, the geometric implementation and simulations of the LHC setup are presented. The simulations are compared to the SPS setup of the previous chapter and simulations done by the FLUKA team for the betatron cleaning insertion [Mag06]. In the end, relations between energy deposition and detector signals leading to BLM thresholds are presented and discussed.
- ★ Finally, the last chapter states conclusions.

¹LHC cleaning insertions IR3 and IR7

²Internal collimator names: TCP, TCSG, TCLA

1. The Large Hadron Collider and its Protection Systems

1.1. The Ring and its Experiments

The Large Hadron Collider (LHC), being constructed at CERN, is a proton collider with an injection energy of 450 GeV and a collision (top) energy of 7 TeV. It is designed to provide primarily proton-proton (pp) collisions at 14 TeV center-of-mass energy and a peak luminosity of $\mathcal{L}^* = 1 \cdot 10^{34} \text{ cm}^{-2}\text{s}^{-1}$. Operation with ion-ion collisions (initially Pb) is also foreseen.

1.1.1. General Layout

The collider itself consists of two storage rings, mounted in the former tunnel of the Large Electron Positron (LEP) collider. Each of these interleaved rings has a circumference of 26.7 km. The counter-circulating beams will be brought to collision at four crossing points, each dedicated to a particle detector experiment, see Fig. 1.1. The LHC consists of eight straight insertion regions (IR's) and eight bending sections (arcs), see Fig. 1.1. The experiments are located at IR 1, 2, 5, and 8. IR 3 and 7 are devoted to the “cleaning” of the beam. The beam dump and radio-frequency (RF) cavities are located in IR 6 and 4, respectively. Each arc is composed of 46 regular “half-cells” consisting themselves of three 14.3 m dipoles magnets (MB), one 3.1 m quadrupole magnet (MQ), and several small corrector and tuning magnets.

Having the bending radius of the LHC predefined by the geometry of the LEP tunnel, the limiting factor for achievable collision energy is the technically feasible magnetic field strength of the dipole magnets. 1232 superconducting main dipole magnets with a nominal field of 8.3 T (operating at a current of 12 kA) are required in the LHC to guide a 7 TeV proton beam through the tunnel. There are about 8000 superconducting Nb-Ti magnets installed in the LHC operating in super-fluid helium at 1.9 K and 4.5 K, depending on the type. They are grouped in 1700 electric powering circuits. The nominal separation of the two counter-circulating beams is only 194 mm. Twin-aperture magnets provide anti-parallel fields to guide the beams. The total amount of energy stored in the magnetic system is about 10 GJ [Sch06]. Tab. 1.1 summarizes some of the LHC beam parameters.

1.1.2. Experiments

The biggest experiments, ATLAS (A Toroidal LHC Apparatus) and CMS (Compact Muon Solenoid) are two high-luminosity pp collision detectors. The primary goal of these detectors is the discovery of the Higgs boson. This particle is postulated within the scope of the standard model to explain the mass of different particles.

ALICE (A Large Ion Collider Experiment) focuses on the physics of strongly interacting matter at high energy densities. By colliding fully-stripped lead ions at an energy of 1150 TeV, corresponding to 2.76 TeV/u, and a luminosity of more than $10^{27} \text{ cm}^{-2}\text{s}^{-1}$ one expects to enter

1. The Large Hadron Collider and its Protection Systems

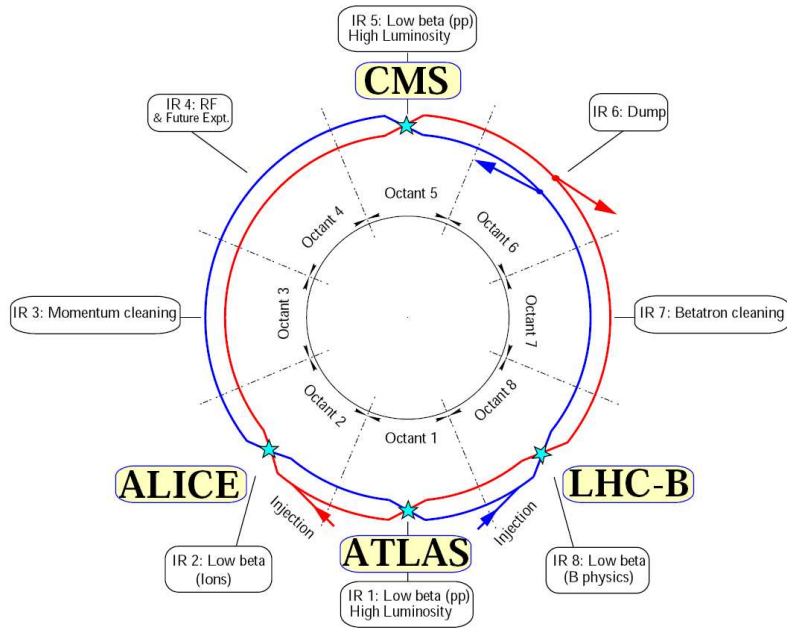


Fig. 1.1.: Overview of the LHC layout. The LHC is divided in octants (IR1-8) each containing a straight section primarily dedicated to one task, e.g. collimation, experiment. The LHC detector experiments are located in the four crossing points of the counter-circulating beams.

LHC parameter	Unit	Injection	Collision
General beam data			
Proton energy	GeV	450	7000
Relativistic gamma γ_L		479.6	7461
Revolution frequency	kHz	11.246	
No. of particles per bunch		$1.15 \cdot 10^{11}$	
No. of bunches		2808	
Longitudinal emittance (4σ)	eVs	1.0	2.5
Transverse normalized emittance (1σ)	$\mu\text{m rad}$	3.5^a	3.75
Circulating beam current	A	0.582	
Stored energy per beam	MJ	23.3	362
rms bunch length ^b	cm	11.24	7.55
Specific for crossing points in IR1 and IR5			
rms beam size ^c	μm	375.2	16.7
Total crossing angle	μrad	-	285
Peak luminosity	$\text{cm}^{-2}\text{sec}^{-1}$	-	$1.0 \cdot 10^{34}$

a: emittance delivered by the SPS

b: assuming a Gaussian distribution

c: assuming a β -function of 0.55 m

Tab. 1.1.: LHC beam parameters as crucial for the peak luminosity, adapted from [LHC03].

1. The Large Hadron Collider and its Protection Systems

in the regime of a quark-gluon plasma. This phase might have existed 10^{-6} s after the Big Bang.

Finally, the LHC-b (LHC Beauty Experiment) detector is suited for a precise study of the CP violation and rare decays.

1.1.3. Preaccelerator Chain

The preaccelerator chain, injecting finally in the LHC, is starting for protons at LINAC2 (Linear Accelerator) and for ions at LINAC3, see Fig. 1.2. These roughly 80 m-long LINAC's accelerate particles up to an energy of 50 MeV per charge and inject in the PSB (Proton Synchrotron Booster, circumference of about 157 m) or the LEIR (Low Energy Ions Ring) for protons and ions, respectively. Protons are accelerated to an energy of 1.4 GeV and are then fed into the PS (Proton Synchrotron, circumference of 628 m). Here the acceleration chain of protons and ions are joined. In the PS the energy of the protons is increased further to 26 GeV and the final LHC beam structure of bunches with 25 ns-spacing is formed. It extracts into the SPS (with a circumference of 7 km) where the protons are finally accelerated to the injection energy of the LHC. Both LHC rings are filled via the injection lines TT2 and TT8 by the SPS. Each LHC ring is filled by several SPS bunch trains.

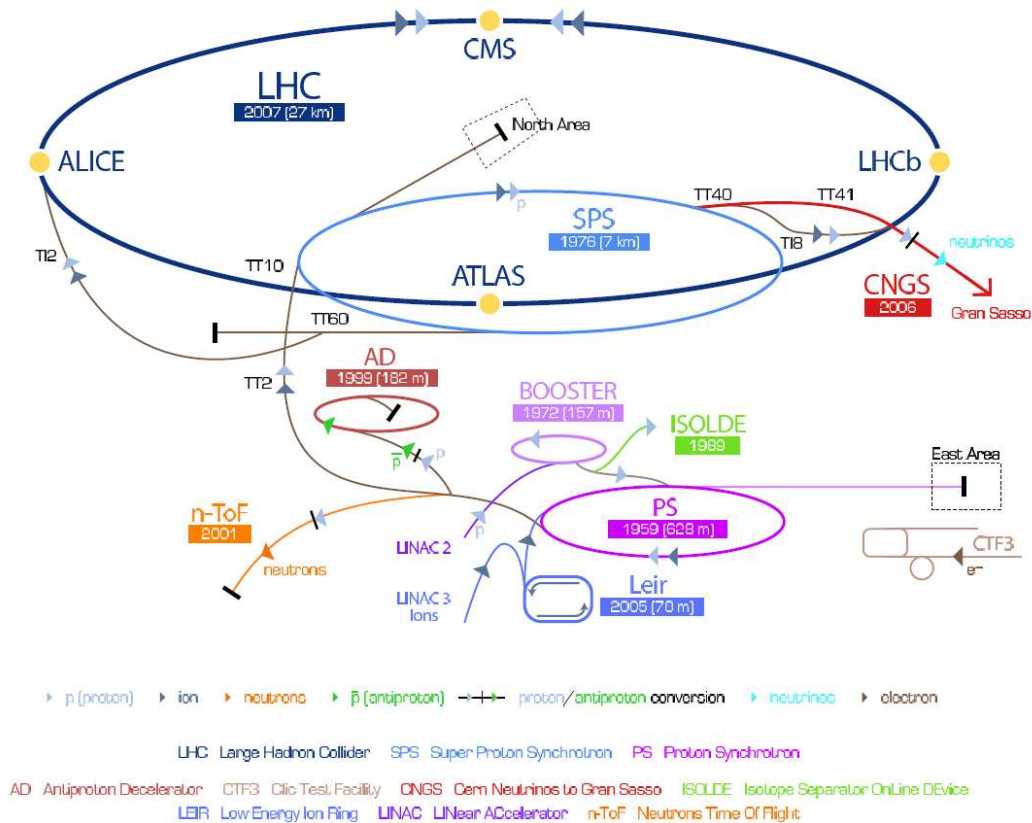


Fig. 1.2.: Overview of the CERN accelerator complex.

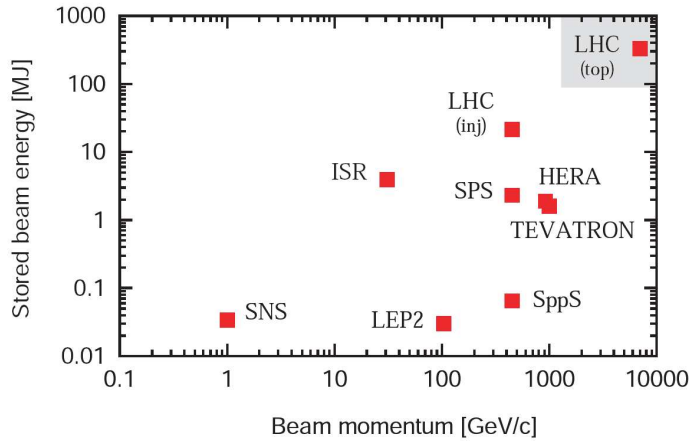


Fig. 1.3.: Comparison of accelerators in terms of beam momentum and stored beam energy, taken from [Ass06].

1.2. Protection System for the LHC

The nominal beam parameters of the LHC will exceed those of currently operating accelerators – often by orders of magnitude. The energy of 362 MJ per beam stored in the LHC at nominal conditions is by a factor of about 200 higher than other existing hadron machines (TEVATRON, RHIC, HERA), see Fig. 1.3. It is sufficient to melt about 500 kg of copper. How harmful an accelerator beam can potentially be is measured by its transverse energy density. With a maximum energy density of $1 \text{ GJ}/\text{mm}^2$, the LHC exceeds currently operating accelerators by a factor of 1000.

Accidental beam losses can lead to severe damage and long downtimes of the LHC. As rough estimation, a one-turn loss of $3 \cdot 10^{-9}$ times the nominal beam intensity can quench a superconducting magnet and a one-turn loss of three to four orders of magnitude more can even damage the LHC components. As a consequence, there is the need for a sophisticated protection system to operate the LHC safely. Energy deposition in material leads to a temperature increase. Damage to the material occurs by melting or plastic deformation. Beam-induced damage and quench limits are given for short losses by the peak energy density and for *steady-state* losses by the power deposition in the sensitive equipment. Depending on the time scale of beam losses, the protection relies on different, partly redundant, systems. The time scale of losses can be grouped in five categories as shown in Tab. 1.2. Fig. 1.4 lists loss durations and responding protection systems. Additionally, losses can be grouped by failure type and its corresponding beam loss pattern around the ring, e.g. quadrupole powering failure or spontaneous firing of an injection kicker [Alo06a, Alo06b]. Critical error scenarios for the protection system are especially *ultra-fast* losses in the injection and extraction phase.

The protection system of the LHC is composed of passive protection components, such as the collimation system (including absorbers installed in front of sensitive components), and active systems which can trigger a beam extraction. The Beam Loss Monitoring (BLM) system, the Quench Protection System, and the cryogenic system [Ver03, Fil05] can issue a request for beam extraction in order to protect machine components from damage.¹

¹There are numerous additional systems which can issue an extraction request in order to protect the LHC

1. The Large Hadron Collider and its Protection Systems

Loss type	Timescale
Ultra-fast	$< 356 \mu\text{s}$ (0 – 4 turns)
Fast	$356 \mu\text{s} - 10 \text{ ms}$
Intermediate	$10 \text{ ms} - 10 \text{ s}$
Slow	$10 - 100 \text{ s}$
Steady state	$> 100 \text{ s}$

Tab. 1.2.: Classification of loss durations.

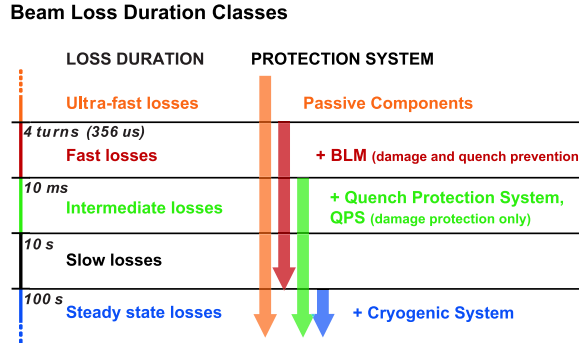


Fig. 1.4.: Classification of beam losses according to their duration and the applicable protection systems, courtesy of E.B. Holzer.

A failure of the LHC protection system resulting in damage to one of the superconducting magnets would cause a down time of up to several months.

1.2.1. Collimation System

Traditionally, the outer part of the beam, the *beam halo*, did not pose a mayor threat to the accelerator components. Yet, this changed with energy and intensities envisaged for recent high-energy accelerators. Proper and efficient removal of deviating beam particles, the collimation of the beam, has become a major design issue for building and running machines like the LHC, as it allows for higher intensities, and thus higher luminosity, without the threat of damaging and quenching the accelerator machinery and detectors. This section outlines general features of the LHC collimation system and comments on some details as they are relevant for this thesis. More literature on the LHC collimation system can be found in [LHC03, Rob06].

Collimators and their Design Specifications

Collimators are robust and movable beam-line elements used to remove halo particles before they are lost in an uncontrolled way in sensitive machine elements. They are set to be the initial material seen by deviating beam particles and are designed to withstand the energy deposition of the excess of lost beam particles and their showers. Fig. 1.5 shows pictures of the internal structure of an LHC collimator. Collimators protect the LHC against irregular fast

and its experiments that are not listed here as they are not of primary concern for this work.

1. The Large Hadron Collider and its Protection Systems

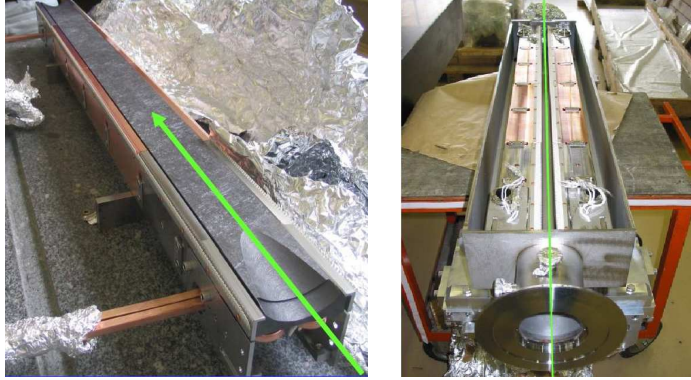


Fig. 1.5.: The photos show the inner structure of a secondary collimator (TCSG) as integrated in the LHC. The left picture shows a single graphite jaw with tapered edges. The right picture shows a top view of a collimator with both jaws integrated in the collimator box. Green lines indicate the position of the beam.

losses by absorption and dilution. They “clean” the circulating beam constantly by removing particles with a large position or momentum deviation. Unavoidable, slow losses occur due to beam-beam interaction background from the experiments, internal bunch and residual gas scattering, imperfections in the beam optics resulting in an orbit shift or emittance growth, RF noise, etc.

The jaw materials of the LHC collimators were chosen to withstand a high energy deposition while maximizing dilution and absorption. The latter mainly depends on the inelastic interaction length λ_{inel} of the material at LHC energies. Different materials and geometries were chosen depending on the location in the ring and on the required functionality. Main materials used are carbon fiber-reinforced graphite (CC), copper, and tungsten. Tab. 1.3 lists different collimators. The TCLA and the TCT collimators are mechanically identical, but they serve for different purposes in the LHC collimation. An exhaustive, list of the LHC collimators and some of their properties can be found on the web at [Col].

Collimator	Technical name	Nominal jaw opening	Jaw length	Jaw material
Primary	TCP	6σ	60 cm	CC
Secondary	TCSG	7σ (squeezed: 10.5σ)	100 cm	CC
Tertiary	TCT	8.3σ (squeezed: 13.5σ)	100 cm	W/Cu
Absorber	TCLA	10σ	100 cm	W/Cu

Tab. 1.3.: Collimator types in cleaning regions and tertiary collimators. Other collimators of similar dimensions and materials are placed along the LHC ring. Jaw openings are given for nominal 7 TeV betatron cleaning. σ is the rms beam size; at injection $\sigma_{\text{inj}} \approx 1$ mm, at top energy $\sigma_{\text{top}} \approx 0.3$ mm). The machine aperture at injection is approximately at 10σ . Jaw length refers to the effective length of the jaw material seen by the beam. When including tapering angles and the interconnection, the total length of an LHC collimator amounts to 148 cm.

The gap between the collimators can vary between 0.5 – 60 mm. The collimator jaws are positioned with stepping motors to a precision of $5 \mu\text{m}$. The control of the the beam-jaw angle is within $5 \mu\text{rad}$. Fig. 1.6 shows a sketch of the surface of a collimator jaw. The jaw surface is not a perfect plane. The deviation from a plane is measured by the parameters flatness

and roughness. The collimators used in the LHC are designed to have a surface roughness of $\leq 1.0 \mu\text{m}$ [$\leq 1.6 \mu\text{m}$] for TCP's [TCSG's]. TCP's [TCSG's, TCLA's] have an average surface flatness of $34 \mu\text{m}$ [$48 \mu\text{m}$, $36 \mu\text{m}$]. CC collimators were tested to withstand a shock beam

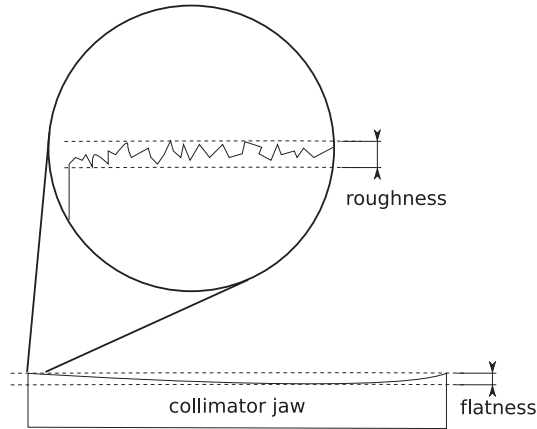


Fig. 1.6.: The surface of a collimator is not perfectly plane. It has a microscopic structure, referred to as roughness, and an overall bend, referred to as flatness.

impact of 2 MJ/mm^2 without damage (nominal injected LHC batch at 450 GeV). Absorbers, positioned in front of beam-exposed, sensitive equipment (i.e. cold and warm magnets) additionally reduce energy deposition due to halo beam particles and parts of proton-induced showers. Movable absorbers have the same mechanical design as collimators, but they are equipped with high-Z (atomic number) jaw materials and are operated with larger gaps.

Layout of the Collimation System

The collimation of the LHC is done in a phased approach adapted to the different operation stages of the LHC. References made in this work refer to the initial Phase 1. Components and layout of later phases (up to four), envisaged for higher intensities and ion collimation, are still being investigated. Phase 1 uses forty-four collimators and absorbers per LHC beam. In App. E the position of LHC collimators is shown schematically. The types of collimators and absorbers are divided into seven categories according to their position in the LHC infrastructure and their dedicated task:

Betatron and momentum cleaning (TCP, TCSG, TCLA): For the efficient capture of deviating particles, either in transversal direction – called betatron cleaning, or in momentum, collimators are positioned in specific phase-advance locations. There are two insertions dedicated to betatron and momentum cleaning, IR7 and IR3, respectively. Most collimators are located in these insertions. In order to meet a collimation inefficiency (or leakage rate), defined as

$$\eta_{\text{col}} := \frac{\text{number of escaping protons } (> 10\sigma)}{\text{number of impacting protons } (> 6\sigma)}, \quad (1.1)$$

of less than $2 \cdot 10^{-5}$, a multi-staged collimation system is of need. High energetic particles interacting with a collimator result in a particle halo which is then intercepted and attenuated by higher order collimators. Fig. 1.7 shows a schematic of the three-stage approach adapted for the LHC.

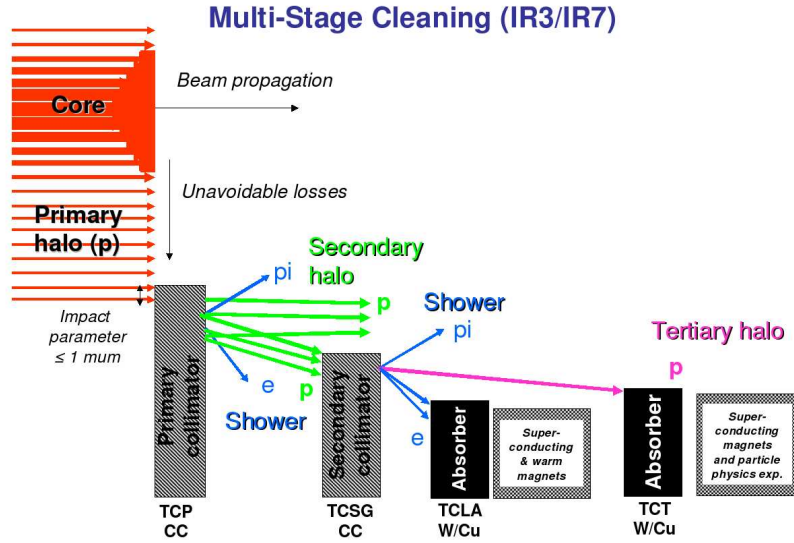


Fig. 1.7.: Schematic of the multi-stage cleaning as performed in the LHC, adapted from R. Assmann. The beam halo is diluted by the TCP's. The secondary shower leaving the TCP's is then attenuated by TCSG's and higher-order high-Z collimators.

The impact parameter b of beam-halo protons on the collimator jaw is defined as the impact depth measured from the edge of the collimator jaw, see Fig. 1.8. Initial mean impact

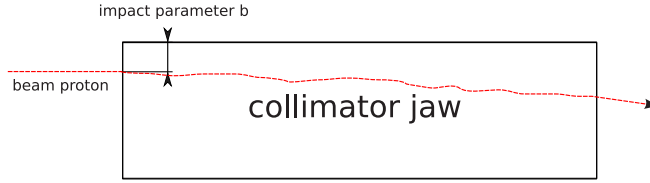


Fig. 1.8.: Definition of the impact parameter as distance from the collimator surface.

parameters on TCP collimators for nominal operation are estimated to be between

- ★ $1.16 - 5.07 \mu\text{m}$ for injection,
- ★ and $0.3 - 1.28 \mu\text{m}$ for collision optics

independent of the transversal plane [Rob06]. This changes in case of magnet failures, where average impact parameters can reach up to about $800 \mu\text{m}$ for injection, and up to $70 \mu\text{m}$ for collision optics [Alo06b]. Due to the low-Z material which is used for the TCP's, the beam protons have a high probability to be scattered out of the jaw. About 95% of the energy entering a TCP jaw leaves it again. Particles impacting close to the jaw surface can be scattered out of the jaw before passing through all the length of the material, this is referred to as *edge escape*. Longer secondary collimators (TCSG's), which are further withdrawn from the beam, are employed to intercept the bulk of particles leaving the primary. Protons incident with impact parameters of $b \sim 200 \mu\text{m}$. The tertiary halo then impacts on absorbers, the machine equipment and on the tertiary collimators.

Triplet protection (TCT): These collimators protect the exposed triplet magnets in front of the experiments.

Transfer line collimators (TCDI): A set of six collimators per transfer line from SPS to LHC (about 2.4 km long) are used to limit excursions of mis-steered particles. A seventh collimator is used to intercept particles with large momentum offset.

Injection protection absorbers (TCLI,TDI): These absorbers are set up to protect the LHC elements after the injection kickers against damage due to kicker failure resulting in a wrong injection angle.

Beam dump protection absorbers (TCDS,TCDQ,TCSG): The dump extraction kickers have to be synchronized with the particle-free *beam abort gap*². To protect against beam losses due to an abort timing mismatch or spontaneous firing of the kicker magnets, two several meter long absorbers are installed after the kickers in front of the *septum magnets*³ and further downstream of the kickers. Additionally, a two-sided CC collimator constrains the beam. The TCDS is not movable.

Collision debris collimators (TCLP): These collimators are installed in IR1 and IR5 to capture part of the debris from the pp interaction in the experiments.

Focus of this Work

Studies in the scope of this thesis focus on the collimator types used in the cleaning insertions (TCP, TCSG, TCLA). They constitute more than 80% of the installed collimators and are of prior interest for monitoring by the BLM system as they see abundant losses. At the collimators, the surveillance for abnormally increased loss rates is achieved by

- ★ BLM detectors measuring beam loss rates close to the collimators,
- ★ and temperature sensors measuring heat load on the collimators⁴.

1.2.2. Beam Loss Monitoring System

The Beam Loss Monitoring (BLM) system is the main active system to prevent damage to magnets and collimators from all possible multi-turn losses. It is the most important active and therefore critical system for *fast* and intense beam particle losses. Further, it is the only system preventing the quenching of superconducting magnets by initiating a beam abort. For medium and longer loss durations the BLM system is assisted by the Quench Protection System and the cryogenic system.

²Gap in the bunch train of the LHC which is sufficiently long to allow the rise of the magnetic field of the extraction kickers.

³Bending magnets right after the start of the extraction line. They are used to bend the extracted beam away from the LHC beam pipe at a larger angle.

⁴Temperature interlock at 40° to 50° C.

Design Specifications of the BLM System

A high dynamic range for the detection of particle fluxes is required to cover all relevant regimes. This is achieved by installing two different types of detectors at critical locations. The monitoring system which is set up around the ring consists of about 3700 ionization chambers (IC's) and 280 secondary emission monitors (SEM's), installed at radiation-exposed positions in vicinity of sensitive equipment. At critical radiation levels, these detectors trigger within one turn ($88.92 \mu\text{s}$) a beam extraction in order to prevent a quenching of superconducting magnets or damage to components [Hol05]. The maximum total time needed from the occurrence of the error until the beam is safely extracted amounts to 3-4 turns, ca. $350 \mu\text{s}$. IC's serve as primary detectors. In high-loss regions, e.g. at a collimator, supplementary SEM's are installed yielding an increase of the detection range from 10^8 to 10^{13} . The detectors probe the transverse tails of hadronic showers through the cryostats and in the collimation insertions.

The BLM protection system requires an extremely high reliability (tolerable failure rate of 10^{-7} per hour per channel) coupled with a low rate of false dumps [Fil05]. A false dump is a beam extraction triggered by a protection system which is not necessary to prevent damage or quenching of LHC equipment and leads to unwanted down time. This is achieved by choosing reliable components, by redundancy combined with voting (in case of not sufficiently reliable components), and by a continuous surveillance of the availability of the readout channels. There must be less than two false dumps per month in order to guaranty the operational efficiency of the LHC.

In addition to its protective features, the BLM system allows at local aperture restrictions for adjustment of the position of the collimation devices, as well as for the observation of orbit distortions, beam oscillations, and particle diffusion.

BLM Thresholds

The BLM thresholds settings of the detectors depend on

- ★ the BLM detector type, i.e. IC or SEM,
- ★ the type of sensitive equipment,
- ★ the location of the detector with respect to the loss location and the sensitive equipment,
- ★ the loss duration,
- ★ and beam energy.

A relation between (pre-)critical radiation levels in vulnerable equipment and a signal seen by the BLM detectors has to be established. The start-up calibration of the detection system is aimed to be within a factor of five in accuracy. For the final calibration a factor within two is foreseen.

A series of studies is devoted to the proper calibration of the final thresholds. Upper safe operation values of sensitive, radiation-exposed equipment were determined, i.e. for collimators, and magnets. Additionally, the quenching levels of superconducting magnets are investigated [Boc08]. IC's and SEM's were calibrated and their response functions were determined [Sto07, Kra08]. Particles have been tracked for LHC optics to find the most probable loss locations. The transversal shower distributions at the BLM positions have been calculated [Hol05].

2. Particle–Matter Interaction

When beam protons are lost in aperture limitations of the beam pipe they interact through various channels, triggering cascades of newly produced particles, so-called *secondaries*, which in turn interact themselves. These interactions result in a heat load deposited in the irradiated matter, which can melt the material, cause mechanical damage, and aging – or also a quench in case of superconducting material.

To adequately estimate particle fluxes due to high-energetic reactions as they take place in present-day colliders, one needs to describe the whole hadronic cascade from several TeV down to thermal energies. Most particle production takes place at energies below 1 GeV. Particle showers are categorized into two types, electromagnetic (EM) and hadronic showers, according to the main interaction channel of the primary particles, being the EM or the strong force, respectively. Some considerations on general features of high-energetic showers and consequences for their description can be summarized as follows [Fer96b]:

- ★ The development of hadron-initiated showers is ruled by both frequent atomic processes (stopping power dE/dx , Multiple Coulomb Scattering (MCS), etc.) and relatively scarce elastic and inelastic nuclear interactions. EM showers are determined by the same atomic processes, plus additional atomic processes such as Bremsstrahlung, pair production, Compton scattering, etc., which are specific for γ 's and e^\pm 's. Nuclear interactions in EM showers play a minor role and are irrelevant whenever the focus is not on the hadrons produced by EM particles.
- ★ The most energetic particles (*shower particles*) are located mainly around the beam axis of primary particles, regardless of their identity. The energy deposition profile in this area is mainly characterized by the stopping power dE/dx and the profile of superimposed EM cascades associated with π^0 's.
- ★ Neutral hadronic particles, that is in practice neutrons – as they are the only ones which are sufficiently stable, are dominant at energies where the range of charged particles becomes shorter than the interaction length. Energy deposition profiles are characterized in their tails by the interactions of low energy neutrons, i.e. recoils and γ -production.
- ★ Most interactions involve particles of intermediate to lower energies (mainly neutrons). This means that a precise quantitative treatment for the bulk of low energy particles is needed.
- ★ On the other hand, shower evolution is determined in the first place by high-energetic particles which initiate the showers. They carry the main fraction of the total energy and have a longer interaction length. An inappropriate treatment and approximations made in the simulation of their interaction can never be recovered in following steps.

This chapter summarizes some of the principal interaction mechanisms of particles traversing matter and provides, along the way, some examples for a quantitative treatment of such

2. Particle–Matter Interaction

processes. A more elaborate description can be found in literature such as [PDG06, Bur95, Fer96b, Fer97].

2.1. Probability of Interaction

The probability of the occurrence of a certain interaction process j between two corpuscles x, y is measured by its cross-section σ_{xy}^j , also called partial cross-section. The cross-section σ_{xy}^j of a process is defined for a very small attenuation of N_x incident particles x on a thin target of thickness Δs consisting of particles of type y , by the equation [Bur95]

$$N_j = N_x \cdot \rho_y \cdot \Delta s \cdot \sigma_{xy}^j, \quad (2.1)$$

where N_j is the number of times the process j takes place, and ρ_y is the number density of y in the target. Values of nuclear cross-sections range from about 0.1 barn, for a small nucleus, to about 10^7 barn, for slow neutrons¹ [Bur95]. The sum of all partial cross-sections for a given projectile-target combination is called total cross-section [Boc98]

$$\sigma^{\text{tot}} \equiv \sigma_{xy}^{\text{tot}} = \sum_j \sigma_{xy}^j. \quad (2.2)$$

In the following the total nuclear cross-section will be associated with this symbol. The sum of all nuclear cross-sections σ^{tot} is often decomposed into

$$\sigma^{\text{tot}} = \sigma^{\text{el}} + \sigma^{\text{inel}} + \sigma^{\text{dif}}, \quad (2.3)$$

its elastic, inelastic, and quasi-elastic (diffractive) part.

In case of non-destructive scattering of the incoming particle, that is elastic or quasi-elastic scattering, the differential cross-section $d^2\sigma/d\Omega dp$ denotes the probability of scattering the incident particle in the solid angle $d\Omega$ with a momentum offset dp . Some processes, like Coulomb scattering in matter, have an infinite cross-section – incident particles are constantly subject to overlapping electric fields.

The mean free path λ_{tot} of a particle in a medium with density ρ is given by

$$\lambda_{\text{tot}} = \frac{A}{\sigma^{\text{tot}} \cdot N_A \cdot \rho}, \quad (2.4)$$

where A is the atomic weight, and $N_A = 6.022 \cdot 10^{23} \text{ mol}^{-1}$ is Avogadro's number. The mean free path for other partial cross-sections is defined analogously. It follows that the probability density function (PDF) for distances between two successive collisions is then given by

$$P(s) ds = \frac{1}{\lambda_{\text{tot}}} e^{-s/\lambda_{\text{tot}}} ds. \quad (2.5)$$

The nuclear elastic and inelastic interaction length λ_{el} and λ_{inel} , respectively, scale analogously to Eq. 2.5 the length traveled by a particle before undergoing an elastic or inelastic nuclear reaction. λ_{inel} is essentially energy independent over wide ranges of energies. Tab. 2.1 displays λ_{el} , and λ_{inel} for protons in different materials at LHC energies.

For a quantitative description of interaction processes it is convenient to model some interactions which occur with a high frequency as *continuous processes*, whereas less probable

¹1 barn $\equiv 10^{28} \text{ m}^2$

2. Particle–Matter Interaction

Material	ρ [g/cm ³]	λ_{el} [cm]	λ_{inel} [cm]	X_0 [cm]	dE/dx [GeV/m]	$\theta_{\text{MCS}}^{\text{rms}}$ [μrad]
at energy [GeV]		450/7000	450/7000	450-7000	450	450/7000
Be	1.85	120/98.7	40.6/37.1	35.28	0.55	53/3.4
C	1.77	118/99.0	46.1/42.1	24.12	0.68	72/4.6
Cu	8.96	23.9/21.6	14.6/13.9	1.44	2.69	292/19
W	19.3	12.7/12.0	9.18/8.93	0.351	5.79	618/40
Pb	11.4	21.8/20.8	16.1/15.7	0.561	3.40	481/31

Tab. 2.1.: Nuclear elastic interaction length λ_{el} , nuclear inelastic interaction length λ_{inel} , and radiation length X_0 for protons. Values are from FLUKA tabulations. The last two rows list stopping power dE/dx for 450 GeV protons, taken from [Rob06], and the rms MCS scattering angle after a material length of 100 cm.

processes, such as hadronic interactions, are usually treated as *point-like*. Due to the large range of the EM force, interaction processes between charged particles, such as small-angle coulomb scattering, ionization, and atomic excitation, occur frequently and are efficiently described by Multiple Coulomb Scattering (MCS) formalism and the Bethe-Bloch formula.

2.2. Energy Loss due to Electromagnetic Processes

Ionization and Atomic Excitation

Moderately relativistic charged particles other than electrons lose energy primarily by EM interaction between the incoming particle and the electron cloud of the atom. This can lead to ionization, when liberating a single electron, or at low energy transfer to atomic excitation. A quantitative description of the mean rate of energy loss of charged particles in matter² or the so-called *stopping power*, is given by the Bethe-Bloch equation [PDG06]

$$S := -\frac{dE}{dx} = K \cdot N_c^2 \frac{Z}{A} \frac{1}{\beta_L^2} \cdot \left(\frac{1}{2} \ln \frac{2 \cdot m_e c^2 \cdot (\beta_L \gamma_L)^2 \cdot T_{\text{max}}}{I^2} - \beta_L^2 - \frac{\delta(\beta_L \gamma_L)}{2} \right). \quad (2.6)$$

Here Z and A are the atomic number and the atomic weight of the absorber, respectively. N_c is the number of elementary charges e_0 of the incident particle. $K = 4\pi N_A r_e^2 m_e c^2$ is a constant³. β_L is the velocity of the particle expressed as a fraction of the velocity of light c , and $\gamma_L = (1 - \beta_L^2)^{-1/2}$. $m_e c^2$ is the rest energy of an electron. I is known as the *mean excitation energy* of the absorber, and can be roughly approximated for elements heavier than Oxygen with

$$I \approx 10 \text{ eV} \cdot Z. \quad (2.7)$$

More exact values can be found in [PDG06]. T_{max} is the maximum kinetic energy that can be transferred by the charged particle to a free electron in a collision. Thus, its value depends on the mass of the impacting particle M . T_{max} is given by

$$T_{\text{max}} = \frac{2 \cdot m_e c^2 \cdot (\beta_L \gamma_L)^2}{1 + 2\gamma_L \cdot m_e/M + (m_e/M)^2}. \quad (2.8)$$

²Neglecting radiative effects and *point-like* interactions.

³ $N_A = 6.022 \cdot 10^{23} \text{ mol}^{-1}$ is Avogadro's number. $r_e = 2.82 \text{ fm}$ is the classical electron radius.

2. Particle–Matter Interaction

$\delta(\beta_L \gamma_L)$ is a density effect correction to ionization energy loss correcting for the flattening of the electric field of a relativistic incident particle. It is usually approximated by Sternheimer’s parameterization [PDG06].

At higher energies corrections for radiative effects become important. The critical energy E_{crit} of a specific material marks the point where the energy loss by radiation is equal to the energy loss by collision and ionization. For lower energies there are various relevant corrections.

Fig. 2.1 shows energy-loss rates for different materials without correcting radiative effects⁴. Apart from a slight dependence on the mass of the incident particle (introduced through T_{max}) at high energies, S for a given particle and material type depends only on β_L . Except in hydrogen, particles of the same velocity have similar loss rates in different materials. For relativistic energies S rises logarithmically.

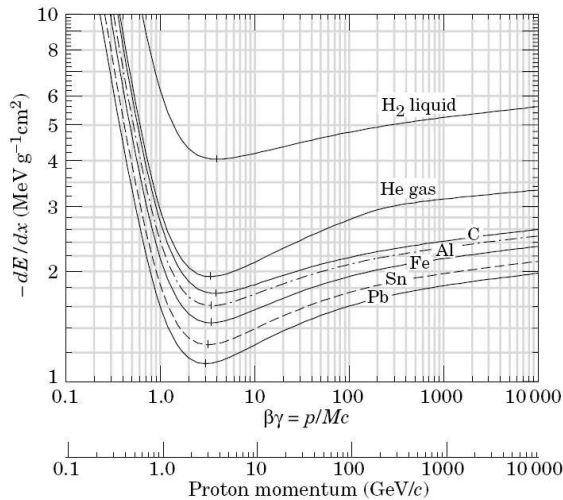


Fig. 2.1.: Mean energy-loss rate in liquid (bubble chamber) hydrogen, gaseous helium, carbon, aluminum, iron, tin, and lead, taken from [PDG06].

The limits of the validity of the Bethe-Bloch formula depend on both the effective atomic number and the mass of the impinging particle. For instance, for pions traveling in copper, the Bethe-Bloch formula describes the energy loss for energies between 6 MeV and 6 GeV to an accuracy of about 1%.

Electromagnetic Particles

Fig. 2.2 shows fractional energy loss of e^\pm 's as a function of energy. For low energies, e^\pm 's lose energy mainly through ionization while processes such as Møller and Bhabha scattering, and e^+ -annihilation contribute. At energies over a few tens of MeV (see Fig. 2.2, at about 10 MeV for lead), energy loss due to Bremsstrahlung ($e^\pm \rightarrow e^\pm + \gamma$), increasing nearly linear with energy, dominates in most materials. For μ^\pm this critical energy is at several hundred GeV. Photons lose also energy by ionization and atomic excitation. For energies higher than about 100 MeV pair production ($\gamma \rightarrow e^+ + e^-$) is dominating.

For EM interactions the radiation length X_0 is the crucial scaling length (as used for the normalization in Fig. 2.2). It is the distance at which a high-energy electron loses all but $1/e$

⁴Relevant for pions and muons.

2. Particle–Matter Interaction

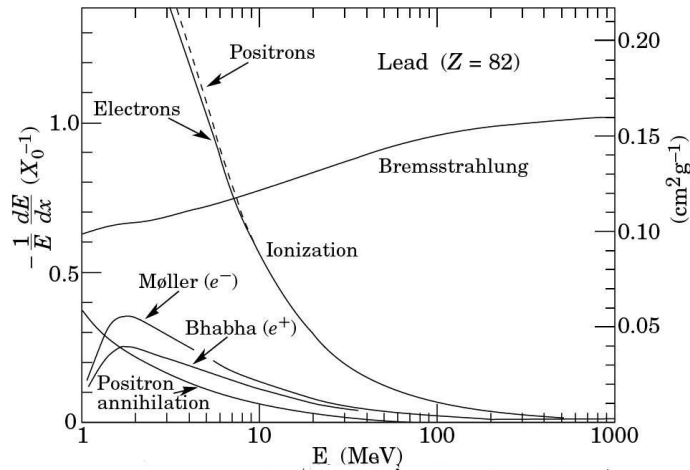


Fig. 2.2.: Fractional energy loss per radiation length in lead as a function of electron or positron energy, taken from [PDG06].

of its energy due to Bremsstrahlung. X_0 is also 7/9 of the average distance for pair production by a high-energetic photon. A compact fit to experimental data is given by [PDG06]

$$X_0 = \frac{716.4 \text{ g cm}^{-2} \cdot A}{Z(Z+1) \ln(287/\sqrt{Z})}. \quad (2.9)$$

Tab. 2.1 displays X_0 for protons in different materials.

2.3. Multiple Coulomb Scattering

Charged particles traversing matter face numerous small angle deflections due to Coulomb scattering by electrons and nuclei. After traveling through a length of material s a charged particle's path deviates by a transverse offset x and an angular deflection θ from its initial one, due to Coulomb scattering processes, as sketched in Fig. 2.3. A cumulative, stochastic treatment of these microscopic scattering events is referred to as Multiple Coulomb Scattering (MCS). Here some results of Moliere's theory of multiple small-angle scattering are summarized [PDG06, Rob06].

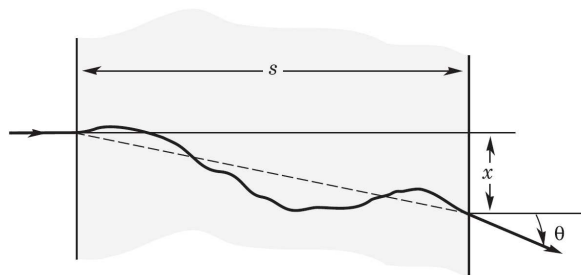


Fig. 2.3.: Schematic view of Multiple Coulomb Scattering (MCS) in one plane, adapted from [PDG06].

The angular distribution obtained by Moliere's MCS theory is roughly Gaussian for small deflection angles, but with larger tails. By fitting the angular distribution one can obtain the

2. Particle–Matter Interaction

following rms scattering angle for a transversal plane as a function of the traversed length s [PDG06]:

$$\theta_{\text{rms}}(s) = \frac{13.6 \text{ MeV}}{\beta_L \cdot pc} \sqrt{\frac{s}{X_0}} \left(1 + 0.038 \cdot \ln \left(\frac{s}{X_0} \right) \right). \quad (2.10)$$

The rms traverse offset is then given by

$$x_{\text{rms}}(s) = \frac{1}{\sqrt{3}} \cdot s \cdot \theta_{\text{rms}}(s). \quad (2.11)$$

Angular deviation of particles due to Coulomb scattering scales for high energies ($\beta_L \approx 1$) with the inverse of the momentum. Some rms scattering angles θ_{rms} of protons at LHC energies after traversing 100 cm of matter are listed in Tab. 2.1. Charged particles which actually get in close vicinity of ions are deflected by a substantial angle. This process is not well reproduced by Moliere’s MCS, but can be described by Rutherford scattering. A convenient approximation is often to split the Coulomb scattering cross-section into two parts, and treat small angle scattering by Moliere’s MCS and the scarce large angle scattering by Rutherford scattering. A coherent way of dealing with MCS is to employ the more complex MCS formalism from Goudsmit-Saunderson [Fer96a].

2.4. Nucleon-Nucleon Interactions

This paragraph presents cross-sections for nucleons in matter and gives a formula to estimate their scattering amplitudes for high energies. There is a manifold of different nuclear reaction types and regimes. App. B introduces basic concepts for describing nuclear interactions systematically.

In Section 2.1 is discussed that the probability for the occurrence of an interaction process between two particles is described by its cross-section σ . Elastic nucleon-nucleon (NN) scattering is the only possible way of interaction for nucleons below the π -production threshold. Cross-sections for pp (or nn), and pn total and elastic cross-sections are shown in Fig. 2.4. The total cross-sections both increase rapidly for small energies, as seen in the left side of the graph. Their difference for energies smaller than ≈ 300 MeV is explained by symmetry and isospin considerations. For higher energies pp and pn cross-sections are equal and rise nearly linearly in double logarithmic scale. For energies up to about 300 MeV the pp angular distribution is fairly isotropic. In contrast, the pn angular distribution is getting more anisotropic for smaller energies. Starting with a few hundred MeV both angular scattering distributions develop a strong forward peak. From energies above 1 GeV the bulk of the angular scattering distribution can be described by an optical diffraction model. The rms scattering angle in a plane is given for these energies by the following formula:

$$\theta_{\text{el}}^{\text{rms}} = \sqrt{3 \cdot A^{3/2} \cdot \frac{0.135 \text{ GeV}}{pc}}, \quad (2.12)$$

where p is the momentum of the scattered particle [RPP92]. After N_{el} scattering events with the angle $\theta_{\text{el}}^{\text{rms}}$, the total angle is $\sqrt{N_{\text{el}}} \cdot \theta_{\text{el}}^{\text{rms}}$.

2.5. Electromagnetic Showers

High-energetic photons, electrons, and positrons interact primarily through processes, such as Bremsstrahlung and pair production. The products of these interactions are, again, γ ’s

2. Particle–Matter Interaction

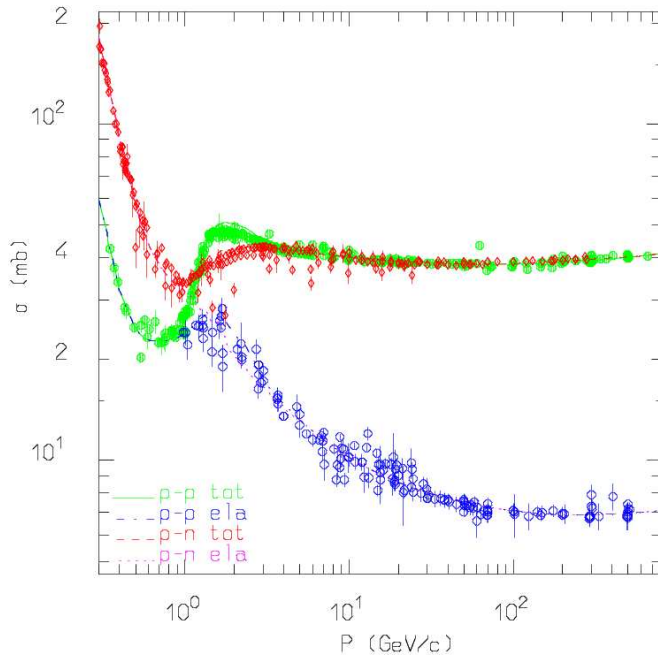


Fig. 2.4.: Total and elastic cross-section for proton-proton (pp) and proton-neutron (pn) scattering, taken from [Fer96b]. Lines are calculated with FLUKA, points are experimental data.

and e^\pm 's, which then react in a similar way. Fig. 2.5 depicts a schematic drawing of such a multiplication. Cross-sections for these particles are nearly energy-independent above 1 GeV. The scaling length for EM showers is the radiation length X_0 . The maximum of the cascade is reached when the average energy of the components is too low to permit further multiplication. The shower then decays slowly through ionization losses and Compton scattering. This regime transition is characterized by the critical energy E_{crit} (for definition see Section 2.2) of the absorber material. It can be roughly approximated by

$$E_{\text{crit}} \approx 800 \text{ MeV} / (Z + 1.2) , \quad (2.13)$$

where Z is the number of protons in the nucleus [PDG06]. The shower maximum can be approximated by the parameterization

$$l_{\text{EM}}^{\text{max}} = \left(\ln \left(\frac{E}{E_{\text{crit}}} \right) - a \right) \cdot X_0 , \quad (2.14)$$

where $a = 0.5$ for γ -induced cascades, and $a = 1.0$ for e^\pm -induced cascades [PDG06].

2.6. Hadronic Showers

As soon as the energy of an initial hadron exceeds several 10 MeV, inelastic interactions start contributing significantly in the development of its shower. A hadronic shower is characterized by multiple particle production due to high-energetic hadrons which interact in nuclei, so-called intra nuclear cascades. Remaining nuclei are often left in an excited state, and decay

2. Particle–Matter Interaction

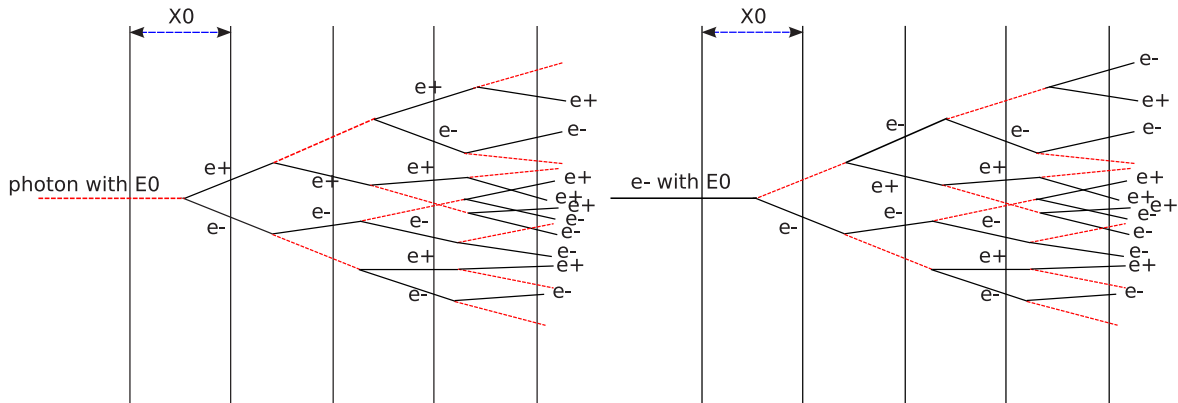


Fig. 2.5.: Schematic drawing of an electromagnetic (EM) cascade. Left [right] for an electromagnetic (EM) shower initiated by a photon [electron]. X_0 is the radiation length.

under the emission of further particles⁵. Secondaries created in the cascades, among them mostly pions and nucleons, have sufficient energy to trigger further interactions. Dependent on the energy of the primary hadrons⁶, mesons (mainly π^0 's and η 's) decaying electromagnetically into γ 's and e^\pm 's (e.g.: $\pi^0 \rightarrow \gamma\gamma$), give rise to an electromagnetic component in the shower. A simple relation estimating the fraction of hadronic and EM shower component is given by

$$\frac{(\text{No. of } \pi^0)}{(\text{No. of all part.})} \approx 0.10 \cdot \ln \left(\frac{E}{1 \text{ GeV}} \right), \quad (2.15)$$

with E the energy of the primary hadron [Boc98]. For a 7 TeV-beam hitting a fixed target this fraction evaluates to about 90%.

The development of hadronic multiplication is scaled by the nuclear interaction length λ_{inel} . Consequently, the shower maximum of a high-energetic hadronic shower is determined by the energy E of the primaries and λ_{inel} . It is approximately given by the parameterization [Boc98]

$$l_{\text{HAD}}^{\text{max}} = \left(0.6 \cdot \ln \left(\frac{E}{1 \text{ GeV}} \right) - 0.2 \right) \cdot \lambda_{\text{inel}}. \quad (2.16)$$

For instance, for a 7 TeV-beam hitting a carbon [copper] collimator with a density of 1.77 g/cm³ [8.96 g/cm³] the shower maximum is expected at 215 cm [71 cm].

⁵Opposed to EM showers, which develop in sub-nanosecond time, hadronic showers have a much larger time scale reaching up to microseconds for the de-excitation of heavy nuclei.

⁶The pion production threshold for nucleons interacting with stationary nucleons is about 290 MeV.

3. Simulation Techniques for Particle-Matter Interaction

The Monte Carlo method refers to a numeric integration based on random numbers. A typically highly multi-dimensional phase space is modeled mathematically by functions depending on random variables. By sampling randomly chosen representative subsets of all possible states of this phase space one obtains information about statistic quantities, i.e. mean values, momenta of second and higher orders, of desired quantities of such a system. For a sufficiently large number of samples N these quantities converge toward the true solution of the problem scaling with $1/\sqrt{N}$. Briefly speaking, one dramatically reduces the computational expense of a problem by restricting the significant outcome on average quantities and abandoning the (often impossible) alternative of a classical numeric or even analytic approach. The generality of this mathematic method makes it a feasible tool for a vast variety of applications involving complex and multi-dimensional model spaces. These applications range from pure mathematical and physical problems, such as high-dimensional integration, far into the fields of economics, biology, and other sciences. Quantum mechanical based formalisms are generally well suited for Monte Carlo methods since they can reflect the nature-based randomness involved in such problems – a quantum mechanical measurement is not a deterministic process. The outcome of a measurement is determined by a underlying probability distribution. This inherent randomness gives a natural connection to Monte Carlo simulations.

3.1. Structure of a Particle Transport Code

In the problem treated in this thesis a high-energetic beam impacts initially on the surface of a collimator jaw creating hadronic and electromagnetic showers which start to evolve in the jaw material and later on in the adjacent machine components. Shower tails are detected by monitors placed close to the beam pipe behind the collimator. General aspects of particle-matter interactions were described in Chapter 2. A Monte Carlo tool simulating such interactions can be schematically structured in the following way:

1. A primary particle is given with an initial momentum and an initial position in a modeled geometry.
2. This particle, and all the others subsequently produced due to this primary (in the following referred to as *secondaries*) are transported, i.e. its coordinates are changed, through the given geometry until an interaction event occurs.
3. The transport distance is determined by the probability of interaction for the given particle type and its energy in the current medium. A random number generator is employed to calculate such a distance by sampling the corresponding PDF as described in App. C.

3. Simulation Techniques for Particle-Matter Interaction

4. At the point of an interaction all the possible interaction channels for the particle with given energy in the given medium are taken into account, being N the number of possible interactions. By a program-internal algorithm (see later) the probability of occurrence P_i of the i^{th} interaction is assigned to each of the N possible interactions. Evidently, $\sum_{i=0}^N P_i$ must be 1. An uniformly distributed random number (see App. C) then decides on the type of interaction occurring.
5. Given that a certain reaction occurs, all particles leaving the reaction point are assigned a momentum and a scattering angle, given by a quantitative model of the interaction process. This requires further sampling of correlated PDF's of angular distribution and momentum for all leaving particles. Newly created particles are placed in the computer stack together with their properties, e.g. position, momentum, type, age, etc.
6. Particles are tracked subsequently until they undergo an inelastic interaction – being transformed, absorbed, or annihilated –, or until they leave the geometry.
7. Frequently occurring interactions, such as Coulomb scattering and energy losses due to ionization, are treated cumulatively, e.g. for Coulomb scattering by the MCS formalism, in order to improve computing efficiency.
8. A program-internal *step size* determines the space interval in which continuous effects on a traveling particle are taken into account. This parameter is often variable, depending on the particle type, its energy, and current position. Robust algorithms for the cumulative treatment of interactions should show a *step size*-independence over the crucial range of this variable. The *step size* should be smaller than the smallest dimension of the adjacent regions.
9. Steps discussed above are repeated for all given primaries. Quantities of interest, such as particle fluencies and energy deposition, are scored in regions of interest. The results converge with increasing statistics, i.e. increasing numbers of primaries.

3.2. Modeling of Particle Interactions

For the quantitative implementation of physical interactions, there are several arguments which have to be considered. Their range is widely spread over topics such as availability of suitable models of interactions at different energy ranges, their reliability, availability of experimental data, possible approximations and simplifications – often depending on the quantities of interest one actually wants to observe, and computative efficiency. Literature covering this subject in more detail can be found in [Fer96a, Fer96b, Fer97, Fer02]. App. B introduces models used for systematic treatment of nuclear interactions.

A basic ingredient list of information required to describe particle interaction (not necessarily complete) is shown below:

- ★ elastic and nonelastic cross-sections as a function of projectile, target, and energy,
- ★ angular distribution for elastic scattering,
- ★ for nonelastic processes, secondary particle yields as a function of energy and angle,
- ★ residual nuclei produced by nonelastic interactions,

3. Simulation Techniques for Particle-Matter Interaction

- ★ and internal correlations between particles produced in the same event.

Ideally, the Monte Carlo tool should provide accurate predictions of the listed items for any desired spatial mesh. The degree of accuracy needed depends on the task and type of information. For example, neutron fluencies, crucial for energy deposition at lower energies, can be required to be known up to a factor of about 10% or even less, whereas residual nuclei produced locally, only rarely require an accuracy smaller than within a factor of two.

As already remarked above, certain very frequent¹ processes undergone by charged particles are conveniently treated as continuous below a suitable energy cut-off by respective formalisms, e.g. MCS, Bethe-Bloch, Bremsstrahlung. This approach is often referred to as *condensed history* Monte Carlo simulations. Possibly explicitly treated interactions are for hadrons:

- ★ δ -ray production (recoil particle that causes secondary ionization),
- ★ elastic nuclear interaction,
- ★ nonelastic nuclear interaction,
- ★ particle decay,

and for EM particles:

- ★ δ -ray production (Møller for e^- and Bhabha scattering for e^+),
- ★ annihilation (for e^+),
- ★ photoelectric effect, pair production, coherent and incoherent (Rayleigh and Compton) scattering (for γ),
- ★ optional Bremsstrahlung (for e^\pm).

These lists are indicative and not complete. Nuclear interactions can also occur with a much lower probability also for photons and even for e^\pm 's and μ 's. Bremsstrahlung is also produced by heavier particles but to a smaller extent². All charged particles can produce e^\pm -pairs. Phenomena such as Čerenkov and transmission radiation are not included. However, these processes can be safely neglected for most practical cases, whenever there is not a special focus on certain interaction products (e.g. simulation for Čerenkov detectors).

3.3. Introduction to FLUKA – a Multi-Purpose Monte Carlo Particle Code

While the former section was dedicated to the general internal structure of Monte Carlo particle codes, this paragraph presents the FLUKA code, its history and physics. There are additional remarks about topics such as biasing, and experimental verification of FLUKA physics.

FLUKA is a Monte Carlo code for particle transport and interaction. First versions of codes giving rise to the FLUKA project came about at CERN in 1962. The name itself stems from

¹The general criteria is that the mean free path is much shorter than the particle's range.

²Suppression factor is roughly $(m_e/M)^2$ for a charged particle with mass M .

3. Simulation Techniques for Particle-Matter Interaction

the German word “Fluktuierende Kaskade” and was given to the project in the 70ties. Back then, it was intended to study fluctuations in calorimeters. Since this period, the code has come a long way. It has been continuously modified to handle new particles, interactions, and energy ranges. Nowadays, there are hardly any links between the initial versions and the completely restructured FORTRAN code of the latest distributions. It is maintained and distributed by a collaboration between CERN and INFN³ Milan, but there are contributions also from other universities and institutes, such as NASA⁴ and SLAC⁵. Its fields of application cover aircraft and spacecraft radiation protection, activation studies for reactors, radiation cancer therapy, particle detectors, and beam-machine interaction studies in accelerators at SLAC and CERN. Further details about the history of FLUKA as well as program specific information can be found in the online manual, available at [Flu]. Simulations done for this thesis use the FLUKA version 2006.3b.

3.3.1. Physics of FLUKA

FLUKA is a multi-purpose transport code able to treat hadron-hadron, hadron-nucleus, neutrino, EM, and μ interaction processes from low energies up until 10 PeV. Also nucleus-nucleus collisions are handled with special ion interaction codes. Charged particles are transported including all relevant processes, as well as within magnetic fields. Whenever possible FLUKA incorporates original well-tested *microscopic* approaches of hadronic interactions. Each step is self-consistent with strong physical basis [Fas03]. This excludes the low energy transport of neutrons (up until 19.6 GeV), where commonly fits to detailed experimental data are employed to yield good results. The performance of the code is counter-checked and optimized comparing with particle production data at the single interaction level – there is no tuning performed with “integral” data. Thus, final predictions are obtained with a minimal set of free parameters, fixed for all energies and projectile-target combinations. EM interactions include: photoelectric and photonuclear interactions, pair production, Bremsstrahlung (all also for μ 's), Compton and Rayleigh scattering, Bhabha and Møller scattering, e^+ -annihilation, μ^- -capture, optic photon (Čerenkov) production and transport.

Phase-shift analysis and/or fits to differential experimental data provide the basis for nuclear elastic, charge exchange, and strangeness exchange reactions, if possible. As described in App. B two types of models are employed for hadronic interactions depending on the projectile energy: the ones based on individual resonance production and the ones based on quark/parton string models for higher energies.

FLUKA interaction models have been compared to experimental data from high-energy colliders, such as the SPS which had cms energies ranging up to about 1 TeV. For comparison, a 7 TeV proton beam interacting with fixed targets, such as collimators, has cms energies of about 188 GeV.

3.3.2. Biasing Techniques and Particle Thresholds

Maintaining correlations in the course of particle interactions means faithfully reproducing physical processes. This is referred to as *analog* simulations. Recorded quantities and their variances and higher moments will converge toward their true average value. However, convergence might be slow. For instance, if one wants to observe some rare physical processes,

³Instituto Nazionale di Fisica Nucleare

⁴National Aeronautics and Space Administration

⁵Stanford Linear Accelerator Center

3. Simulation Techniques for Particle-Matter Interaction

one would have to sample a huge amount of primaries in order to gain a sufficient amount of statistics about these processes. A second illustration: when producing particle showers by a high energetic beam, many secondaries with very similar properties are created (EM particles). To track all of these particles requires quite some time. Yet for certain quantities of interest, particles which are less frequently produced contribute considerably. To reduce computational costs, a powerful feature of the FLUKA toolbox is a variety of *biasing* techniques. They change some properties of the problem in an often unphysical way on the individual interaction basis to promote convergence of desired quantities.

Biasing does not influence the physics results of a problem. It is merely a mathematical method to promote the convergence of desired statistics to the disfavor of others. It predicts the average quantities correctly but it does not conserve higher moments. On the contrary, it aims at minimizing the second moment. *Biasing* does not reproduce correctly correlations and fluctuations. Furthermore, one has to be very careful when applying these techniques as, falsely applied, they can lead to misleading statistics and wrong conclusions.

Simulated particles are prescribed a new property *weight*. Initially, it is generally equal 1. It determines a particle's contribution to recorded quantities. There is a large variety of *biasing* techniques provided by FLUKA and it is up to the user to choose the suitable ones. In this place, only the relevant ones will be discussed.

Surface Splitting/Russian Roulette: Particles which cross defined surfaces are reduced or multiplied on average with certain probabilities, adjusting at the same time the particle's *weight* accordingly to compensate for the bias, i.e. $\text{probability} \times \text{weight}$ is constant. This technique can be used to obtain constant particle fluencies in different regions of the geometry, e.g. compensating for attenuation by absorption. It is adjustable by particle type.

Leading Particle Biasing: This method is applied to γ 's and e^\pm in order to compensate the geometric increase of these particles in high-energetic EM showers. Instead of tracking two particles which are characteristically produced in EM processes only one is kept with an adjusted *weight*. A similar biasing technique is also existing for hadronic processes.

Weight Windows: In order to constrain *weight* fluctuations by prior *biasing*, this technique sets an upper and a lower *weight* limit. When the *weight* of a particle surpasses one of these limits particle splitting or Russian roulette is applied to force the particle back in the set *weight window*. The *weight* limits can be set particle and energy-dependent. *Weight windows* should be used together with other *biasing* techniques that are able to produce big *weight* fluctuations.

Additionally, calculation time can be saved by setting *production* and *transport cut-offs* for individual particle types. Particles below the thresholds are not transported anymore and their remaining energy is deposited directly by distributing it scaled by the particle's range continuously in the movement direction of the particle. This is of course not "physical", but if the *cut-offs* are low enough it has little impact on the results, and at the same time it can reduce the calculation time considerably.

4. Technical Implementation of the Beam Loss Monitoring System

This chapter describes the structure of the BLM system, giving details about the used detector types and the electronic data acquisition chain.

4.1. Principles of Ionization Chambers

An ionization chamber (IC) is a cavity between two electrodes filled with gas [Blu93, Mni04]. A high voltage is applied to the electrodes to create an electric field inside the chamber. A charged particle passing through this gas will ionize single gas molecules. The loss of kinetic energy due to interaction of the incident particle itself is in the range of some keV/cm and thus for most cases of interest negligible. The number of electron-ion pairs created scales with the path lengths traveled inside the chamber. The creation of electron-ion pairs is due to the EM force and depends on the charge of the particles. It is almost independent on the mass of incident particles.

Due to the strong electric field between the electrodes, created ions and electrons are accelerated toward the cathode and anode, respectively. By moving toward the electrodes they induce a current. Upon reaching a certain energy by this acceleration, electron-ion pairs created by incident primary particles are by itself capable of ionizing gas molecules (secondaries). This leads to an exponential multiplication of the originally created charge which is mainly due to the accelerated electrons. This charge multiplication is referred to as avalanche effect. The order of this amplification is typically in the range of $10^4 - 10^6$ and results in a measurable magnitude of charge for a single passing particle. This secondary ionization can also take place when a charged particle excites an atom, which in turn ionizes another atom during its de-excitation.

IC's are only operated at the *plateau region*, see Fig. 4.1. In this region all initially created charge is collected by the electrodes and a variation of the electric field within this regime does not influence the response of the chamber.

W-factor

To relate energy deposition in a gaseous detector to the amount of charges created, one can quantify the average energy required to produce an electron-ion pair, defined as W-factor E_W [Kno00].

In order to ionize a gas molecule, an incoming particle has to transfer an amount of energy at least equal to the ionization energy of the gas molecule. For nitrogen gas N_2 the first ionization potential is for example about 15.5 eV. There are other effects by which an impinging particle can lose energy without creating an electron-ion pair. For example by exciting an inner shell electron to a higher bounded state. It has to be accounted for such energy losses in the gas, not resulting in an ionization process. The feature that makes the W-factor important

4. Technical Implementation of the Beam Loss Monitoring System

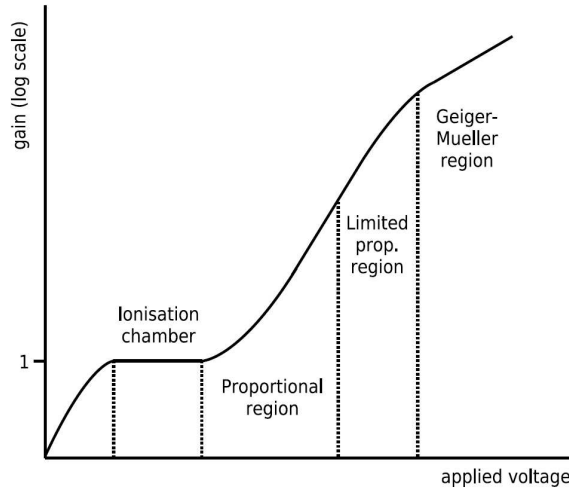


Fig. 4.1.: Operational regimes of a gaseous detector depending on its electric field. Gain is the ratio between the charges collected by the detector and the initially created charges by the incident particle.

for radiation dosimetry is that it is very insensitive to the mass and energy of the ionizing particle, given that the velocity of the particle is large compared with the orbital velocities of the valence electrons in the absorber molecules. Thus, for most cases of interest it can be considered to be constant. A constant W -factor results in a proportional relation between deposited energy in the gas and number of electron-ion pairs created. W -factors for different gases are typically in the range from 25 to 35 eV per electron-ion pair.

4.2. Principles of Secondary Electron Emission Detectors

A charged particle that passes through a metal excites conduction band and valence electrons. As these electrons have typically energies lower than 50 eV, independent of the primary particle's energy and type, they have a diffusion length in the nm-scale. When applying a bias voltage to electrodes, only secondary electrons close to the surface of the cathodes can leave it and drift away due to the electric field. The so-called secondary electron emission yield (SEY) measures the number of released electrons per surface-crossing particle. For the used SEM detectors the SEY is roughly about 10%. A quantitative model of the response of the LHC secondary emission monitor (SEM) can be found in [Kra07, Kra08].

4.3. Detectors and Electronics of the BLM System

LHC Ionization Chambers and Secondary Emission Monitors

The specifications for the detectors used for beam loss monitoring are a high dynamic range, and a high reliability. Further, they must be radiation tolerant, up to 70 MGy/year, with a life time of about 20 years which is in the order of the estimated LHC operation duration. IC's were chosen for this purpose. The high intensity range of losses was covered by installing less sensible SEM's in high-loss regions, i.e. near collimators. For high fluencies IC detectors are subject to space-charge effects resulting in a non-proportional signal. For a closer discussion of space charge see [Sto07].

4. Technical Implementation of the Beam Loss Monitoring System

Property	BLM IC	BLM SEM
Length	50 cm	11.3 cm
Diameter	8.9 cm	8.9 cm
Sensitive region	1524.16 cm ³ †(N ₂)	2 · 40.72 cm ² *(TiO ₂)
Pressure	1.1 bar	Vacuum
No. of electrodes	61	3
Electrode spacing	5.75 mm	5.75 mm
Electrode thickness	0.5 mm	0.25 mm
Electrode diameter	75 mm	75 mm
Standard bias voltage	1500 V	1500 V

†: cylinder between electrodes, *: surfaces of signal electrode

Tab. 4.1.: Dimensions and properties of IC and SEM used in the BLM system for the LHC.

Design and properties of the IC's and SEM's of the LHC BLM system are described in more detail in [Sto07, Kra08]. Tab. 4.1 lists some of the principal design parameters. Fig. 4.2 displays the inner structure of the IC and the SEM.

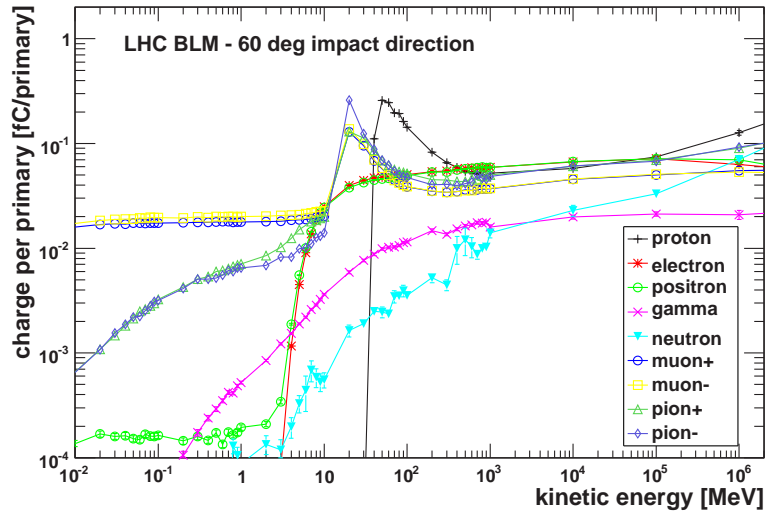


Fig. 4.2.: Inner structure of an IC (left) and inner structure of a SEM (right).

Depending on the loss location of primary protons in the LHC and the local geometry, IC's and SEM's will be exposed to different radiation fields. In order to determine the signal of the IC and the SEM, their response as a function of incident particle type, its energy, and the angle of the impinging radiation was simulated and compared with measurements [Sto07, Kra08]. Fig. 4.3 shows simulated response curves of an IC and a SEM at an angle of 60° and 0°, respectively. The charge created in the IC per primary was derived by converting the average deposited energy for a certain particle type and energy predicted by the simulation with a W-factor E_W of 34.8 eV. For the IC, absolute signal heights were found to differ by a factor of about 2, comparing the longitudinal and the transversal response of the chamber. This is primarily due to the different path lengths of the particles inside the detector electrodes and rod materials. Response curves of protons, muons, and pions each show a sharp cut-off at lower energies as they are absorbed below their specific energy thresholds in the chamber walls, not entering the sensitive volume. The signal of the SEM detector in units of charges was derived by modeling induced current due to the secondary emission yield (SEY) and the balance of incoming and outgoing charges at the signal electrode. For a detailed description see [Kra08]. As for the IC spectra, the cut-offs in the SEM spectra are due to absorption in the detector wall and internal components, other than the signal electrode.

4. Technical Implementation of the Beam Loss Monitoring System

a)



b)

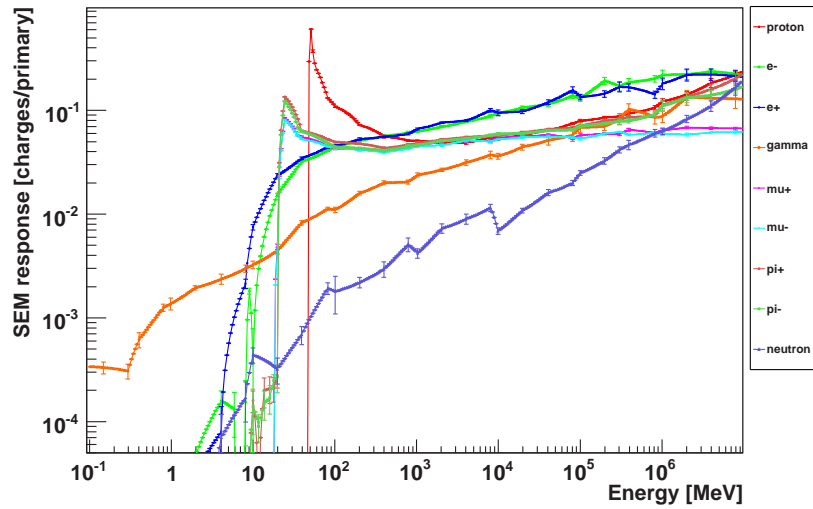


Fig. 4.3.: a) Simulated response curves of an IC for particles incident at an angle of 60° , taken from [Sto07]. Kinetic energy of the particles ranges from 10 keV to 1 TeV.

b) Simulated response curves of a SEM for a mean incident angle of 0° , taken from [Kra08]. Kinetic energy of the particles ranges from 100 keV to 10 TeV.

4. Technical Implementation of the Beam Loss Monitoring System

The signal ratio of charges created per track fluence for IC and SEM is

$$\frac{\left(\frac{dQ}{dF}\right)_{SEM}}{\left(\frac{dQ}{dF}\right)_{IC}} = 6.9 \cdot 10^4 \quad . \quad (4.1)$$

The conversion of charges collected by the BLM detectors to dose in the detector region is described in App. F.

Data Processing and Electric Readout of Detector Signals

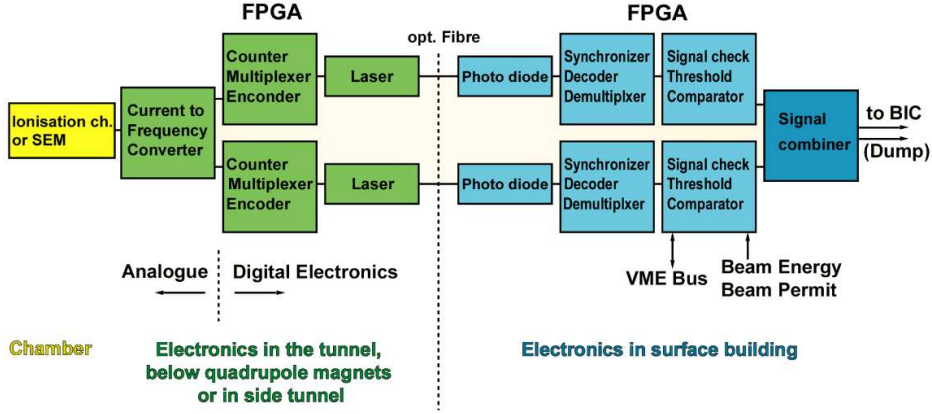


Fig. 4.4.: Transmission chain of the BLM signal, courtesy of B. Dehning.

The schematic structure of the BLM signal transmission can be seen in Fig. 4.4. The signal of the BLM detectors is sent to the radiation tolerant front-end electronics (BLMCFC's) which are located in the LHC tunnel. The data of the front-end electronics is transmitted to the surface via two (redundant) optical fibers. There it is compared by a data acquisition board (BLMTC) to predefined thresholds which can be set individually for each detector for all twelve monitored time spans (see later) and 32 different beam energy intervals.

The BLMCFC signal acquisition cards digitize the charge deposited in the detectors by a CFC (current-to-frequency converter). Fig. 4.5 a) depicts the functional principle of such a CFC [Fri02]. Induced signal current is integrated to charges by an analog integrator. It is then discharged via the reference current source. Fig. 4.5 b) displays the typical analog output voltage for a constant input current, almost at the maximum value of the operating range. In case of a positive input current, the voltage ramps negative. When reaching a fixed threshold voltage V_{tr} , the so-called *one-shot*, see Fig. 4.5 a), connects the integrator with the reference current source I_{ref} for a fixed time interval ΔT , giving an electronic pulse. As consequence, the integrator current is driven back and the output voltage increases. Once the reference current I_{ref} is disconnected, the integration cycle starts again to ramp down.

Every time the capacitor is discharged the *one-shot* adds 1 count ($\hat{=} 1024$ bits) to a counter which is read out every $40 \mu s$. The maximum number of counts in one acquisition interval of $40 \mu s$ is 255. For the IC's without filters this leads to a "saturation of the electronics" at 22 Gy/s or $0.88 \text{ mGy per } 40 \mu s$, see also Fig. 5.19. The relation between output frequency f

4. Technical Implementation of the Beam Loss Monitoring System

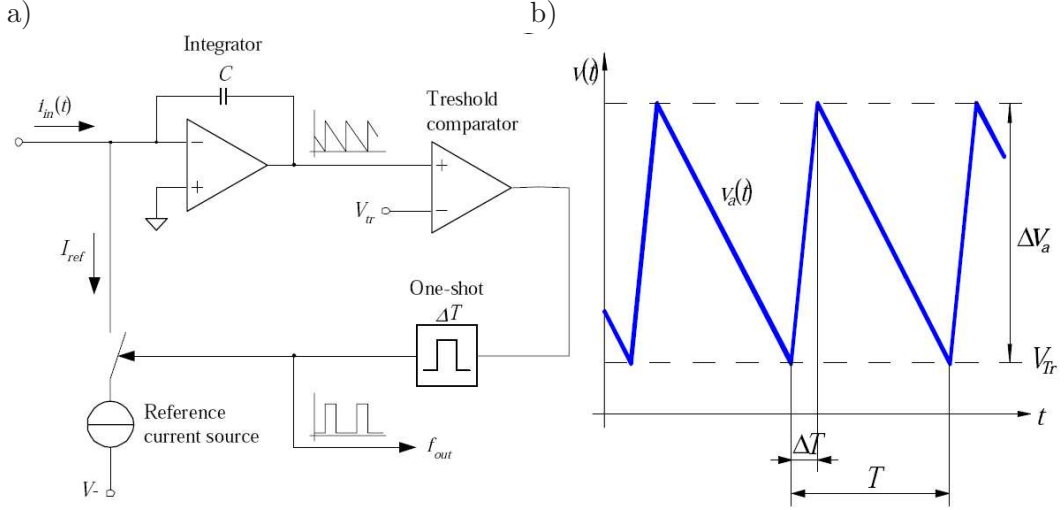


Fig. 4.5.: Principle of a CFC circuit, taken from [Fri02]. a) Depicts the basic circuit. b) Shows output voltage of the integrator for a signal current which is close to the maximum current handled by the circuit.

and detector current i_{in} is given by

$$f = \frac{i_{in}}{I_{ref} \Delta T}. \quad (4.2)$$

To extend the dynamic range of the CFC, an ADC (analog-to-digital converter) measures the integrator output voltage of the CFC at the time of the counter readout. The difference of the last two of the ADC readings is then used to add the fraction of a count in bits to the last $40 \mu\text{s}$ -value. The $40 \mu\text{s}$ -values are summed by twelve different running sums (RS's) each monitoring accumulated losses during a time span reaching from $40 \mu\text{s}$ to 84s , see Tab. 4.2.

Thresholds set for different time windows cover different loss durations reaching from *fast losses* to *intermediate losses* (see Fig. 1.4). The data from the BLMTTC is continuously logged every second. Further, high losses leading to an extraction of the beam trigger the acquisition of post mortem (PM) data readouts containing the $40 \mu\text{s}$ -values of all twelve RS's over 80ms for offline analysis. A more detailed description of the technical implementation of the data acquisition and processing can be found in [Zam05, Zam06].

4. Technical Implementation of the Beam Loss Monitoring System

Signal name	Time window		Refreshing rate [ms]	Data type
	Δt_i [ms]	$40 \mu s$ steps		
RS1	0.04	1	0.04	max.
RS2	0.08	2	0.04	max.
RS3	0.32	8	0.04	max.
RS4	0.64	16	0.04	max.
RS5	2.56	64	0.08	max.
RS6	10.24	256	0.08	max.
RS7	81.92	2048	2.56	max.
RS8	655.36	16384	2.56	max.
RS9	1310.72	32768	81.92	sum
RS10	5242.88	131072	81.92	sum
RS11	20971.52	5242288	655.36	sum
RS12	83886.06	2097152	655.36	sum

Tab. 4.2.: Twelve running sums (RS's) are storing the losses for their corresponding time interval. When written to the logging data base shorter time intervals marked with 'max.' contain the maximum RS value of the last second, whereas RS's with time spans longer than one second store the sum of the $40 \mu s$ values over their time interval.

5. Beam Losses at the LHC Collimator mounted in the SPS

In this chapter experimental data, acquired in an LHC collimation-like installation in the SPS ring, is compared to the prediction of detector signals by simulations with FLUKA. This allows to evaluate the overall accuracy of predicting the signal of BLM detectors by simulations with a radiation field similar to the one expected in the LHC collimation area. The study includes an estimation of deviations of the BLM signals due to simplifications and misalignment of the geometry in the simulation, different physics parameters of the simulation, calibration of the signal of the BLM detectors, and uncertainties for the beam impact scenario. It enables to assess the accuracy of threshold predictions for the BLM detectors in the LHC collimation setup. Further, the setup allows to investigate the dependencies of the BLM signals on initial parameters, such as beam profile, intensity, and impact position. The experimental data was taken at SPS injection energy of 26 GeV. This method allowed to direct the beam on the collimator with different mean impact parameters, depending on the position of the collimator jaw with respect to the beam.

5.1. Description of the Experimental Setup

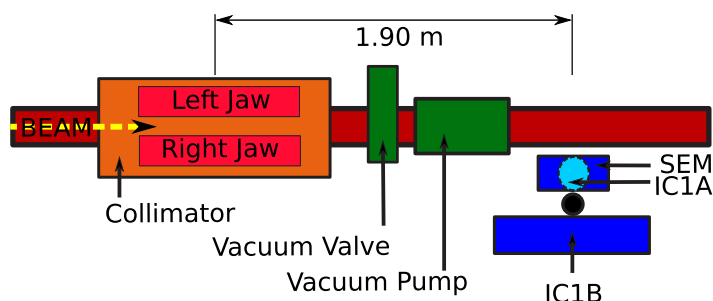


Fig. 5.1.: Schematic top view of the LHC collimator in the SPS and the BLM detectors. The beam impacts on the jaws of a horizontally mounted secondary collimator (TCSG). Two IC's and one SEM detector are mounted downstream of the collimator. The beam pipe between collimator and detectors contains a vacuum valve and a vacuum pump.

In the SPS LSS5 (Long Straight Section 5) an LHC prototype secondary graphite collimator (TCSG) is mounted for test purposes. About 1.9 m (middle-to-middle) downstream of this collimator a set of BLM detectors is installed, consisting of two IC's and one SEM. Fig. 5.1 and Fig. 5.2 depict a schematic drawing and a photo of the setup, respectively. One IC is mounted in a vertical position with respect to the beam pipe (BLM IC1A), and a second one is mounted parallel to the beam pipe (BLM IC1B). The shorter SEM is installed parallel to the beam pipe at the height of the beam. IC1A and the SEM are located in a similar position with respect to the collimator as in the standard LHC collimation installation (see

Chapter 6). The BLM detectors are connected to the BLM data acquisition system. The position of the collimator is set by a control software for the LHC collimators.

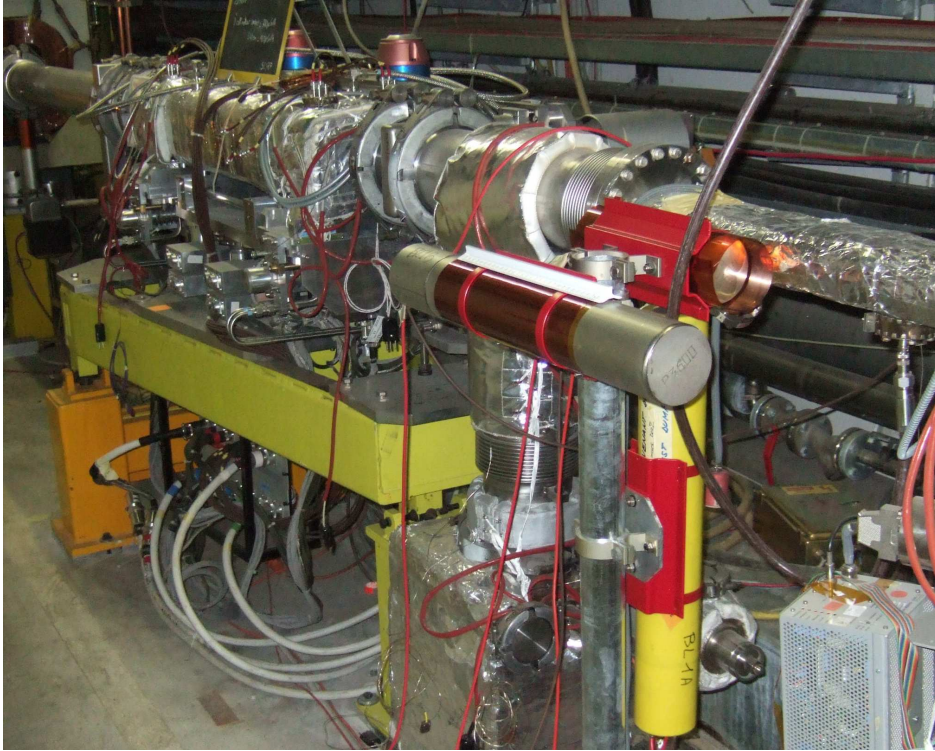


Fig. 5.2.: Collimator and BLM setup in SPS LSS5 looking upstream. The LHC prototype collimator, wrapped by heating jackets (silver), is mounted on a support mainly composed of steel (yellow). The stand with the IC's and the SEM can be seen in the front. The beam pipe between collimator and BLM support contains a vacuum valve and a vacuum pump which is placed under the beam pipe.

5.2. Preparation of the Simulation

At first, the implementation of the experimental setup at the SPS in the Monte Carlo code FLUKA is described. Furthermore, the calibration of the FLUKA physics settings, studies done for misalignment, and not precisely known model parameters are discussed.

5.2.1. Implementation of Geometry and Materials

The section of the SPS LSS5 containing the LHC collimator and the set of BLM's was modeled in FLUKA. The total length of the geometry is about 5 m and extends to the concrete tunnel wall of the SPS. Special focus was put on the crucial sections of the collimator (where the first impact onto matter occurs), the beam tube, and the BLM detectors¹ [Sal07]. Materials and material properties of the collimator and the BLM detectors were carefully chosen and are in agreement with the design specifications. The positioning of the BLM monitors with respect to the collimators is exact up to maximum 3 cm. Instrumentation and supports in vicinity were included making some simplifications in geometry and assuming standard materials such

¹Detailed geometry files of the IC and the collimator were kindly provided by the FLUKA team.

5. Beam Losses at the LHC Collimator mounted in the SPS

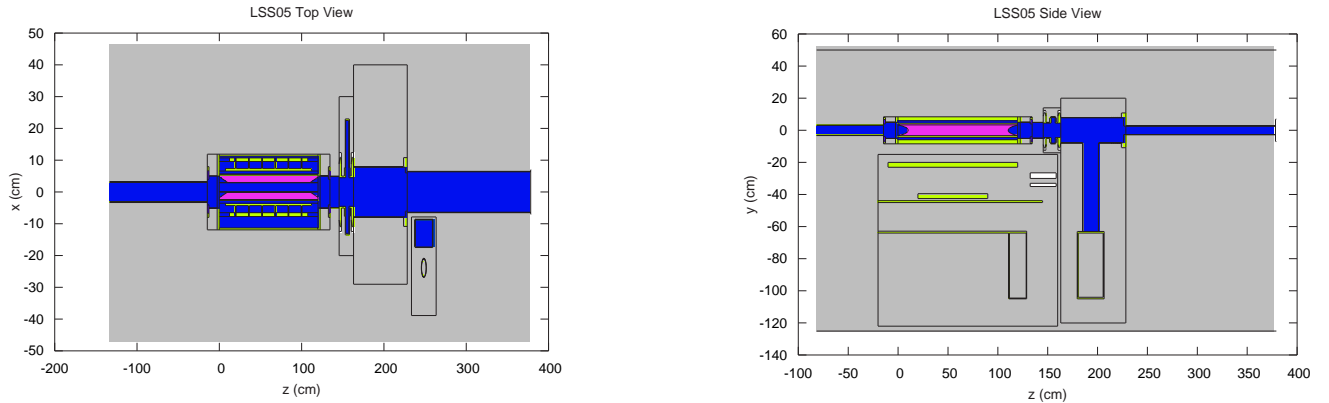


Fig. 5.3.: Geometry of the experimental setup as implemented in FLUKA. Left [right] figure shows a lateral cut in the horizontal [vertical] plane through the beam center. Collimator jaws are pink, air is gray. The grey boxes mark the size of the different *prototype*-components copied into the geometry.

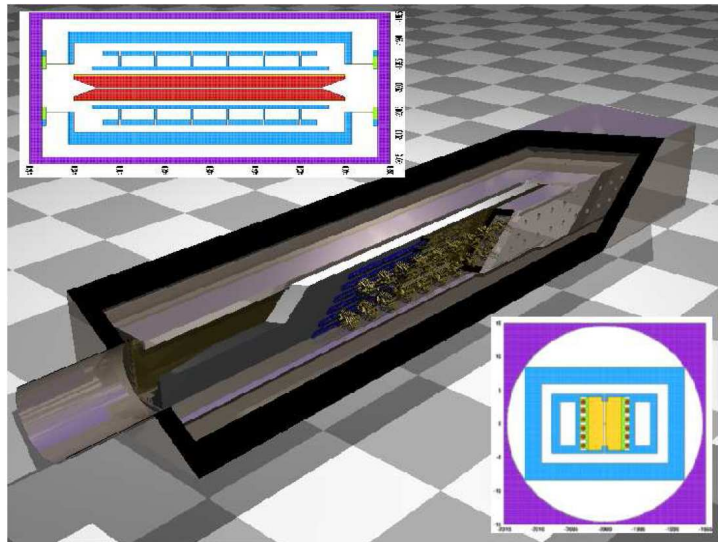


Fig. 5.4.: Rendered 3D view of the TCSG collimator together with two cross-sectional views, as implemented in FLUKA, taken from [Mag06].



Fig. 5.5.: Rendered 3D view of the ionization chamber (IC) as implemented in FLUKA, taken from [Sar07].

5. Beam Losses at the LHC Collimator mounted in the SPS

Detector	Scored quantity	Scoring volume [cm ³]	Material	ρ [g/cm ³]
IC	Energy [GeV] in vol.	1520.00	N ₂	0.0013
SEM	Energy [GeV] in vol.	1191.43	Air	0.0012

Tab. 5.1.: Settings for energy deposition scoring in the detectors. The scoring area of the IC is the volume between the electrodes. The SEM detector was approximated by a cylinder with an outer radius of 44.5 mm, and a height of 21.9 cm. It has a thickness of 2 mm for the wall, and 5 mm for the end-caps.

as steel, and aluminum. Uncertainties due to these simplifications were assessed with variation studies (see later). Fig. 5.3 depicts cross-sectional views of the geometry. Fig. 5.4 and Fig. 5.5 show detailed pictures of the implementation of the TCSG collimator and of the IC, respectively. A modular approach was used for the FLUKA implementation, yielding a bigger flexibility: components were build as a whole in a separate construction area (*prototypes*) and then copied to their real position in the geometry (*replicas*). This approach allows for modeling collimator jaws with a detailed geometry and making them at the same time easily movable, as in this manner only a small amount of parameters has to be changed manually for each setting of the jaws.

5.2.2. Recorded Quantities

Particle fluencies through the BLM detector volumes are recorded, and energy deposited in the IC's and the SEM is scored. For both, IC and SEM detector, the energy deposition is converted into dose. For the IC this is done for the sensitive volume filled with nitrogen gas between the electrodes. The volume of the SEM detector is filled with air. Energy deposition in this cylindric volume is also converted in dose and is then compared to an *equivalent dose* for a given charge deposition in the SEM; calculated in [Kra08]. Tab. 5.1 gives some details about the implementation of the scorings. The conversion of detector signal in dose rate is described in App. F. In addition, also particles leaving the geometry through the beam pipe are scored and their properties are written in an extra file.

5.2.3. Returning Beam Protons

The experimental setup was such that the beam was in circulating mode in the SPS while impacting on the collimator. With a collimator jaw moved partly into the beam, this leads to a reduction of the horizontal (x) phase-space area of the beam particles. Fig. 5.6 illustrates the removal of beam particles by a collimator after one and two passages. Multiple passages of the beam result finally in a round cut in normalized phase space. In the simulations it has to be accounted for protons that return after an initial passage of the collimator as all quantities are scored “per simulated primary proton”.

Protons missing the collimator jaw Beam protons that do not interact in the collimator during their initial passage due to their horizontal position, can hit the collimator in a successive turn. The ratio of *lost protons* to injected protons is known for the experiment by the beam intensity measurements. For the simulations, beam distributions were cut so that all *primary* protons impact on the collimator jaw. This assumes that returning protons hit the jaw with the same impact distribution as the initial one.

5. Beam Losses at the LHC Collimator mounted in the SPS

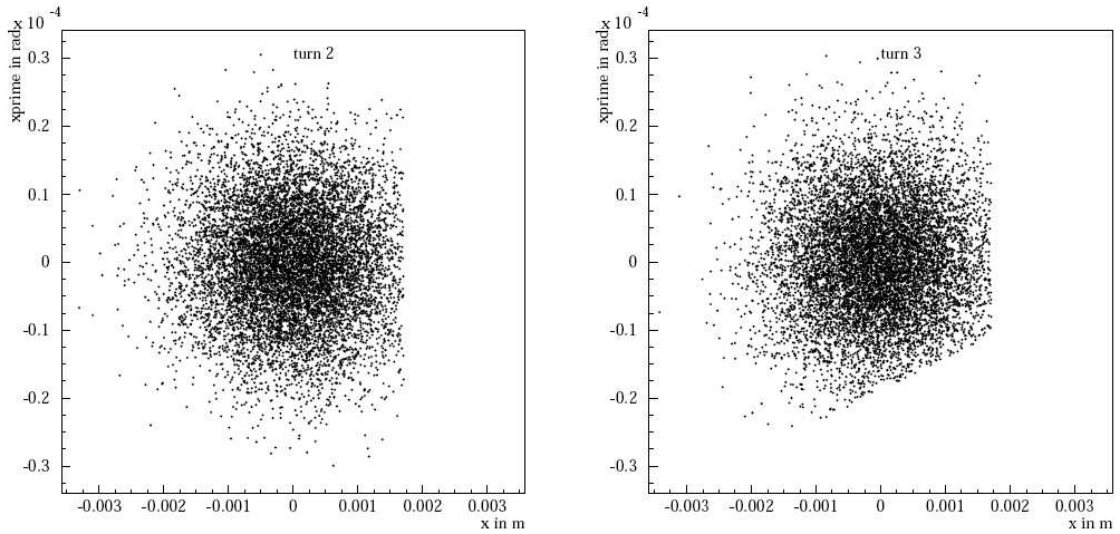


Fig. 5.6.: Normalized phase-space plot of beam particles at a collimator after one and two turns, taken from [Bur04]. Simulated particles are removed from an initially Gaussian-distributed beam ($\sigma_x = 0.855$ mm) by a collimator jaw at $x = 2\sigma_x = 1.71$ mm. An nominal SPS tune of $Q_x = 26.18$ was assumed. The left graph (“turn 2”) shows the distribution after the first passage of the collimator. The right graph (“turn 3”) shows the distribution after the second passage.

Edge escape Additionally, impacting protons which are only slightly elastically scattered while traversing the jaw have to be considered. They alternate just marginally their transversal and longitudinal position in phase space, and hence, might hit the collimator in successive turns. This fraction of slightly scattered protons at 26 GeV is small². But protons which are impacting close to the surface of the collimator jaw can be scattered out of it before traversing the full length of the collimator jaw. This effect, the so-called *edge escape*, is noticeable only for small impact parameters starting from about $10 \mu\text{m}$.

ploc : In the following, the term *lost proton*, or particle lost on collimator N_{ploc} will refer to protons that impact on the collimator jaw and are there sufficiently scattered to be intercepted by the SPS aperture limits within the next turn.

poc : Protons on collimator N_{poc} refers, less exclusively, to protons which impact on the collimator jaw.

To account in the simulations for protons which “survive” the initial passage at the collimator jaw to hit it in a successive turn, protons that leave the geometry inside the beam tube are scored. By comparing their energy with the energy aperture of the SPS and their emittance with the admittance of the SPS, the fraction of returning protons F_{ret} is estimated. Tab. 5.2 lists the apertures of the SPS. This is just a rough approximation as it is not accounted neither for the phase ϕ of protons at the aperture limitations, nor for the combined effect of aperture limitation and dispersion³. To assess uncertainties involved in this approximation,

²Material parameters of the collimator jaw at 26 GeV: $\lambda^{\text{inel}} = 46.8$ cm, $\lambda^{\text{el}} = 122$ cm, and $X_0 = 24.12$ cm.

³To do so would require to feed the exiting particles into an optical tracking code, such as SIXTRACK or MADX, with SPS optics.

5. Beam Losses at the LHC Collimator mounted in the SPS

SPS Apertures	
Energy $\left(\frac{\Delta E}{E}\right)_{\text{ape}}$	≈ 0.01
$\left(\frac{\pi x(s)^2}{\beta_x(s)}\right)_{\text{min}}$	$213.90 \pi \cdot \text{mm} \cdot \text{mrad}$
$\left(\frac{\pi y(s)^2}{\beta_y(s)}\right)_{\text{min}}$	$32.47 \pi \cdot \text{mm} \cdot \text{mrad}$

Tab. 5.2.: Apertures of the SPS: the maximum deviation from the nominal energy and admittance for particles in x and y directions.

the numbers of Tab. 5.2 where multiplied by a factor of 0.5 and 2.0, and the change in F_{ret} was monitored. The approximation proved sufficient for most of the intended analysis (maybe with the exception of *continuous scraping*, see Section 5.3.8), as corrections are mostly small (below 1%).

Scored quantities from the simulations are rescaled properly by the fraction of returning particles F_{ret} to yield comparable values to the experiment of dose per *lost proton*, or dose per N_{ploc} . The rescaling is done by the factor

$$F_{\text{res}} = \sum_{n=0}^{\infty} (F_{\text{ret}})^n = \frac{1}{1 - F_{\text{ret}}}, \quad (5.1)$$

resulting of a geometric series where n is the number of turns.

5.2.4. Monte Carlo Statistics, FLUKA Physics Settings, and Biasing

Generally, statistical errors for the simulation were kept $\lesssim 5\%$ by adjusting the number of primary protons accordingly. To have sufficient statistics in the scoring regions of interest, i.e. sensitive volumes of the BLM detectors, a number of 100 000 primary protons per configuration proved to be sufficient for most cases. For some cases up to 400 000 primaries were needed.

FLUKA-internal *production* and *transport thresholds* (see Section 3.3.2) for γ 's, e^{\pm} 's, p 's, μ^{\pm} 's, and $\pi^{0,\pm}$'s were varied by factors of ten to find a compromise between computational effort and exact physics⁴. This was done for a 26 GeV proton beam impacting on the collimator jaw. Tab. 5.3 shows the threshold settings. Setting 3 was chosen for further simulations as no significant changes in energy deposition was observed while computational time increases considerably for lower thresholds.

To increase statistics in the regions of the BLM detectors, *surface splitting* (see Section 3.3.2) was used to augment the particle multiplicity in two steps by a total factor of ten. Further, *leading particle biasing* (see Section 3.3.2) was employed globally to all e^{\pm} and γ -interactions to reduce the amount of electromagnetic particles produced and transported by the simulation. There is an excess of these particles due to electromagnetic showers. The energy thresholds for starting *leading particle biasing* for both e^{\pm} 's and γ 's, were set to 1 GeV.

5.2.5. Variation Studies

To evaluate sensitivity of the results of the simulations to not precisely known model parameters, such as misalignment of the components and simplification of the geometry, crucial

⁴Thresholds for neutrons were not varied. Interactions of neutrons below 19.6 MeV are calculated by FLUKA with tabulated cross-sections based on experimental data (see Chapter 3).

5. Beam Losses at the LHC Collimator mounted in the SPS

Setting number	Threshold type	Particle type with kinetic energy		
		γ [MeV]	e^\pm [MeV]	$p, \mu^\pm, \pi^{0,\pm}$ [MeV]
0	Prod.	0.333	1.511	
	Trans.	0.333	1.511	10
1	Prod.	0.1	1	
	Trans.	0.01	0.1	1
2	Prod.	0.01	0.1	
	Trans.	0.001	0.01	0.1
3	Prod.	0.001	0.01	
	Trans.	0.0001	0.001	0.01
4	Prod.	0.001	0.01	
	Trans.	0.0001	0.001	0.005
5	Prod.	0.001	0.01	
	Trans.	0.0001	0.001	0.001

Tab. 5.3.: Settings for FLUKA *production* and *transport thresholds* used to investigate the changes in BLM detector responses.

parameters were scanned and the change in energy deposition in one of the IC's (BLM ICA) was monitored. This study was done with the left jaw at -30.9 mm and the right jaw at -4.1 mm. Following model parameters were modified:

- ★ The components of collimator support were replaced by air (5% change), and the whole support volume was replaced by a steel block (-15% change).
- ★ Minor changes in details of the vacuum valve and parts of the beam tube⁵ resulted in not significant changes of energy deposition in BLM ICA of $< 3\%$.
- ★ Horizontal misalignment of the IC of ± 10 mm changed the energy deposition by maximum 2%.
- ★ A change of the vertical beam impact position on the collimator of ± 5 mm changed the IC response by maximum 1%.
- ★ Investigating the influence of the size of the beam profile to the signal, the beam size was scanned, see Fig. 5.7 a). The beam center was impacting at 4.1 mm and vertical and horizontal beam sizes were changed. Maximum IC signal variation was 11% for the triple beam size. The change of the BLM detector response shows a low dependency on the beam size, given that the beam center hits deep in the jaw.

5.2.6. Impact Parameter Scan at 26 GeV

Protons with very small impact parameters can be scattered out of the jaw before traversing the whole jaw or undergoing an inelastic interaction. As mentioned before this effect is referred to as *edge escape*. To determine the change of the BLM signal as a function of the impact parameter, simulations with a *pencil* beam, that is a beam with no transversal

⁵Exact geometry was not known, as no technical drawings were provided.

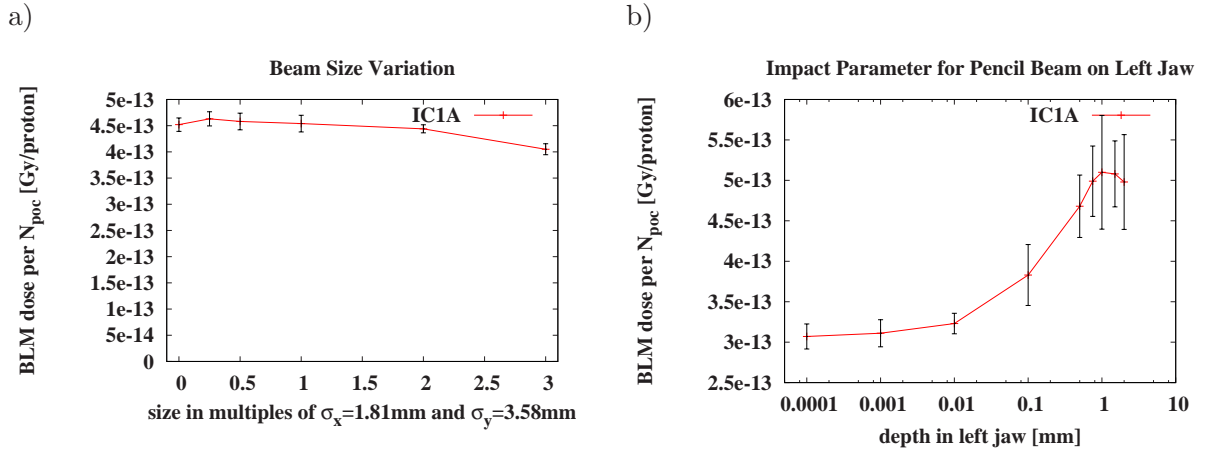


Fig. 5.7.: a) Normalized BLM signal versus beam size. A Gaussian beam profile is varied in multiples of the beam size calculated in Tab. 5.6.

b) Normalized BLM signal versus impact parameter. Simulation was done with a *pencil* beam impacting on the left collimator jaw at 26 GeV. The signal increases when hitting deeper into the jaw.

extension, were done at 26 GeV. These simulations give an indication for the sensitivity to the impact parameter of the whole beam. Simulations were done with a perfectly flat jaw surface and a beam-jaw angle of zero. Thus, values for small impact parameter have to be considered with caution. Fig. 5.7 b) shows the dependence of the IC1A detector signal on the impact parameter. As expected, the response per impacting proton is lower for small impact parameters due to *edge escape* – more particles are scattered out of the collimator jaw and are not any longer capable to initiate hadronic showers which give a contribution to the BLM signal. For different impact parameters there is a maximum signal change of about 60% with respect to the maximum value.

5.2.7. Particle Spectra in the BLM Detectors

Fig. 5.8 shows the differential track-length fluencies⁶ in the scoring volume of the BLM detectors for the particles contributing most to the signal of the IC and SEM detector, respectively. Spectra of IC and SEM are similar as they are mounted close to each other. The energy of these particles range up to about 10 GeV.

5.3. Measurements

5.3.1. SPS Beam Conditions and Acquired Data

Three measurement sessions were carried out for the collection of data in the SPS. The first two sessions were both mainly devoted to test measurements of the SEM. This explains the suboptimal conditions for IC acquisition, as discussed later.

The SPS beam conditions for the measurements are described in the following. Initially, the SPS was set up to operate in cycling mode with a period of 20 seconds, and a proton beam at injection energy of 26 GeV. At the end of the cycle the remaining beam was extracted

⁶That is track-length of particles of a certain energy in a scoring volume divided by this scoring volume.

5. Beam Losses at the LHC Collimator mounted in the SPS

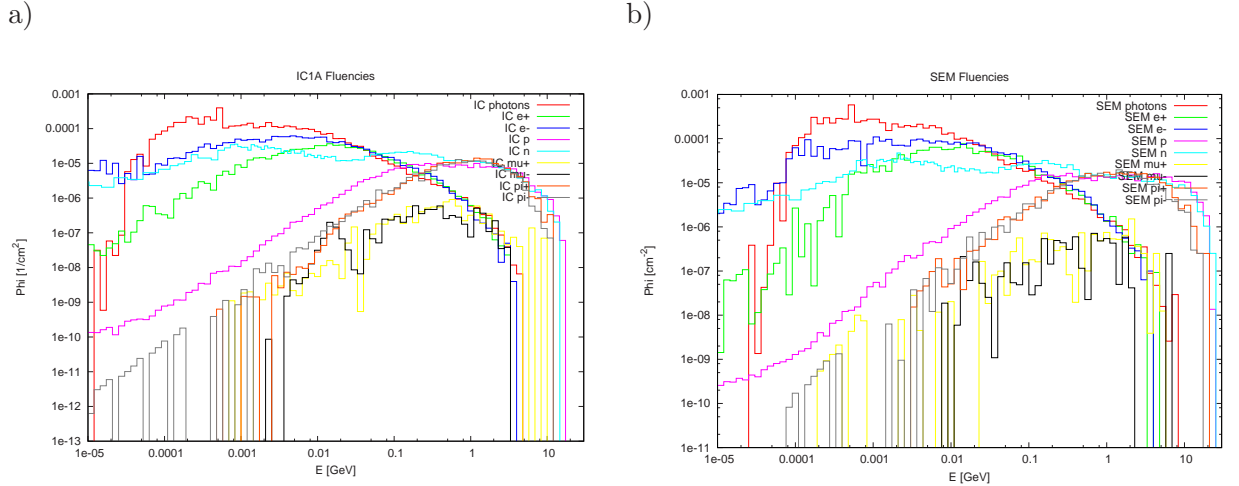


Fig. 5.8.: Track-length fluencies for a 26 GeV-beam in the IC1A (a) and the SEM detector (b) versus energy. Fluencies are given per primary proton.

to the SPS beam dump. Measurements were conducted during *flat bottom*⁷. Tab. 5.4 gives an overview of the beam conditions during the measurement sessions. The beam intensity was regulated in the SPS preaccelerator chain (see Chapter 1.1) via the number of particles per bunch and the number of bunches. The intensity of the beam was monitored during the measurement sessions by Beam Current Transformers (BCT's) in the injection line to the SPS, and in the SPS itself. In Session 3 also the beam oscillations in the SPS were measured by Beam Position Monitors (BPM's). Tab. 5.5 lists the devices used for data acquisition.

5.3.2. Overview of Data Analysis

This paragraph gives an overview of the data analysis done. All processes and their results are discussed in detail later. The data analysis of measurements splits in two parts. These are the measurement of normalized dose seen by the detectors, and the determination of parameters of the beam impact scenario for the comparison of the measured normalized doses by simulation.

Normalized Dose

The collimator is the smallest aperture in the SPS ring. Hence, protons are primarily lost on the collimator jaw⁸ and their showers generate a signal in the BLM detectors mounted downstream of the collimator.

The discussion below is dedicated to the measurements of the ratio of dose seen by the BLM detectors to the number of protons lost on the collimator N_{ploc} , or short the normalized dose, in:

$$\left[\frac{\text{Dose}_{\text{IC1A/IC1B/SEM}}}{N_{\text{ploc}}} \right] = \frac{\text{Gy}}{\text{proton}} . \quad (5.2)$$

⁷The time in the cycle after injection and before acceleration.

⁸To be more precise the minimal value of the aperture over the square root of the beta function is the significant value for loss locations; given that the dispersion is small.

5. Beam Losses at the LHC Collimator mounted in the SPS

Session	No. 1	No. 2	No. 3
Internal name	MD45	MD46	MD28
Date	08/11/2007	12/11/2007	09/07/2008
SPS settings			
Beam type	LHC 25 ns	Fixed Target	LHC 25 ns
Flat bottom [sec]	10.86	≈ 2.0	10.86
Horizontal tune Q_H	26.13 ± 0.01	26.62 ± 0.01	26.13 ± 0.01
Vertical tune Q_V	26.18 ± 0.01	26.58 ± 0.01	26.18 ± 0.01
Beam energy [GeV]		26	
Lorentz β_L		0.9994	
Lorentz γ_L		28.7186	
Momentum spread $\frac{\Delta p}{p}$		≈ 0.001	
No. of batches	1	1	1
No. of bunches	72	72	12/24/48/60/72
Injected intensity	$\approx 900 \cdot 10^{10}$	$\approx 1300 \cdot 10^{10}$	$\approx 10 - 90 \cdot 10^{10}$

Tab. 5.4.: SPS settings and beam properties for the three measurement sessions.

Session	No. 1	No. 2	No. 3
Devices type	Acquisition device name		
Transfer line BCT	TT2BCTFI	TT2BCTFI/TT10BCTFI	TT2BCTFI/TT10BCTFI
SPS BCT	BCTDC.41435	BCTDC.41435	BCTDC.31832/41435
SPS wire scanner	BWSA.51995	BWSA.51995	BWSH.41420.rot
SPS BPM	-	-	BPH.51808.H
BLM detectors	IC1A, IC1B, SEM	IC1A, IC1B, SEM	IC1A, IC1B, SEM
Collimator pos.	TCSP.51934	TCSP.51934	TCSP.51934

Tab. 5.5.: Devices used for the acquisition of data during the measurement sessions.

5. Beam Losses at the LHC Collimator mounted in the SPS

Two types of measurements were conducted, to determine the normalized BLM signal.

Direct dumping In the first type of measurements (see Section 5.3.7), the injected beam was directly intercepted by the collimator. The response of the BLM's was measured as a function of the collimator position while monitoring the beam intensity in the SPS via BCT's. In this series one collimator jaw was moved into the beam center in steps of 0.5 – 1.0 mm while the other jaw was kept at rest, completely withdrawn from the beam. The jaw was moved between two cycles when there was no beam in the SPS. The range of movement was from 30 mm down to –5 mm. Fig. 5.9 shows the example of such a measurement. As the jaw is positioned closer to the beam center, the number of particles intercepted by the collimator increases. After initial impact on the collimator, directly after injection, one observes a decay of the beam current. This loss is attributed to the capturing of the beam by the RF system together with beam diffusion and a slow repopulation of the horizontal phase space due to coupling in the transversal plane. Increased losses at later times, as seen in Fig. 5.9, are due to acceleration. At the end of the cycle the beam is extracted and the intensity decreases to zero.

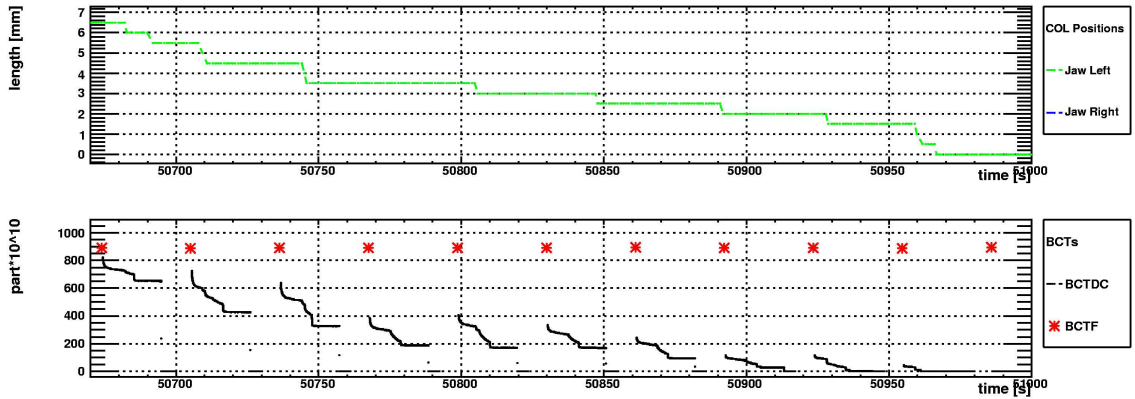


Fig. 5.9.: The upper graph depicts the position of the left collimator jaw versus time. For the same time span the second graph shows in red (*) the particle intensity measured by the fast Beam Current Transformer (BCT) in the transfer line to the SPS, and in black (—) the particle intensity measured by the BCT in the SPS. Data for a time span of ten and a half cycles is shown.

Continuous scraping In the second type of measurement series (see Section 5.3.8), the beam was injected with both of the collimator jaws withdrawn from the beam. During the injection plateau, one of the collimator jaws was moved continuously into the beam until the intensity of the circulating beam was zero. The integrated signal from the BLM's in the period of the collimator movement gives the total amount of signal from all protons lost on the collimator. Fig. 5.10 displays such a scraping done with the right collimator jaw.

Parameters of the Beam Impact Scenario

This part of the data analysis introduces beam parameters needed for reproduction by simulation. These parameters are:

5. Beam Losses at the LHC Collimator mounted in the SPS

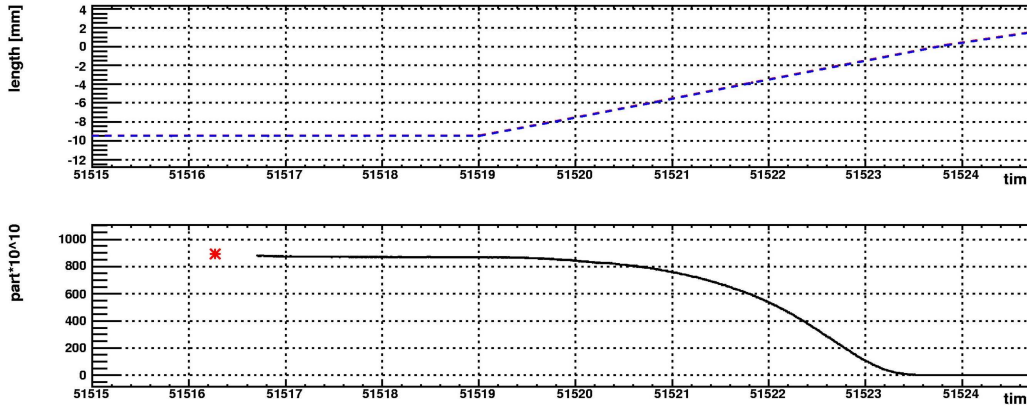


Fig. 5.10.: Scraping of the beam with the right collimator jaw. The upper graph shows the position of the right collimator jaw versus time. The lower graph shows for the same time in red (*) the particle intensity measured by the fast BCT in the transfer line to the SPS, and in black (—) the particle intensity measured by the BCT in the SPS. The beam intensity decays as the collimator is moved toward the beam center.

- ★ the beam size at the collimator,
- ★ the mean beam impact parameter on the collimator,
- ★ and the proton impact parameter distribution for the *continuous scraping* process.

The transversal beam size in horizontal (x) and in vertical (y) direction at the collimator was determined by beam profile measurements by wire scanners (see Section 5.3.3). For verification, the horizontal beam profile was additionally determined by plotting the beam intensity versus the collimator jaw position for the *continuous scraping* process (see Section 5.3.4). This results in the beam intensity distribution and the beam position with respect to the collimator.

The position of the collimator with respect to the beam was also calibrated by moving the collimator jaw into the beam center step wise, in between the cycles, (*direct dumping*) until the beam is depleted (see Section 5.3.5).

The distribution of proton impact parameters for the *continuous scraping* process was calculated by an analytic model considering the collimator movement, drift and diffusion of beam particles, and coherent slow beam oscillations (see Section 5.3.6).

5.3.3. Calculation of the Beam Profile at the Collimator with a Wire Scanner

By measuring the Gaussian-like beam profile with a wire scanner, the emittance and the transversal rms beam size $\sigma_{x,y}$ at the collimator position was determined. An example of a wire scanner measurement is shown in Fig. 5.11. The rms beam size σ measured by the wire scanner together with the Courant-Snyder parameters at the wire scanner and the collimator position were then used to calculate the beam size at the collimator. This was done calculating the rms emittance ϵ of the beam by using the relation

$$\sigma = \sqrt{\frac{\epsilon\beta}{\pi} + D^2 \left(\frac{\Delta p}{p}\right)^2}, \quad (5.3)$$

5. Beam Losses at the LHC Collimator mounted in the SPS

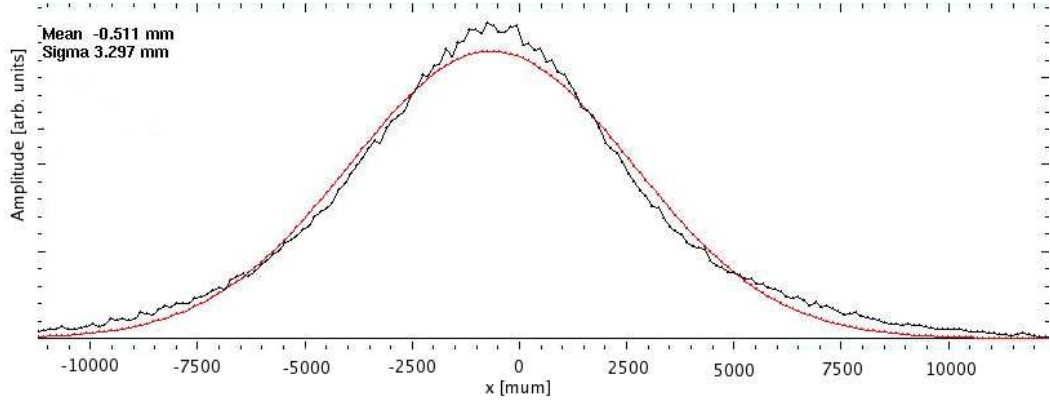


Fig. 5.11.: Horizontal beam profile measured by a wire scanner in the SPS. Data is in black (—). The red line (—) is a Gaussian fit to the data.

Position	s [m]	β_x [m]	D_x [m]	β_y [m]	D_y [m]	σ_x [mm]	σ_y [mm]
Wire scanner	5242.54	81.494	-0.015	28.150	0.0	3.25	2.01
Collimator	5221.78	24.848	-0.215	89.766	0.0	1.81	3.58

Tab. 5.6.: SPS Courant-Snyder parameters and beam size at the collimator and wire scanner (BWSA.51995) for Session 1. These measurements of the beam profile by a wire scanner were used to determine the size of the beam at the collimator.

with the β -function β and the dispersion function D at the place of the wire scanner. $\frac{\Delta p}{p} \approx 0.001$ is the momentum spread of the beam. Eq. 5.3 was then used again with β and D at the collimator to calculate the beam size σ at the collimator. A summary of beam optics and related Courant-Snyder parameters can be found in App. G. Relevant Courant-Snyder parameters and results from calculations for Session 1 are listed in Tab. 5.6. Assuming for β an error of $\Delta\beta/\beta = 20\%$ results in an uncertainty of about 14% for the beam size at the point of the collimator. Calculations for the following sessions were done analogously. For the last session only the horizontal beam size was measured, as the vertical particle distribution was simulated to have little impact on the BLM signal (see Section 5.2.5). Tab. 5.7 lists the beam sizes determined for all three sessions.

Session	No. 1	No. 2	No. 3 12/72 bunches
Hori. σ_x [mm]	1.81	2.88	$4.96 \pm 0.26/3.23 \pm 0.11$
Vert. σ_y [mm]	3.58	4.29	-
Amplitude of initial beam oscillations [mm]	-	-	0.85
Collimator position calibration [mm]	1.5 ± 0.5	3.5 ± 0.5	2.25 ± 0.25

Tab. 5.7.: The first two rows list the beam size at the collimator measured by a wire scanner. The last two rows give the initial amplitude of beam oscillation determined by the Beam Positioning Monitors (BPM's), and the results of the collimator-beam orbit center calibration together with their uncertainties.

5.3.4. Measuring of the Horizontal Beam Profile by Scraping

For comparison with the wire scanner measurements, the beam profile at the collimator was measured by scraping the circulating beam with a collimator jaw.

Derivation of Intensity Distributions for Scraping

One can measure the transversal beam profile by scraping the beam with a collimator jaw. For this procedure the collimator jaw is moved slowly into the center of the beam. When plotting the fraction of particles lost on the collimator jaw versus the collimator position, the cumulative losses characterize the beam distribution in the scraping plane. The movement of the collimator can generally be considered stationary with respect to the scraping process.

A normalized two-dimensional Gaussian phase-space distribution writes

$$G_2(x, x') = \frac{1}{2\pi\sigma_x\sigma_{x'}} e^{-\frac{1}{2}((x-x_0)^2/\sigma_x^2 + x'^2/\sigma_{x'}^2)}, \quad (5.4)$$

where x and x' are the phase-space coordinates, σ_x and $\sigma_{x'}$ are the respective standard deviations, and x_0 is the mean value of the distribution in x .

In the following the error function will be noted as

$$\text{erf}(t) := \frac{2}{\sqrt{\pi}} \int_0^t e^{-x^2} dx, \quad (5.5)$$

It will be assumed that there is no dispersion. For a derivation including dispersion, see App. H. Dispersion can be neglected for the case of interest as it is small at the collimator (about 0.2 m).

The fraction of particles that are lost after a single-sided cut, see Fig. 5.12 a), at n_σ is equal to

$$F_{L,1}(n_\sigma) = \int_{-\infty}^{\infty} dx' \int_{n_\sigma\sigma_x+x_0}^{\infty} dx G_2(x, x') = \frac{1}{2} (1 - \text{erf}(n_\sigma)). \quad (5.6)$$

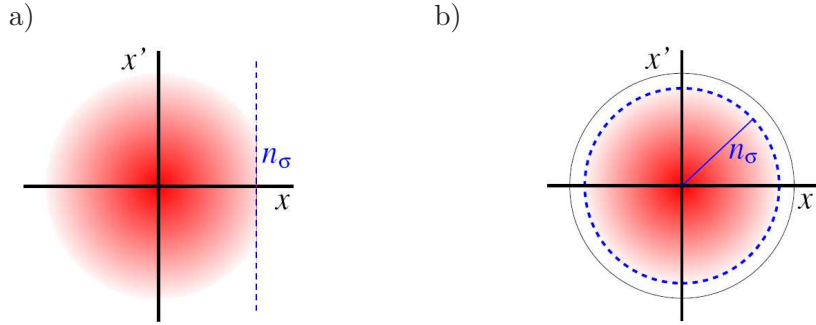


Fig. 5.12.: a) Single-side cut in normalized phase space at n_σ , taken from [Bur04].

b) Round cut in normalized phase space after many passages of not-scattered beam particles at a restrictive aperture, taken from [Bur04].

If the beam is cut on both sides at n_σ , we find

$$F_{L,2}(n_\sigma) = \int_{-\infty}^{\infty} dx' \left(\int_{n_\sigma\sigma_x+x_0}^{\infty} dx + \int_{-\infty}^{-n_\sigma\sigma_x+x_0} dx \right) G_2(x, x') = 1 - \text{erf}(n_\sigma). \quad (5.7)$$

5. Beam Losses at the LHC Collimator mounted in the SPS

These cases describe a single passage of a beam at a collimator. When we look at multi-turn passages, we find that the beam is evenly cut off at $n_\sigma = \sqrt{(x-x_0)^2/\sigma_x^2 + x'^2/\sigma_{x'}^2}$, see Fig. 5.12 b). The remaining particles are distributed according to

$$\begin{aligned} G_{\text{multiple}}(x) &= \int_{-\sigma_{x'}\sqrt{n_\sigma^2-(x-x_0)^2/\sigma_x^2}}^{\sigma_{x'}\sqrt{n_\sigma^2-(x-x_0)^2/\sigma_x^2}} G_2(x, x') dx' \\ &= \frac{e^{-(x-x_0)^2/2}}{\sqrt{2\pi}} \cdot \operatorname{erf}\left(\sqrt{\frac{n_\sigma^2 - (x-x_0)^2/\sigma_x^2}{2}}\right). \end{aligned} \quad (5.8)$$

Further, the fraction of particles remaining is given by

$$F_{R,\text{multiple}}(n_\sigma) = \int_{-n_\sigma\sigma_x+x_0}^{n_\sigma\sigma_x+x_0} dx \int_{-\sigma_{x'}\sqrt{n_\sigma^2-(x-x_0)^2/\sigma_x^2}}^{\sigma_{x'}\sqrt{n_\sigma^2-(x-x_0)^2/\sigma_x^2}} dx' G_2(x, x'). \quad (5.9)$$

This integral can be solved analytically in polar coordinates. We substitute $\frac{x-x_0}{\sigma_x} = r \cos \phi$, $\frac{x'}{\sigma_{x'}} = r \sin \phi$, and $dx dx' = r \sigma_x \sigma_{x'} dr d\phi$ to find:

$$F_{R,\text{multiple}}(n_\sigma) = \frac{1}{2\pi} \int_0^{2\pi} d\phi \int_0^{n_\sigma} r e^{-r^2/2} dr = 1 - e^{-n_\sigma^2/2}. \quad (5.10)$$

Thus, the fraction of particles lost after multiple passages at a collimator is given by

$$F_{L,\text{multiple}}(n_\sigma) = 1 - F_{R,\text{multiple}}(n_\sigma) = e^{-n_\sigma^2/2} \equiv e^{-\frac{1}{2}(r-x_0)^2/\sigma_x^2}, \quad (5.11)$$

where r is the position of the collimator.

Summarizing the above, one finds that moving a collimator jaw into a two-dimensional Gaussian beam phase-space distribution results in a curve of accumulated losses as a function of the collimator position which is Gaussian.

Results

Fig. 5.13 displays a curve of the lost beam fraction versus the collimator position, obtained by scraping with the right collimator jaw. The integrated loss curves can be well fit with a double Gaussian distribution of the form

$$G_2(x) = R_{\text{Fit}} \cdot e^{-(x-\mu_{\text{Fit}})^2/2\sigma_{\text{Fit},1}^2} + (1 - R_{\text{Fit}}) \cdot e^{-(x-\mu_{\text{Fit}})^2/2\sigma_{\text{Fit},2}^2}. \quad (5.12)$$

Its parameters, the mean value μ_{Fit} , standard deviations $\sigma_{\text{Fit},1}$, and $\sigma_{\text{Fit},2}$, and the ratio R_{Fit} , are determined by the fit. The error of each individual data point was estimated by fitting a linear function through 50 neighboring data points and determining their standard deviation with respect to the fit. As the curvature of the data points is not taken into account, a systematic error is introduced. The maximum deviation in terms of $\sigma_{\text{Fit},1}$, and $\sigma_{\text{Fit},2}$ introduced by this error is negligible compared to the variance of repeated measurements. Two exemplary fits for the error estimation of a single point are shown in Fig. 5.14.

For Session 1, the discrepancy of the horizontal beam size obtained from measurements with the wire scanner is about 28%. The agreement is reasonable considering that consequential measurements of the beam size vary, and that $\Delta\beta$ alone can introduce an uncertainty of

5. Beam Losses at the LHC Collimator mounted in the SPS

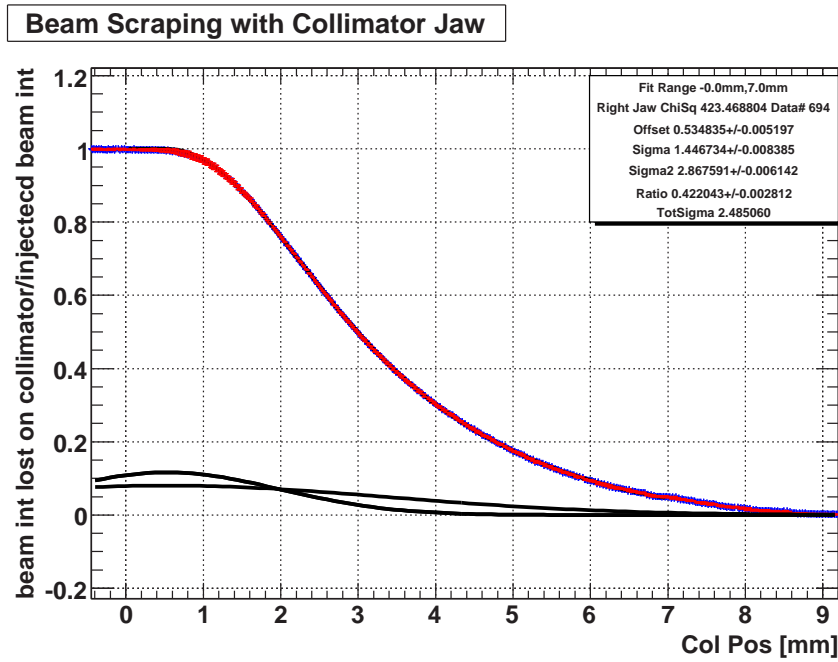


Fig. 5.13.: Fraction of lost beam intensity on the collimator versus the position of the collimator. The scraping of the beam was done with the right collimator jaw. Data points are displayed in blue (—), errors for the data points are displayed in red (—). The integrated losses were fit by a double Gaussian given in Eq. 5.12. The two normalized Gaussian distributions resulting from the fit are drawn in black (—). As the actual curve of the fit matches the data points precisely, it is not visible for this resolution.

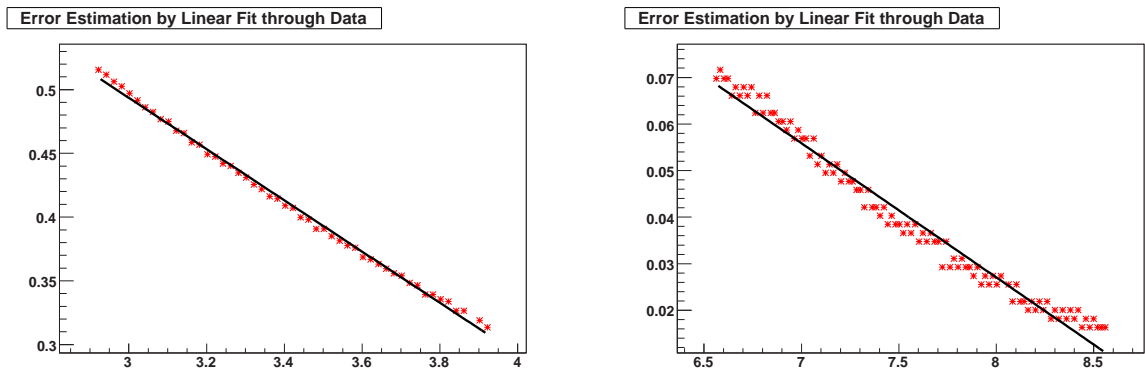


Fig. 5.14.: Magnified details of the measurements from Fig. 5.13 (same units). Estimation of the error of an individual point by a linear fit through 50 neighboring data points is shown for the slope region (left) and for the tail region (right).

5. Beam Losses at the LHC Collimator mounted in the SPS

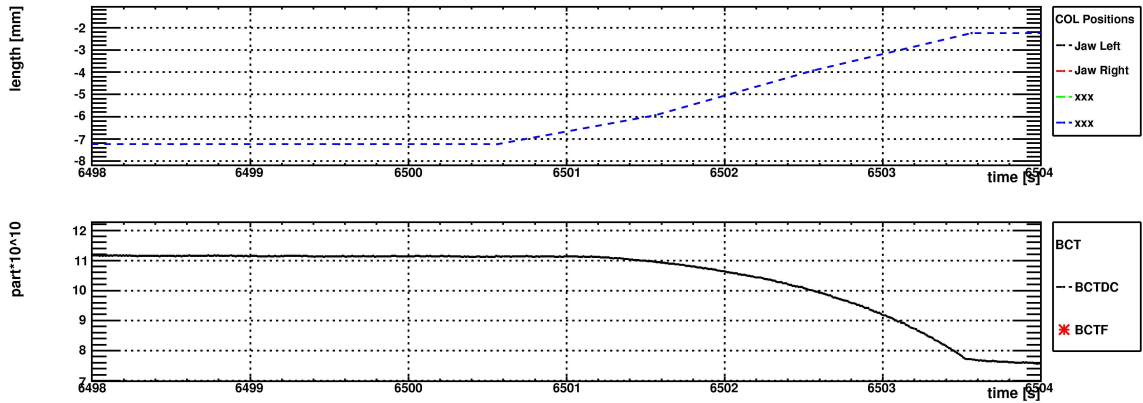


Fig. 5.15.: Collimator jaw position versus time, and beam intensity versus time. These measurements were used for matching the time offset between collimator data and BCT data.

Scraping No.	Mean [mm]	Standard deviation [mm]
R1	0.90	2.44
L1	-0.44	2.76
R2	0.53	2.49

Tab. 5.8.: Values obtained by fitting data from different scrapings (R1,R2,L1) with a double Gaussian. The unknown time offset between collimator position and BCT data has been varied for the R2 fit in order to estimate the accuracy of the determined fit parameters.

about 14%. As the BLM response depends only weakly on the beam size itself (errors of up to 11%, see Section 5.2.5), this inaccuracy is acceptable.

Uncertainties of the measurements include a time offset of up to ± 0.5 s between the beam current and the collimator position measurements [Wei07]. As the jaw moves with a velocity of 2 mm/s, this introduces an uncertainty of ± 1 mm for the mean value of the distribution and thus the position of the beam center with respect to the collimator. In Session 3 the time offset between the devices was calibrated. This was done by moving a collimator jaw only partly into the beam while it was circulating. The time offset of the decay of the beam current was matched to the end of the collimator movement⁹. Fig. 5.15 shows the collimator position versus time and the beam current versus time for such a match. This allowed to calibrate the time offset to about 0.1 s. The resulting uncertainty for the calibration of the impact parameter for the last session is thus 0.2 mm.

5.3.5. Calibration and Uncertainties of the Beam Impact Parameter

As the central beam orbit may shift, and the collimator jaw positions are initially not calibrated, a priori, only the relative position of the collimator jaws to each other is known. The distance between jaws and the center of the beam orbit has to be determined by measurements.

The beam position was measured in the previous section by *continuous scraping*. These

⁹The position of the collimator jaws is only measured every 0.5 s, but the slope of the constant collimator movement can be extrapolated to the rest position of the collimator.

5. Beam Losses at the LHC Collimator mounted in the SPS

measurements have the advantage that strong, initial beam oscillations already diminished at the time of the measurement. These coherent and slow (compared to the betatron frequency) beam oscillations are introduced by mismatches of the injection line optic parameters compared to the ring parameters. Consequently, their amplitude and initial phase, depends crucially on the injection settings which can vary for each measurement session. Beam offsets from these optic mismatches have to be taken into account when determining the beam position at the initial impact on the collimator. Fig. 5.16 shows coherent beam oscillations for Session 3. The initial amplitude of the oscillations is considerably reduced by a damping mechanism. Over time the remaining oscillations smear out as particles tend to populate the whole available phase space. There are remaining oscillations with lower amplitudes due to other effects discussed in Section 5.3.6. For Session 3, the initial amplitude at the place of the collimator is about 0.85 mm. As the phase of the oscillations is not precisely known at the collimator, this limits the accuracy of the impact parameter at injection to ± 0.85 mm.

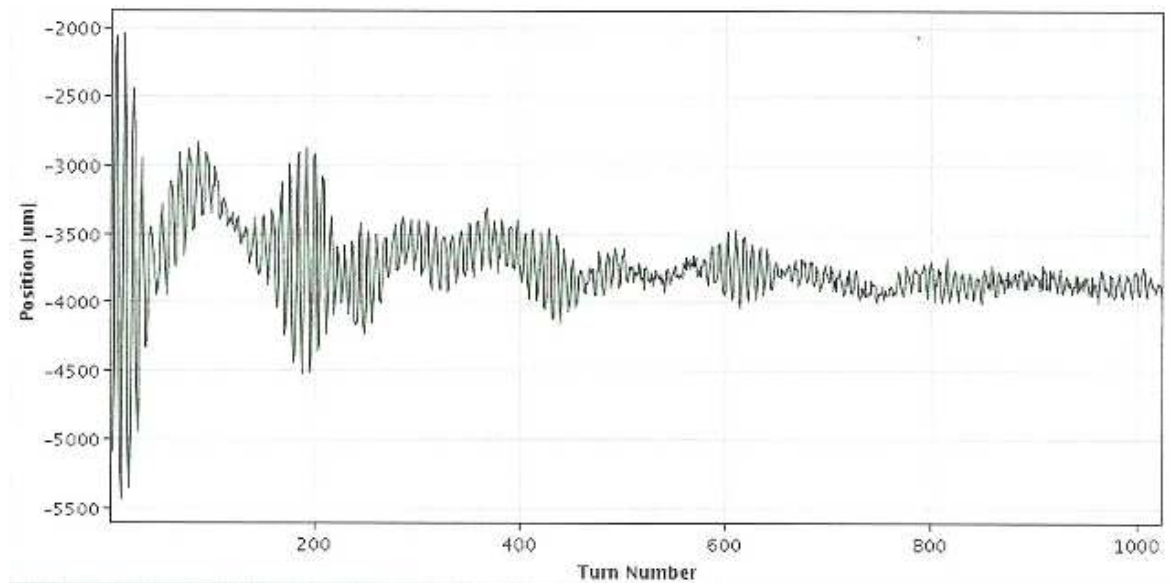


Fig. 5.16.: Oscillations of beam position in the SPS versus time for the first 1000 turns (about 23 ms) after injection.

For all three measurement sessions the calibration of the impact parameter was done by moving the collimator step wise into the beam until it was completely depleted. Due to the circular cut in the normalized phase-space, introduced through the collimator (see Section 5.3.4), the beam is completely depleted when the collimator reaches the center of the beam. As the collimator was moved into the beam in steps of 0.5 mm this is the constrain for the maximal exactness of this method¹⁰.

Results of the calibration of the jaw positions are listed in Tab. 5.7. The amplitude of the beam oscillations was monitored only during Session 3. It is not known for the first two sessions.

¹⁰An improvement in exactness can be achieved by fitting the curve of the beam intensity versus the collimator position, similar as in the previous section.

5.3.6. Impact Parameters for Continuous Scraping

During the *continuous scraping* procedure particles hit the surface of the collimator jaw as the collimator moves into the beam. For determining the depth of their impact various processes have to be considered.

- The movement of the collimator jaw slowly reduces the aperture.
- Diffusion processes of beam protons due to nonlinear fields or stochastic effects, like residual gas scattering, make the protons gradually migrate to larger betatron amplitudes.
- Coherent slow modulations of the center orbit lead to a relative motion of the maximum excursion of protons with respect to the collimator.

The combined effect of the collimator movement, diffusion, and coherent beam modulations is depicted in Fig. 5.17 a).

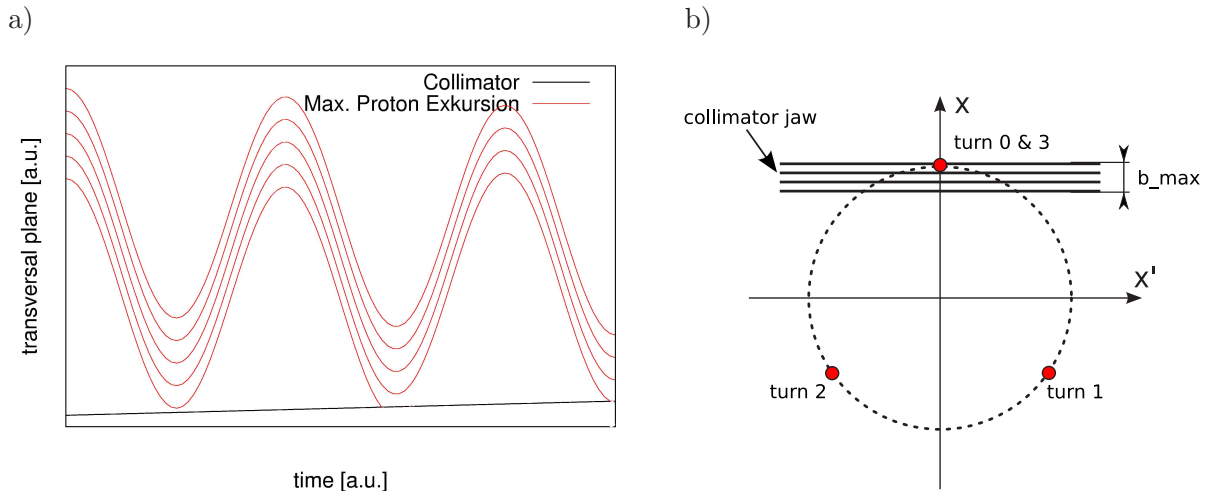


Fig. 5.17.: a) Transversal beam position at a collimator versus time. The combined effect of diffusion process, collimator movement, and coherent beam oscillations is sketched qualitatively. The collimator jaw moves slowly into the beam. The excursion of the particles is subject to coherent oscillations and increments due to diffusion ($\propto t^{1/2}$).

b) Phase-space position of a particle at a collimator is shown for four turns. Figure illustrates the calculation of the maximum impact parameter for a fractional tune of $1/3$. In turn 0 the particle misses the collimator jaw only slightly. In turn 3 it hits with a depth of $b_{\max} = 3 \cdot \Delta x$.

Impact Parameters due to Drift and Diffusion

The impact parameter distribution due to particle drift and diffusion can be well described analytically, see [Sei94]¹¹. It can be parameterized by a drift coefficient P_0 , which measures the linear amplitude increase per turn, and a diffusion coefficient D_0 . When assuming a

¹¹A detailed derivation of essential equations of the following formalism used in this work can be found in the same reference.

5. Beam Losses at the LHC Collimator mounted in the SPS

linear particle drift with a Gaussian distributed term due to diffusion, the emittance ϵ_k of a particle is given recursively for each turn k by

$$\epsilon_{k+1} = \epsilon_k \cdot \left(1 + P_0 + \sqrt{2D_0} \cdot \zeta_k \right) . \quad (5.13)$$

where ζ_k is a Gaussian distributed random variable with mean zero and unit variance. Such random variables can be obtained as described in App. C. The mean increase of the particle excursion per turn at the transversal point x , measured from the beam center, is therefore given by

$$\Delta x = \frac{P_0}{2} \cdot x . \quad (5.14)$$

The constant movement of the collimator jaw during the scraping process can be taken into account by this formalism by introducing an augmented drift coefficient $P_0(x_{\text{col}})$, depending on the velocity of the collimator v_{col} , its position x_{col} , and the accelerator revolution time τ :

$$P_0 \rightarrow P_0(x_{\text{col}}) := P_0 + \frac{2v_{\text{col}} \cdot \tau}{x_{\text{col}}} . \quad (5.15)$$

For betatron tunes away from low order resonances, the maximum impact parameter b_{max} on the collimator is nearly independent of the tune and can be approximated by

$$b_{\text{max}} \approx \frac{3}{2} \cdot x_{\text{col}} \cdot \left(\frac{\pi}{2} \cdot P_0(x_{\text{col}}) \right)^{\frac{2}{3}} , \quad (5.16)$$

when disregarding diffusion for a moment. Accelerators are generally operated away from those low order resonances. This was also the case for the measurements in the SPS. Tunes for the measurement sessions are listed in Tab. 5.4. For low order resonances the maximum impact parameter decreases considerably. For instance, for a fractional tune of $1/3$ the maximum impact parameter (again disregarding diffusion) is given by $b_{\text{max}} = 3 \cdot \Delta x$, as illustrated in Fig. 5.17 b).

The probability density function (PDF) of the impact parameter b due to drifting is calculated by summing all probabilities of possible combinations of particle phases and amplitudes which result in an impact parameter b . As a linear dependence of the probability is found [Sei94], it can be obtained by integrating over a δ -function in the following way:

$$P_{\text{dr}}(b) = C_{\text{dr}} \cdot \int_0^\infty u \cdot \delta(u - b_{\text{max}} + b) du , \quad (5.17)$$

C_{dr} is the normalization constant determined by $\int_0^\infty P_{\text{dr}}(b) db = 1$. The normalized integral evaluates to

$$P_{\text{dr}}(b) = \frac{2}{b_{\text{max}}^2} (b_{\text{max}} - b) . \quad (5.18)$$

If considering diffusive motion instead of a deterministic drift, the δ -function has to be replaced by Gaussian distribution. In this case the PDF is:

$$\begin{aligned} P_{\text{dr+di}}(b) &= C_{\text{dr+di}} \cdot \int_0^\infty u \cdot e^{-\frac{(u-b_{\text{max}}+b)^2}{2\sigma^2}} du \\ &= C_{\text{dr+di}} \cdot \left(\sigma^2 \cdot e^{-\frac{(b-b_{\text{max}})^2}{2\sigma^2}} + \sqrt{\frac{\pi}{2}} \sigma \cdot (b_{\text{max}} - b) \cdot \left(1 - \operatorname{erf} \left(\frac{b - b_{\text{max}}}{\sqrt{2}\sigma} \right) \right) \right) . \end{aligned} \quad (5.19)$$

5. Beam Losses at the LHC Collimator mounted in the SPS

with the error-function defined as

$$\operatorname{erf}(t) := \frac{2}{\sqrt{\pi}} \int_0^t e^{-x^2} dx, \quad (5.20)$$

and $C_{\text{dr+di}}$ is again a normalization constant, evaluating to

$$C_{\text{dr+di}} = 2 \cdot \left(\sqrt{\frac{\pi}{2}} \sigma \cdot (\sigma^2 + b_{\text{max}}^2) \cdot \left(1 + \operatorname{erf} \left(\frac{b_{\text{max}}}{\sqrt{2}\sigma} \right) \right) + \sigma^2 \cdot b_{\text{max}} \cdot e^{-\frac{b_{\text{max}}^2}{2\sigma^2}} \right)^{-1}. \quad (5.21)$$

By comparison with an empirical calculation, the dependence of σ on D_0 is found to be:

$$\sigma(D_0) = v \cdot x_{\text{col}} \cdot (D_0)^w, \quad (5.22)$$

with constants $v = 1.109$, and $w = 0.3 \pm 10^3 = 2/5$ [Sei94].

The mean impact parameter $\langle b \rangle$ can be obtained by integrating

$$\langle b \rangle = \int_0^\infty b \cdot P_{\text{dr+di}} db. \quad (5.23)$$

The integral evaluates to

$$\langle b \rangle = \frac{\sigma \sqrt{2\pi} \cdot s(s^2 + 3) \cdot e^{s^2/2} \cdot \operatorname{erf}(s) + s^2 + 2}{3 \sqrt{2\pi} \cdot s(s^2 + 1) \cdot e^{s^2/2} \cdot \operatorname{erf}(s) + s}, \quad (5.24)$$

$$\text{with } s := \frac{b_{\text{max}}}{\sigma} = 1.828 \cdot \frac{P_0^{2/3}}{D_0^{2/5}}, \quad (5.25)$$

where the last equal sign comes from Eq. 5.22.

To obtain the impact parameter distribution and the mean impact parameter for a *continuous scraping* process where the collimator jaw is moving, Eqs. 5.19 and 5.24 have to be integrated weighted by the transversal particle density function $\rho(x)$ while replacing P_0 as in Eq. 5.15:

$$P_{\text{cont}}(b) = \int_0^\infty 2 \cdot \rho(x) \cdot P_{\text{dr+di}}(b, x) dx, \quad (5.26)$$

$$\langle b \rangle_{\text{cont}} = \int_0^\infty 2 \cdot \rho(x) \cdot \langle b \rangle(x) dx. \quad (5.27)$$

The factor 2 origins from the simple fact that particles from both sides of the transversal plane are equally scraped away. A Gaussian particle distribution will be assumed in the following:

$$\rho(x) = \frac{1}{\sqrt{2\pi}\sigma} \cdot e^{-\frac{x^2}{2\sigma^2}}. \quad (5.28)$$

Influence of Coherent Oscillations on the Impact Parameter

Coherent beam oscillations additionally enlarge impact parameters as depicted in Fig. 5.17. Their amplitude must be large against the change of particle excursions due to the combined effects of drifting, diffusion, and collimator movement. Amongst others, slow oscillations can be due to

5. Beam Losses at the LHC Collimator mounted in the SPS

Parameter	
v_{col}	2 mm/s
τ^{SPS}	23.069 μs
D_0^{SPS}	$\sim 2 \cdot 10^{-10}$ a
$\Delta t^{\text{SPS}}/\tau^{\text{SPS}}$	7.69

a: This is a rough assumption.

Tab. 5.9.: Collimator and SPS parameters as relevant for the calculation of the impact parameters.

- betatron coupling (action exchange between the transversal planes modulates the maximum particle excursion),
- synchrotron oscillations, leading to oscillations of the reference orbit,
- and closed orbit oscillations, as caused by power supply ripple and ground motion.

These oscillations lead to a periodic relative motion of the maximum particle excursion with respect to the collimator jaw. Particles diffuse outwards between the maxima of an oscillation period Δt to hit the jaw then with deeper impact parameters at the end of this oscillation period. They feel, so-to-say, an effective drift process and the collimator movement after a time Δt . Assuming regular oscillations of one dominant frequency, the impact parameter can still be approximated for this situation by the Eqs. 5.19 and 5.24 by modifying P_0 and D_0 . The diffusion process scales with $t \propto t^{1/2}$. After a time Δt of unhampered diffusion the effective diffusion coefficient will be given by

$$D_0^{\text{eff}} = D_0 \cdot \sqrt{\frac{\Delta t}{\tau}}. \quad (5.29)$$

Similarly, the effective drift coefficient after a time Δt is given by

$$P_0^{\text{eff}} = P_0 \cdot \frac{\Delta t}{\tau}. \quad (5.30)$$

By replacing original coefficients with the effective ones, one can calculate $P_{\text{cont}}^{\text{eff}}(b)$ and $\langle b \rangle_{\text{cont}}^{\text{eff}}$.

Resulting Impact Parameter Distributions for Continuous Scraping

Eqs. 5.26 and 5.27 were evaluated by numeric integration as the integrals are quite complex. The numeric results of the PDF's were then fit for further analytic treatment by the tail of a Gaussian with the following parameterization:

$$P_{\text{cont}}^{\text{Fit}}(b) = A_{\text{Fit}} \cdot e^{-\frac{(b-\mu_{\text{Fit}})^2}{2\sigma_{\text{Fit}}^2}}. \quad (5.31)$$

Relevant parameters of the collimator and the SPS are listed in Tab. 5.9. Beam sizes are listed in Tab. 5.10. The drift term P_0 is small against the movement speed of the collimator for relevant amplitudes. Thus, drifting can be neglected and set to zero. Δt was set to the period of the eigenfrequency of the SPS for a horizontal SPS tune of 0.13. The tune invokes a dominant harmonic oscillation.

When evaluating Eqs. 5.26 and 5.27 with given parameters, with and without considering slow beam oscillations, one obtains mean impact parameters of a few microns, see Tab. 5.10, and the PDF's shown in Fig. 5.18.

5. Beam Losses at the LHC Collimator mounted in the SPS

Session	No. 1	No. 3	
No. of bunches	72	12	72
Hori. σ_x [mm]	1.81	4.96	3.23
$\langle b \rangle_{\text{cont}} [\mu\text{m}]$	1.45	2.04	1.76
$\langle b \rangle_{\text{cont}}^{\text{eff}} [\mu\text{m}]$	5.62	7.88	6.82

Tab. 5.10.: Mean impact parameters as obtained by Eq. 5.27 for drift and diffusive processes only $\langle b \rangle_{\text{cont}}$, and additionally including slow orbit oscillations $\langle b \rangle_{\text{cont}}^{\text{eff}}$.

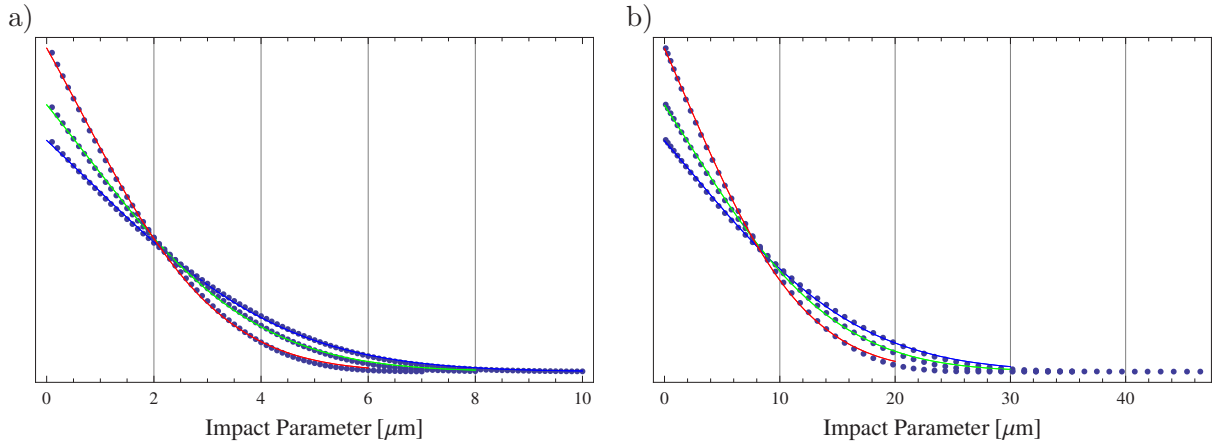


Fig. 5.18.: Normalized PDF's as obtained by Eq. 5.26. For drift and diffusive processes only (a), and additionally including slow orbit oscillations (b). Numeric data is fit by Eq. 5.31. Red, green, and blue curves correspond to Session 1, Session 3 with 72 bunches, and Session 3 with 12 bunches, respectively.

Discussion of Impact Parameter Distributions for Continuous Scraping

For a *continuous scraping* of the beam with a collimator jaw, impact parameters are essentially determined by coherent slow oscillations of the beam and the motion of the collimator. If there would be no coherent beam oscillations, maximum impact parameters on the collimator jaw would be by a factor of about 4 lower. The diffusion parameter D_0 is not precisely known, but for results including slow oscillations it plays a minor role. There are several superimposed coherent beam oscillations which are not completely regular. These fluctuations of the amplitudes can also lead to increased impact parameters on the jaw.

There are numerous approximations and assumptions made in the derivation of the impact distributions. There are also uncertainties in some parameters crucial for the calculation of the results. Hence, obtained numbers have to be considered as a rough estimation.

Mean impact parameters without considering beam oscillations are about 1.5 to 2.0 μm . Mean impact parameters of 16 μm are produced by multiples of the assumed oscillation period Δt or by multiples of the assumed diffusion parameter D_0 . Thus, a reasonable assumption for mean impact parameters be somewhere between 2 – 16 μm with a shape similar to the ones obtained in Fig. 5.18.

5.3.7. Normalized Detector Signal for Direct Dumping

In this type of measurement series the collimator was partially or completely moved into the beam orbit when the beam was injected, as shown in Fig. 5.9.

Number of Particles Lost on the Collimator

When “dumping” the beam directly after injection on the collimator, the number of injected protons is measured by the beam current transformers (BCT’s) in the injection transfer line. To determine the number of protons lost on the collimator jaw $N_{\text{ploc}}^{\text{dump}}$ from the beam current measurements, one has to account for protons that are injected, but not lost on the collimator itself, and thus, are not contributing to the signal seen by the BLM’s. These losses can be due to mismatches from the transfer line to the SPS, restrictive vertical aperture limits, and energy offsets of beam protons leading to their loss in high dispersion regions.

When the collimator jaws are withdrawn, the ratio R_{Lost} of the particles seen by the BCT in the SPS over the particles seen by the BCT in the transfer line was 0.975 and 0.996 for Session 1 and 2, respectively. For Session 3, the injected intensities were by two to three orders of magnitude lower compared to the previous sessions. For these low intensities the BCT’s in the transfer line showed a systematic offset compared to the more accurate measurements of the SPS BCT. This offset was corrected and resulted in a ratio R_{Lost} of 1.10. For direct “dumping” on the collimator, the number of *lost protons* on the collimator $N_{\text{ploc}}^{\text{dump}}$ was calculated by

$$N_{\text{ploc}}^{\text{dump}} = N_{\text{Prot. in Transfer Line}} \cdot R_{\text{Lost}} - N_{\text{Prot. in SPS}} \quad (5.32)$$

for each cycle.

The dose integrated by the BLM detectors during the injection is divided by the number of particles lost on the collimator $N_{\text{ploc}}^{\text{dump}}$ to obtain the normalized dose.

Saturation Effects for the IC

For measurements by *direct dumping* high doses are integrated in small time intervals. At high dose rates, like in Sessions 1 and 2, IC detectors are subject to space-charge effects. Space-charge effects start to affect linearity of the IC signal at rates of about 17 mGy per 40 μs . For Session 3, the beam intensity was reduced by 1 to 2 orders to minimize space-charge effects in the IC’s. Measurements are conducted in the onset of space charge¹².

Additionally, BLMCFC cards saturate for IC detectors for more than 0.88 mGy per 40 μs -integration interval (22 Gy/s) as explained in Section 4.3. Fig. 5.19 displays saturated signals of several IC’s. The electronic saturation of the BLM signals can be circumvented by placing a filter, consisting of a capacitor and a resistor, between IC signal cable and BLMCFC card. This results in a stretched-out BLM signal due to the resistor limited discharge of the capacitor. For Session 1 and 2, IC1A, and for Session 3, IC1B were equipped with such a filter.

Consequently, there is only usable IC data from the IC1B detector for Session 3.

¹²Signal for full impact on the jaw was for IC1B for 12 [72] bunches about 30 mGy [150 mGy].

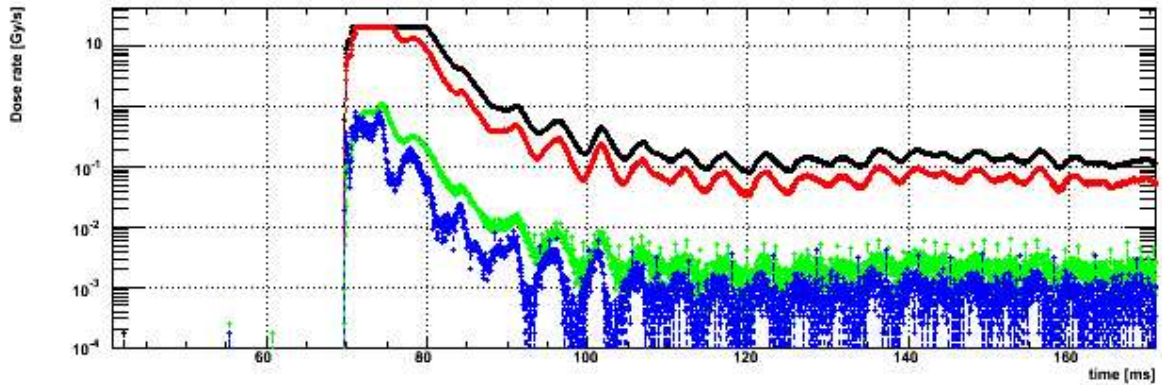


Fig. 5.19.: Dose rate measurements of four IC's downstream of the collimator versus time with a resolution of $40 \mu\text{s}$. The black and the red curve show saturation of the electronics at 22 Gy/s after initial impact of the beam. The signal oscillations are caused by beam movements due to the harmonics of the SPS magnet power converters [Kra08].

Uncertainties of the BLM Detector Signals

The sets of data, i.e. BLM measurements, collimator position, and beam current measurements, were taken with a systematic offset of timestamps. To correlate the data, the time offset between the different measurements had to be determined. As there is one BLM value every second, the offset between BLM data and BCT data can be determined up to one second. This results in some cases in an uncertainty determining the exact lost intensity in the integration time of the BLM data.

Due to the very low intensities of Session 3 the SEM signal-to-background¹³ ratio is small. Large background fluctuations were averaged and subtracted from the signal. Fluctuations of the remaining SEM signal are in the order of some percent. They were averaged by repeated measurements.

The background signal of the IC's has been evaluated to be at least three orders of magnitude smaller than the full signal and is hence negligible.

Results and Discussion of Measurements by Direct Dumping

Fig. 5.20 shows the normalized BLM signal versus particles lost on the collimator for Session 3 for the IC1B and the SEM detector. The curves of the IC detector show a clear dependency on the intensity of protons lost on the collimator. Values for small intensities are up to 50% higher. This can probably partly be attributed to space-charge effects. But also the curve from the SEM measurements with the left collimator jaw in the beam shows a slight dependency. Values are up to 20% higher for low intensities. Tab. 5.11 lists the signal-to-dose measurements. SEM measurements from Session 1 differ by 30% from the averaged SEM signal from Session 3. SEM (and also saturated IC's) measurements from Session 2 are systematically lower by about 60%. This systematic offset is not understood and these measurements were not considered for further data analysis.

An analysis of possible causes of the data dependency on the intensity was done.

¹³This background is due to a constant offset current of 10 pA added to the input current of the BLMCF card. This is done to constantly monitor the SEM's for proper functioning and to avoid negative currents.

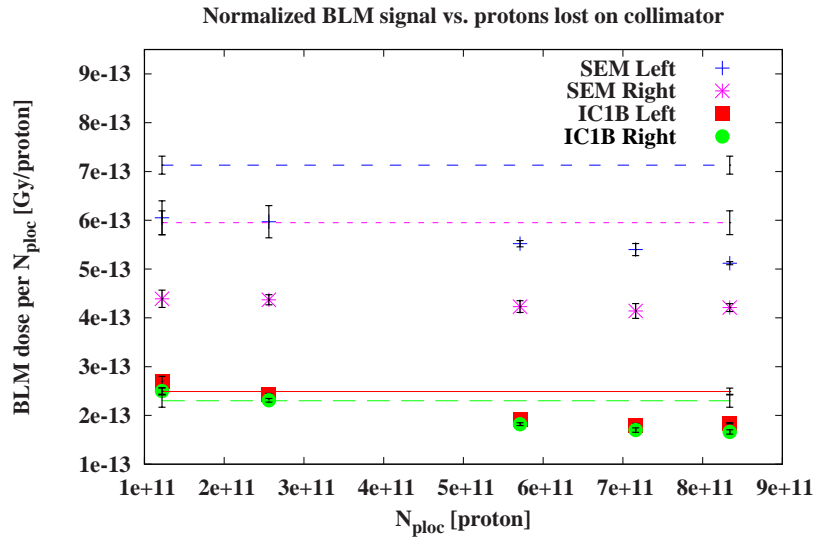


Fig. 5.20.: Normalized BLM signal of IC1B and SEM from Session 3 versus $N_{\text{ploc}}^{\text{dump}}$. For the values marked with “Left” [“Right”] the left [right] collimator jaw was at 3.25 mm [1.75 mm] past the center of the beam orbit. Points are measured values. Lines are values predicted by simulations.

- ★ The lowest SEM signal for left scraping was found to be due to a smaller collimator jaw gap for this measurement (decreased from 14 to 5 mm). In contrary to the IC’s, the SEM, which is mounted at the height of the beam, is sensitive to this gap-width. This reduces the spread of the SEM values to 12%.
- ★ The change of the BLM response due to different beam sizes for low and high intensities, i.e. 50% between 12 and 72 bunches (see Tab. 5.7), was simulated. It resulted only in maximum signal changes of 6%.
- ★ The sensitivity of the BLM signal to different impact parameters was investigated. Both simulation and measurements from Session 1 and 2 (see Tab. 5.11) show a low dependence of maximum 5% for different positions of the beam center with respect to the collimator of 0.0 and 5.5 mm.
- ★ A large jaw-beam angle misalignment of a few mrad produces a BLM response which is increasing with increasing beam size¹⁴ as more jaw matter is traversed. Such a big misalignment is not expected. The data of the stepping motors from the jaw agree within about 0.01 mm. Yet, the beam-jaw angle was not calibrated at the beginning of the measurements.

It is concluded that the dependency of the SEM measurements on the beam intensity is not fully understood.

5.3.8. Normalized Detector Signal for Continuous Scraping

In this measurement series the circulating beam was scraped by continuously moving a collimator jaw into the beam center as shown in Fig. 5.10. As the dose measured by the BLM

¹⁴For our measurements the beam size was larger for smaller intensities.

5. Beam Losses at the LHC Collimator mounted in the SPS

Session	No. 1		No. 2		No. 3	
Jaw	Left		Left		Left	Right
Pos. [mm]	0.0	5.5	0.0	5.5	3.25	1.75
Meas.	Normalized dose/ 10^{-13} [Gy/proton lost on collimator]					
IC1B	saturated		saturated		2.70 ± 0.10	2.50 ± 0.07
SEM	7.60 ± 0.12	7.32 ± 0.12	3.11 ± 0.02	2.98 ± 0.02	5.73 ± 0.17	4.27 ± 0.05
Sim.	Normalized dose/ 10^{-13} [Gy/proton lost on collimator]					
IC1B	-	-	-	-	2.49 ± 0.07	2.30 ± 0.13
SEM	10.2 ± 0.4	10.4 ± 0.3	10.2 ± 0.4	10.4 ± 0.3	7.13 ± 0.19	5.95 ± 0.24
Ratio	Measurement/Simulation					
IC1B	-	-	-	-	1.08	1.09
SEM	0.75	0.70	0.31	0.29	0.80	0.72

Tab. 5.11.: Normalized BLM signal of IC1B and SEM measured for *direct dumping* of the beam. SEM values from Session 3 are averaged over all intensities; except the lowest value from the left jaw (see Results and Discussion). For the IC values the data from the lowest intensity was chosen, as the signal change due to the space charge effect is the lowest. The row with the jaw position lists the jaw position past the center of the beam orbit.

detectors is accumulated over a scraping period of approximately 3s, saturation of the IC detectors does not play a role. The integrated losses over 5.2s were taken during the scraping period (RS10, see Tab. 4.2).

Number of Particles Lost on the Collimator

For measurements by *continuous scraping*, the injected particles are initially measured by the SPS BCT. The number of *lost protons* evaluates to

$$N_{\text{ploc}}^{\text{scrap}} = N_{\text{Prot. in SPS before scraping}} \cdot \quad (5.33)$$

Results and Discussion of Measurements by Continuous Scraping

Tab. 5.12 lists the doses measured by the BLM detectors per lost proton. *Continuous scrapings* were made for Session 1 and 3. In Session 1 there were only two scrapings performed for each collimator jaw. Thus, the reproducibility of these measurements is not precisely known and errors of the values are only indicative. For Session 3, there were nine scrapings performed with the left jaw and eleven with the right jaw for various intensities.

Measurements for Session 1 and 3 agree for the IC's within 15%, and for the SEM within 13%. The signal ratio between left and right scraping is slightly higher for Session 1. The difference between measurements might be due to a slight misalignment of the collimator jaws with respect to the beam together with a different mean impact parameter on the jaw (see Section 5.3.6).

5. Beam Losses at the LHC Collimator mounted in the SPS

Session	No. 1		No. 3		Ratio 1	Ratio 3
Jaw	Left	Right	Left	Right	Left/Right	
Meas.	Normalized dose/ 10^{-13} [Gy/proton lost on collimator]					
IC1A	3.08 ± 0.02	2.26 ± 0.12	2.64 ± 0.04	2.41 ± 0.02	1.36	1.09
IC1B	-	-	1.92 ± 0.03	1.95 ± 0.01	-	0.98
SEM	9.84 ± 0.30	8.35 ± 0.30	8.57 ± 0.43	7.65 ± 0.42	1.18	1.12
Sim.	Normalized dose/ 10^{-13} [Gy/proton lost on collimator]					
IC1A	3.19 ± 0.45	2.14 ± 0.30	3.33 ± 0.43	2.57 ± 0.38	1.49	1.30
IC1B	2.20 ± 0.31	1.57 ± 0.22	2.41 ± 0.35	1.62 ± 0.21	1.40	1.48
SEM	8.18 ± 1.22	5.10 ± 0.81	8.56 ± 1.19	4.40 ± 0.61	1.60	1.95
Ratio	Measurement/Simulation					
IC1A	0.97	1.06	0.79	0.94		
IC1B	-	-	0.80	1.20		
SEM	1.20	1.64	1.00	1.73		

Tab. 5.12.: Normalized BLM signal measured for *continuous scraping* of the beam by detector IC1A and SEM.

5.4. Evaluation of the Simulation

The simulation in FLUKA was adapted to the beam impact conditions and collimator jaw positions during the measurement sessions. Both measurement types for determining the normalized BLM signal, *direct dumping* and *continuous scraping*, were reproduced. Simulations were run with parallel beam particles at 26 GeV/c and a momentum spread $\Delta p/p$ of 0.001.

5.4.1. Simulation of Direct Dumping

A Gaussian beam distribution with the rms beam size and beam center with respect to the collimator as determined in Sections 5.3.3 and 5.3.5 was chosen. The collimator jaws were set according to the calibrated data from the collimator readout. The BLM signal increase due to *returning protons* was evaluated for these distributions to be $< 1\%$ (see Eq. 5.1). Tab. 5.11 lists normalized BLM signals resulting of these simulations and the ratio of measurement to prediction by simulation.

The response of the SEM was also calculated for selected beam impact scenarios by a two-step simulation in FLUKA and GEANT4. Particles in the FLUKA simulation which entered the region of the SEM were scored and used as a particle input map for GEANT4 simulations which model the physical processes in the SEM resulting in the signal. Simulations were done by D. Kramer [Kra08]. The resulting values are by about 30% higher than the values simulated by FLUKA only.

Comparison with Measurements and Discussion

Simulations of the IC chamber agree within 9% with the measured values. This agreement is reasonable. Yet, space-charge effects might have affected the measurement values. Considering space charge would result in a slightly increased signal from the measurements. The

measurements result in a SEM signal which is by 20-30% lower than the simulated response. With the combined simulation in FLUKA and GEANT values were even up to 40% lower. The deviation between the measured and the simulated signal may origin from:

- ★ uncertainties in the calibration of the response of the IC and the SEM (about 20% and 11%),
- ★ lower IC signal due to space-charge effects,
- ★ uncertainties of parameters for the simulation, i.e. mean impact parameter, beam size, misalignment,
- ★ and statistics of the simulation (about 5%).

5.4.2. Simulation of Continuous Scraping

The simulation of *continuous scraping* was done with following beam parameters. A Gaussian beam profile in the vertical (y) direction with rms beam size as determined in Section 5.3.3 was set. The jaw which was scraping the beam was set to the beam center. The fit of the horizontal impact distributions which was determined in Section 5.3.6 (see Eq. 5.31) was taken with respective parameters. Due to the small impact parameters there is a not negligible fraction of *returning protons* F_{ret} which leads to a BLM-signal increase of about 18% (see Eq. 5.1). Uncertainties of this estimation are assessed as described in Section 5.2.3 and are added to the uncertainty due to the statistics of the simulation. The results of the simulations are shown in Tab. 5.12.

Comparison with Measurements and Discussion

The signals of the IC's show an agreement within $\pm 21\%$. The measurements for the SEM differ by maximum -40% and $+73\%$ for FLUKA simulations. For combined simulations in FLUKA and GEANT4 the maximum deviation of the SEM signal is $\pm 40\%$

For scraping with the left and the right jaw the large measurement-simulation data offset of the SEM in opposite directions is not expected. Misplacement of the SEM in the simulation was investigated but no mistakes were found.

The measurements for *continuous scraping* yield bigger uncertainties in terms of initial parameters as input for the simulations compared to the measurements by *direct dumping*. To account for the uncertainties of the impact distributions, BLM signals for mean impact parameters of $2\ \mu\text{m}$ and $16\ \mu\text{m}$ were simulated. They resulted in a deviation of the detector signals of 10%.

As the impact on the jaw occurs with small impact parameters there is an increased sensitivity to the surface structure of the collimator, its flatness, and the jaw-beam angle. The effect of the jaw roughness was assessed by reducing the density of a $1\ \mu\text{m}$ -surface layer of the collimator jaws by a factor of 0.5. It resulted in a signal decrease of about 4%.

Misalignment of the beam-jaw angle is depicted in Fig. 5.21. It results in a decreased effective length of the collimator jaw for beam particles impinging with small enough impact parameters. A curvature of the jaw, measured by its flatness, has a similar effect. To assess the signal dependency on a beam-jaw angle misalignment as well as the jaw flatness, the jaw surface was inclined by an angle of $\pm 50\ \mu\text{rad}$. This reduced the response of the BLM detectors by maximum about 20%.

5. Beam Losses at the LHC Collimator mounted in the SPS

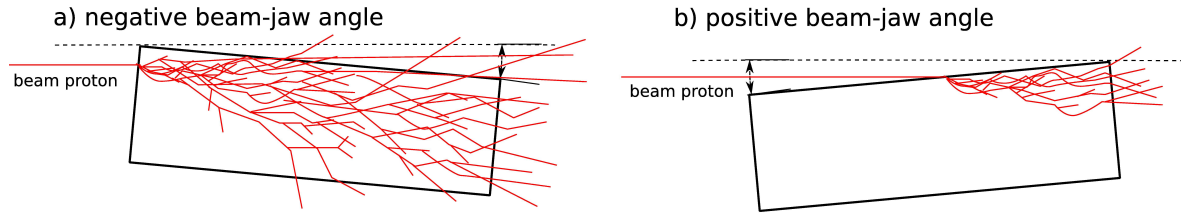


Fig. 5.21.: Misalignment of the beam-jaw angle is depicted schematically. Beam-jaw misalignment shortens the effective length of the collimator for impinging beam protons. For a positive misalignment beam particles hit the jaw later and less showers evolve in the jaw material.

Uncertainties for the measurements discussed above result mostly in a decreased detector signal and cannot explain the higher values from SEM measurements compared to simulations.

5.5. Comparing Measurements with Simulations – Results from the SPS Experiment

The response of the IC detectors could be reproduced by simulations within $\pm 21\%$. For the SEM detectors the agreement is worse. The two measurement methods, *direct dumping* and *continuous scraping*, resulted in opposite deviations from the simulated SEM signal. For simulations only with FLUKA the signal deviation was maximum $+73\%$ for *continuous scraping*, and -30% for *direct dumping*. For combined SEM simulations in FLUKA and GEANT4 the maximum deviation was about $\pm 40\%$.

The *direct dumping* procedure is simpler to reconstruct by simulation, as uncertainties of crucial parameters, such as the mean impact parameter and the impact distribution, influence the result of the simulation less. There is a variation of the SEM measurements of 12%, depending on the beam intensity, which is not understood.¹⁵ Further, values taken from Session 2 are systematically by a factor of about 0.4 lower, these values were not taken into account for further analysis. Space-charge effects influenced the signal of the IC's, making the data less reliable.

The measurements done with a *continuous scraping* of the beam do not show a dependency on the beam intensity. Repeated measurements for different intensities agree nicely with a statistical error of 1.3% [5.3%] for the IC [SEM]. The statistical error of the SEM measurements is mostly due to the noticeable background fluctuations on the low-range measurement scale of the SEM. Differences in signal between the two measurement sessions are probably due to different beam-collimator jaw angles together with slightly different mean impact parameters.

Measurements by *continuous scraping* are sensitive to not well known parameters from the experiment. These are the angular beam-jaw alignment, the surface structure of the collimator, and only slightly scattered beam particles which return and hit the collimator a second time. The fraction of these *returning particles* was estimated to be about 15%.

The *continuous scraping* process, for which beam particles continuously hit the collimator jaw with small impact parameters producing a constant BLM signal, is closer to the LHC collimation scenario for nominal operation. *Direct dumping* on the collimator is closer to an LHC failure scenario; many beam particles hit the collimator jaw with larger impact parameters in a short time scale.

When simulating the impact of a *pencil* beam on the collimator over the range from $0.1 \mu\text{m}$ to 2 mm, the BLM signal decreases for smaller impact parameters by about 60%. For a spread-out distribution of impact parameters, as it was the case for *direct dumping*, the BLM signal does not vary considerably (5%). This was confirmed by both measurements and simulations.

Beam-jaw alignment cannot be integrated in the BLM thresholds. Therefore it adds an additional uncertainty to the calibration of the BLM thresholds.

¹⁵For data see Fig. 5.20 without the measurement for the highest intensity of the “SEM Left”-data.

6. Simulations for the LHC Collimation Setup

At each collimator in the cleaning insertions a BLM pair, consisting of an IC and a SEM detector, is installed. Fig. 6.1 shows a schematic view of such a “collimator-detector cell”. This chapter describes energy deposition studies done for an LHC-like setup. Given the

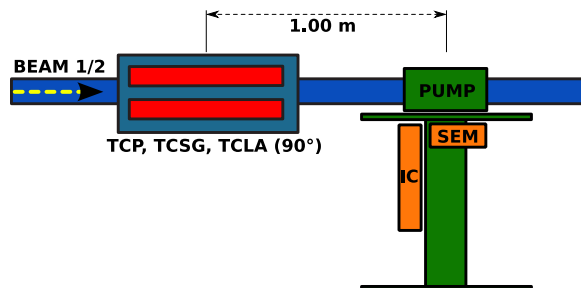


Fig. 6.1.: Schematic side view of a “collimator-detector cell” composed of a collimator, an IC, and a SEM, as installed in the LHC cleaning insertions IR3 and IR7. A vertical collimator with red jaws at 90° is shown.

collimator-specific damage levels, these simulations are intended to allow the prediction of BLM detector thresholds for protons in the LHC cleaning insertions IR3 and IR7, i.e. at the primary collimators (TCP), secondary collimators (TCSG), and active absorbers (TCLA). Thresholds for BLM detectors at other collimators positioned along the ring (not in IR3 or IR7) can be roughly estimated, based on obtained numbers. This study focuses on the dependency of the BLM detector signal on different parameters, such as detector misalignment, impact parameter, and beam-jaw angle.

Results from these simulations are compared to the ones obtained in the previous chapter and to studies done for the cleaning insertions by the FLUKA team [Mag06].

6.1. Shower Cross-talks

The term *shower cross-talk* refers to the signal seen by a BLM detector dedicated to the protection of a certain collimator which does not originate from this collimator itself, but from another collimator. This may include also signal from the other beam. Fig. 6.2 illustrates the cross-talk between two collimator-detector cells. Considering losses of the two counter-cycling beams at aperture limitations in the collimation region IR3 and IR7, preliminary assessments of *shower cross-talks* from different loss locations in the IR3 and IR7 cleaning insertions have been done, and are still ongoing [Kur03, Mag06, Bru08]. These simulations resulted in *shower cross-talk matrices* decomposing the total signal seen by a BLM detector into the fractional contribution to the signal from each loss location, i.e. collimators. This was done for nominal collimator settings.

6. Simulations for the LHC Collimation Setup

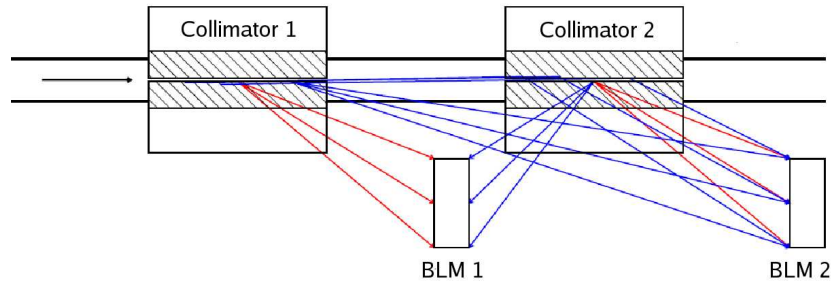


Fig. 6.2.: *Shower cross-talks* are illustrated schematically, adapted from I. Kourotchkin. Signal seen by BLM detectors, which is not originating from its dedicated device, here a collimator, is referred to as *shower cross-talk*. Lines in red mark showers from primaries lost and detected in the same “collimator-BLM detector cell”. Blue lines mark showers from primaries initially lost somewhere else. There is also a cross-talk between beam one and beam two, not shown in the picture.

6.2. Modeling Approach

In order to reduce complexity, simulations presented in this work assume that each IC and SEM detector pair installed at a collimator sees only signal originating from its collimator. For a cell, the BLM detector thresholds are set to limit the maximum energy deposition in the collimator for a determined ratio of detector signal to energy deposition in the collimator. *Shower cross-talks* from other sources, i.e. other collimators from Beam 1 or 2, leading to a possibly increased BLM signal by a background due to *shower cross-talk*, are not considered systematically. The focus of these simulations is on the dependencies of the normalized BLM signal and the ratio of BLM signal to energy deposition in the collimator on different parameters, such as the impact parameter on the collimator, the collimator surface roughness, and its surface alignment. The consequences of such dependencies to the calibration of the BLM thresholds are investigated.

6.3. Preparation of the Simulation

This section describes the implementation of a “collimator-detector cell” of the LHC collimation setup in FLUKA. The implementation orients itself on the geometric structure of the implementation of the LHC collimation insertions by the FLUKA team [Mag06]. As in the FLUKA simulation for the experimental setup in the SPS (see Chapter 5), the variation of the BLM signals due to misalignment and simplification is considered.

6.3.1. Implementation of Geometry and Materials

As in the SPS simulations discussed in the previous chapter, existing detailed models of the IC, the TCP, TCSG, and TCLA collimator were used¹. Collimators were implemented as interchangeable. As the angle of the collimators with respect to the beam axis changes for the different collimator-detector cells (tilted collimator positions: horizontal, vertical, skew), collimators are implemented to be rotatable in the simulation. Simulations were made in the following mostly for horizontal collimators. For a horizontal collimator the beam impacting on either side of the collimator leads to the same signal in the BLM detectors due to symmetry in

¹Kindly provided by the FLUKA team.

6. Simulations for the LHC Collimation Setup

the vertical plane. The full gap between the collimator jaws was set to 3.2 mm. The support of the collimator was not implemented. IC and SEM detector were modeled as in the SPS simulation. The support of the vacuum pump on which the BLM detectors are mounted was implemented in detail. The beam pipe was modeled as a cylinder. The structure of the pumps was disregarded as the pumps are located above the BLM detectors at the height of the beam and are thus expected to influence the BLM signal only slightly. Materials of the components and their properties were chosen following the design specifications. The position of the pump stand with respect to the collimators is precisely fixed for all collimator-detector cells. The positions of the BLM detectors on the pump stand itself can vary within 3 – 5 cm. Signal variations due to this misalignment are assessed later.

6.3.2. Recorded Quantities

Particle fluencies through the BLM detector volumes are recorded and energy deposition in the IC, the SEM, and the collimator jaws is scored and converted in the same way as in the SPS simulation, see Section 5.2.2 and App. F. Total and local energy deposition in the collimator jaws is scored to obtain a BLM signal-to-energy deposition ratio. The term “total energy deposition in the collimator jaws” refers in the following always to the energy deposition in the collimator jaw material plus the movable part on which they are mounted, i.e. support parts and cooling system. Local energy deposition in the jaws is recorded in a fine mesh to obtain the peak energy deposition in the collimator jaws. The binning size in direction of the beam (z) was set to 1 cm. The transversal binning size of the mesh varies and was chosen in accordance with the size of the impacting beam. It is at least by a factor of 5 smaller than the rms size of the impacting beam. Particles leaving the geometry through the beam pipe are scored and their properties are written in an extra file. This allows to use these recorded particles as input for simulations of collimator-detector cells placed further downstream.

6.3.3. Monte Carlo Statistics, FLUKA Physics Settings, and Biasing

The statistical error from the simulations was kept $\lesssim 5\%$ by adjusting the number of primary protons accordingly. FLUKA *production* and *transport thresholds* were varied between Setting Number 0 and 3, see Tab. 5.3. As no significant changes in detector signals were observed ($\leq 3\%$), thresholds were set to Setting Number 0. *Surface splitting* was used to augment the particle multiplicity in the collimator jaws and the BLM detectors in two steps by a total factor of ten.

6.3.4. Variation Studies

For the following variation studies it was assumed that a *pencil* beam with an impact parameter of $1\ \mu\text{m}$ hits the right jaw of a horizontally positioned primary collimator (TCP). The BLM signal change due to misalignment of the BLM detectors was investigated. To do so, the pump support with the BLM detectors was displaced by $\pm 3\text{ cm}$ in the transversal directions (x horizontal and y vertical) and by $\pm 5\text{ cm}$ in the longitudinal direction (z). The results are shown in Tab. 6.1. The BLM detectors are most sensitive to a displacement in height (y). Maximum changes for both LHC injection and top energy, are about 21%.

To assess the impact to the BLM signals of omitting the collimator support, a steel layer of the length of the collimator with a thickness of 5 and 10 cm was placed just beneath the

6. Simulations for the LHC Collimation Setup

Misalignment		Injection energy		Top energy	
Axis	Amount	IC	SEM	IC	SEM
x	-3 cm	4.2%	-6.9%	-2.6%	-6.1%
x	+3 cm	-3.3%	9.6%	-1.8%	1.0%
y	-3 cm	-21.5%	-15.7%	-11.3%	-12.9%
y	+3 cm	6.0%	13.8%	16.2%	20.8%
z	-5 cm	-6.7%	19.0%	-5.1%	3.2%
z	+5 cm	-13.7%	0.7%	0.6%	6.4%

Tab. 6.1.: Misalignment study displacing BLM detectors in transversal directions (x horizontal and y vertical) and longitudinal direction (z) for a horizontal TCP collimator. There are statistical fluctuations of about of $\lesssim 5\%$.

collimator. Simulations resulted in a variation of the BLM signals of up to 74%. As the influence of this approximation is big, a more realistic version of the collimator support was implemented; still simplified. Fig. 6.3 shows a side view of this model which looks like a “double cross”. For this support model, deviations of the BLM signal are maximum 16%. Tab. 6.2 summarizes results of the simulations.

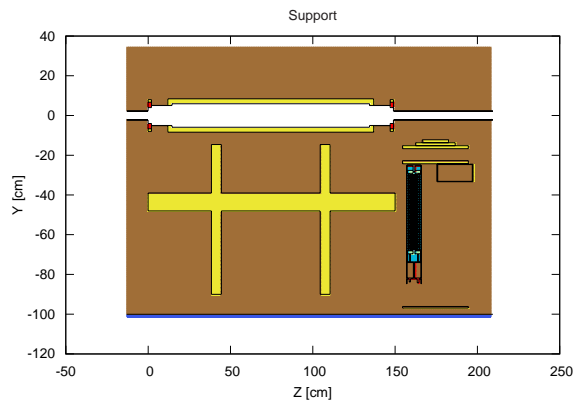


Fig. 6.3.: A side view of a collimator-detector cell is shown with a more realistic version of the collimator support (yellow “double cross” under the beam pipe).

6.3.5. Particle Spectra in the BLM Detectors

Fig.6.4 shows particle fluencies in the BLM detectors at 450 GeV and 7 TeV. The energy of these particles ranges up to about 10 GeV. Sharp cuts of the γ -spectrum at 0.33 MeV, of the e^\pm -spectra at 1.5 MeV, and of the p -spectrum at 10 MeV are due to the set *transport thresholds*, see Tab. 5.3, Setting Number 0. The response curves of the IC and the SEM detectors, see Fig. 4.3, show a sensitivity for γ 's down to about 1 MeV, for e^\pm 's to about 3 MeV, and for p 's to about 12 MeV. This justifies the chosen threshold settings. Except for

6. Simulations for the LHC Collimation Setup

Collimator support model	Injection energy		Top energy	
	IC	SEM	IC	SEM
Steel plane 5 cm	-59.8%	-12.4%	-56.1%	-20.6%
Steel plane 10 cm	-74.1%	-23.0%	-72.5%	-18.9%
Double cross	-4.7%	4.8%	-16.2%	-8.3%

Tab. 6.2.: Change of detector signal due to the introduction of a simplified collimator support in form of a steel block of 5 and 10 cm thickness, and a more realistic model having the shape of a double cross.

γ 's, the relative fluencies of particles at beam energies of 450 GeV and 7 TeV are very similar. γ 's exhibit a steeper incline for lower energies.

Doses deposited in the IC and the SEM, and thus their signals converted to normalized dose², are very similar. This is due to the similar position of the detectors in the geometry.

6.3.6. Comparison with the SPS Simulations and the IR7 Implementation

There are several observations when comparing fluencies through the BLM detectors of the SPS simulation at 26 GeV with the LHC collimation setup at 450 GeV and 7 TeV; see Fig. 5.8 and Fig. 6.4, respectively.

- ★ There are hardly any particles above 10 GeV.
- ★ The relative contribution of γ 's rises for the simulations with higher beam energy; especially for the low energy part of the spectra. This is due to a larger fraction of electromagnetic particles in high-energetic hadronic showers.
- ★ The relative contribution of high-energetic p 's and n 's (100 MeV – 1 GeV) increases.
- ★ p 's, e^\pm 's, and γ 's are estimated to yield the largest contribution to the detector signal for both setups. n 's and π 's add considerably.

It can be stated that the spectra from the simulations for the SPS experiment and the simulations for LHC collimation setup are comparable.

BLM signals per primary proton for the LHC collimation setup are roughly 1 to 2 orders of magnitude larger than the signals from the SPS setup. Besides the distinct beam energies for the different setups, this is also noticeably influenced by the difference in position of the detectors with respect to the collimator.

The BLM signals of this implementation of a collimator-detector cell were cross-checked with the BLM signals from the IR7 implementation by the FLUKA team [Mag06, Bru08]. Signals agreed within 5%.

6.4. Predictions of BLM Signals

This section contains predictions of the ratio of signal of the BLM detectors to protons on collimator N_{poc} , or normalized dose. The BLM signal is also related to the total and

²An air-filled SEM is assumed as mentioned before.

6. Simulations for the LHC Collimation Setup

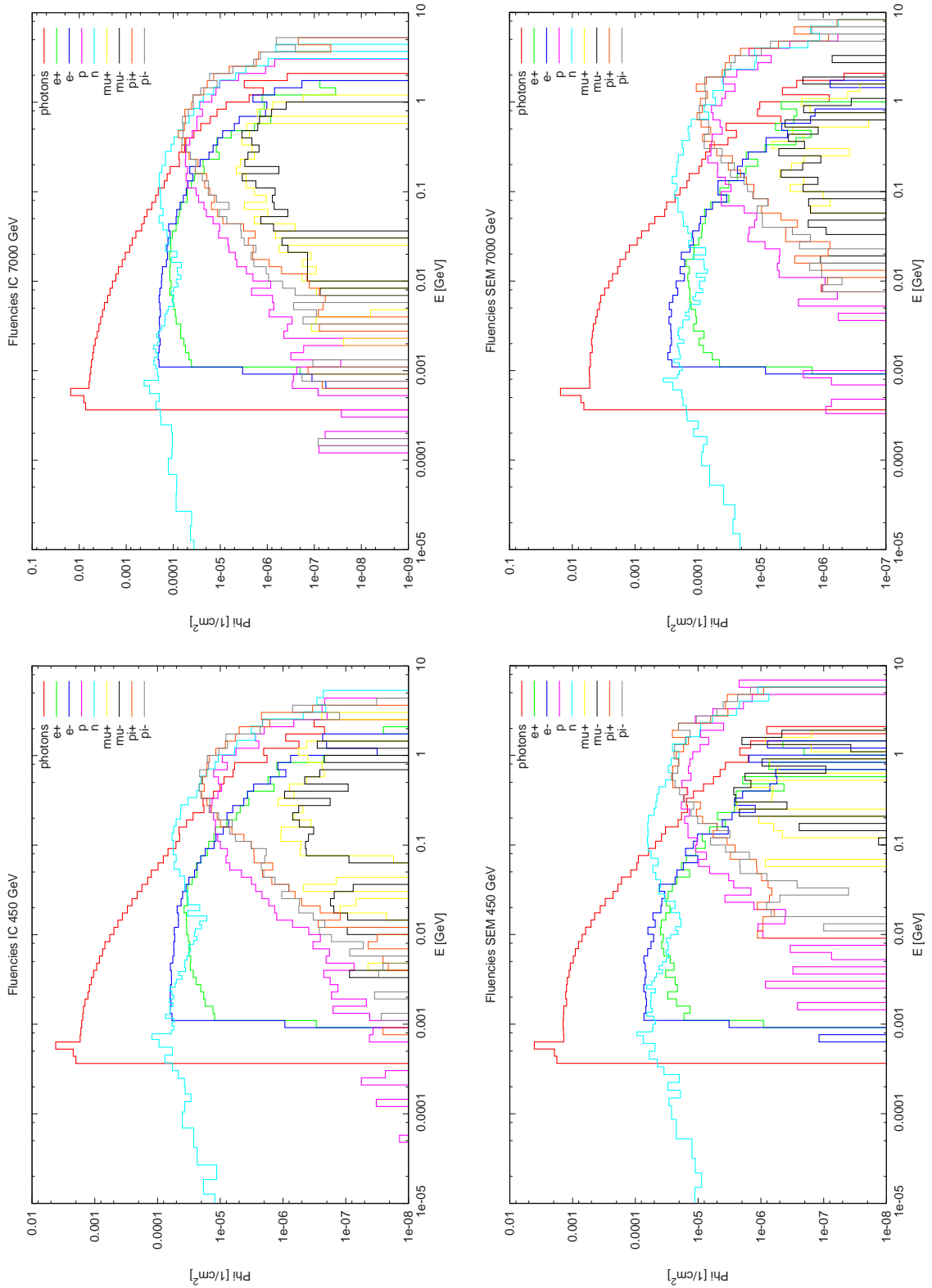


Fig. 6.4.: Track-length fluencies of different particles through the IC and the SEM detector versus energy. Fluencies are due to losses at a TCP collimator for the LHC collimation geometry at 450 GeV and 7 TeV. Fluencies are given per primary proton.

6. Simulations for the LHC Collimation Setup

Jaw with beam impact	Injection energy		Top energy	
	IC	SEM	IC	SEM
Up	-28.8%	-15.4%	-34.1%	-10.2%
Down	-29.8%	-18.5%	-36.1%	-8.9%

Tab. 6.3.: Dependency of the BLM signal on the position of the jaw were the beam is impacting, i.e. up, down, and left/right. The BLM signal for a beam impacting on the left or right jaw is the same due to a symmetric arrangement. Values are given as deviation in percentage from the BLM signal for a beam impacting on the left/right jaw of a horizontally mounted collimator. Simulations were done for a TCP collimator.

peak energy deposition in the collimator jaws. In Section 6.4.1 the normalized BLM signals are calculated for different collimator-detector cell geometries. Section 6.4.2 investigates the change in BLM signal due to different impact parameters on the collimator jaws, and different beam-jaw angles. Section 6.4.4 estimates the dose-to-peak energy deposition for beam distributions typical for different failure cases. In Section 6.4.5 the ratio of BLM signal to energy deposition is calculated for particle spectra of higher order halos impacting on TCP collimators.

6.4.1. BLM Signal Changes due to Different Cell Geometries

Collimator tilt angle Collimators in the LHC cleaning insertions are installed with horizontal, vertical, and skew collimator jaws, where skew collimators are typically inclined by 40° to 50° with respect to the horizontal plane. In Tab. 6.3 the signal for a beam impacting on the jaws of a vertically positioned collimator is given as a fraction of the signal for a beam impacting on a horizontally positioned collimator. Due to a symmetric arrangement, the BLM signals for a beam impacting on the left or right jaw are the same. SEM signals for a vertically mounted collimator deviate less than the IC signal as the SEM is positioned closer to the beam axis. Maximum deviation for the IC is -36%. Maximum deviation for the SEM is -19%. Simulations were done with a TCP collimator and a *pencil* beam with an impact parameter of $10\ \mu\text{m}$. Relative deviation for other collimators are expected to be similar.

Signals for skew collimators are expected to be somewhere in between those for the extreme horizontal and vertical positions. For further simulations a beam impacting on the right jaw of a horizontally positioned collimator was considered.

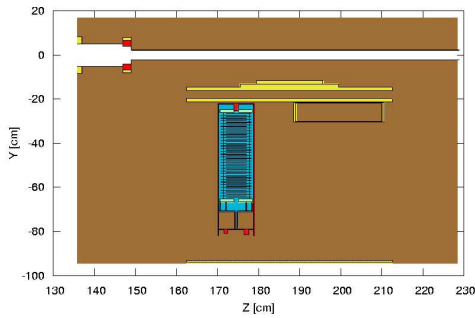
Swapped detector positions The pair of BLM detectors can be mounted on the pump support in two different ways, in a *normal* and a *swapped position*, as depicted in Fig. 6.5. The signal change due to these different positions was calculated. Tab. 6.4 shows the results of the simulations. Signals of the SEM chambers are by 132% higher for the *swapped position*. This large difference is due to the fact that the SEM is about 30 cm closer to the collimator for the *swapped position*. The signal of the IC differs by maximum 37%.

6.4.2. Scan of the Impact Parameter

Fig. 6.6 shows the normalized BLM signal versus impact parameter of a *pencil* beam at LHC injection and top energy for a TCP collimator. To assess the influence of the collimator jaw

6. Simulations for the LHC Collimation Setup

a)



b)

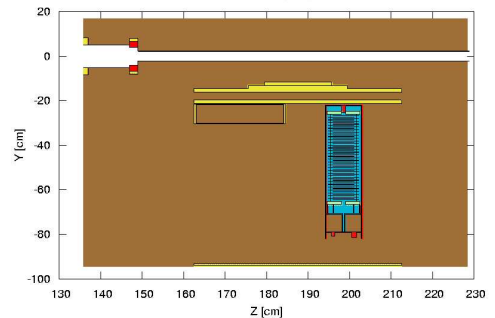


Fig. 6.5.: Side view of the *normal* (a) and *swapped position* (b) of IC and SEM as implemented in the simulations. The filling of the IC is light blue. The SEM appears as a rectangle filled with air (light brown). The vacuum of the beam pipe can be seen in white with the end of the collimator on the left-hand-side of the figure.

Beam energy	IC	SEM
Injection	-37.4%	131.6%
Top	-31.4%	95.8%

Tab. 6.4.: BLM signal for the *swapped position* for a horizontally mounted TCP. Given as deviation in percentage from the BLM signal for the *normal position*.

roughness for small impact parameters, the density of a $1 \mu\text{m}$ surface layer of the collimator jaw was reduced to $1/2$ of the regular density. The change in BLM signal for an impact parameter of $0.9 \mu\text{m}$ is -25% at 450 GeV and -31% at 7 TeV . Normalized signals of the IC and the SEM are nearly identical. For a TCP collimator, a steady increase of the BLM signal over the impact parameter range by about 100% (considering surface roughness about 200%) is predicted for both 450 GeV and 7 TeV .

When directing a beam on a collimator jaw with very small impact parameters, the Multiple Coulomb Scattering (MCS) formalism employed as default by FLUKA might not be adequate anymore. Close to surfaces ($\sim 1 \mu\text{m}$) the *step size* for calculating a MCS scattering angle³ can be large compared to the scattering angle. Particles are scattered out of the collimator jaw by a large MCS step which supposes the particle to be within the same material for the whole step length. This results in a modified angular spectrum of particles exiting the collimator jaw. To assess the impact of this effect to the BLM signals, simulations using single Coulomb scattering were compared to the simulations with the MCS formalism for an impact parameter of $0.9 \mu\text{m}$. The difference was 3% for the IC and 9% for the SEM.

Fig. 6.7 shows for a *pencil* beam the BLM signal per total energy deposition in the collimator jaws for the TCP, and the TCSG collimator as a function of the impact parameter. This ratio is about constant, and does not differ noticeably for LHC injection and top energy. For

³The *step size* is derived by a FLUKA-internal algorithm.

6. Simulations for the LHC Collimation Setup

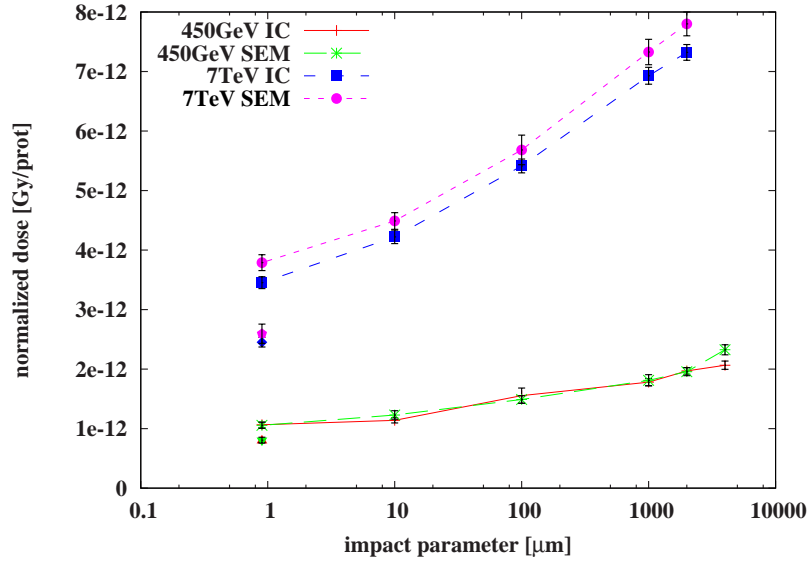


Fig. 6.6.: Normalized BLM signal versus impact parameter is shown for a horizontal TCP collimator. The isolated points are calculated reducing carbon density in a $1\ \mu\text{m}$ surface layer of the collimator jaws to $1/2$ of the regular density to cope for the surface roughness of the jaws.

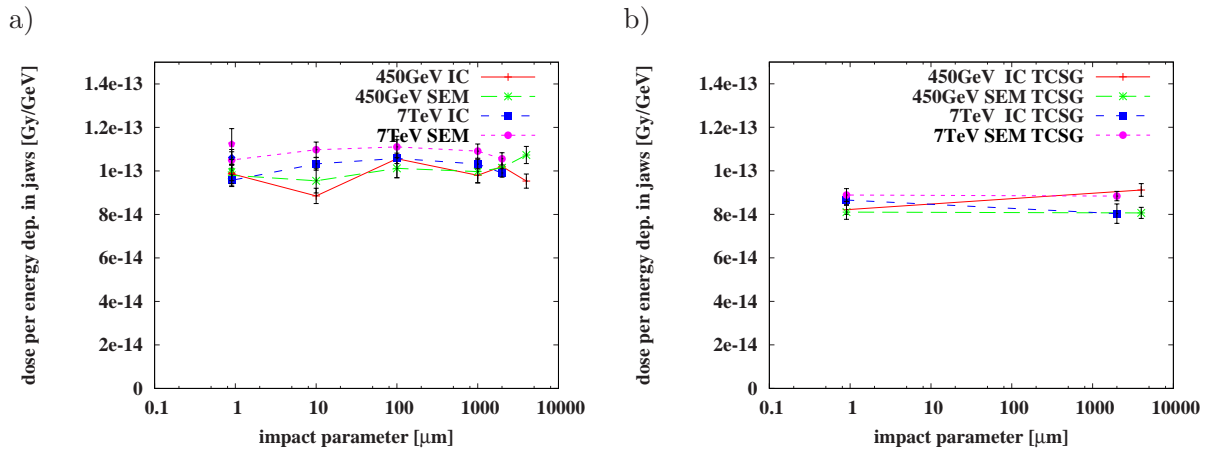


Fig. 6.7.: BLM signal-to-energy deposition ratio as a function of the impact parameter for a horizontal TCP (a) and a TCSG (b) collimator. The isolated points of the graph of the TCP collimator are calculated reducing carbon density in a $1\ \mu\text{m}$ surface layer of the collimator jaws to $1/2$ of the regular density to cope for the surface roughness of the jaws (the points are not clearly distinguishable as they fall together with the other ones).

6. Simulations for the LHC Collimation Setup

TCSG collimators, the ratios are shifted by a factor of about 0.76 compared to the ratios for the TCP collimator.

Fig. 6.8 depicts the signal-to-energy deposition ratios for a TCLA collimator. They are about one order of magnitude lower compared to the TCP and TCSG collimator due to the different jaw material (W). Over the data range of the simulations, the ratios show a maximum increase for smaller impact parameters of 50%.

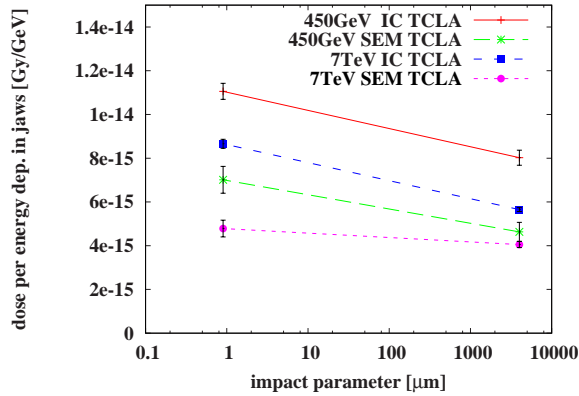


Fig. 6.8.: BLM signal-to-energy deposition ratio as a function of the impact parameter for a horizontal TCLA collimator.

6.4.3. Scan of the Beam-Jaw Angle

Alignment of the beam-jaw angle is a parameter which might differ according to collimator settings. For a beam-jaw angle not equal to zero, beam particles impacting close enough to the collimator surface see a shorter effective collimator length, see Fig. 5.21. A collimator can also have a shorter effective length for small impact parameters due to its jaw flatness, see Fig. 1.6. The reduction in effective length due to the jaw flatness is similar to the reduction due to a beam-jaw angle. Thus, its impact on the BLM signal can be also assessed by introducing a beam-jaw angle. Fig. 6.9 shows the BLM-signal ratios versus beam-jaw angle for a TCP collimator. A *pencil* beam with an impact parameter of $2 \mu\text{m}$ was used. Beam-jaw angles were varied between $\pm 300 \mu\text{rad}$. Negative and positive beam-jaw angles are defined as depicted in Fig. 5.21.

The normalized dose was found to vary about 2 to 3 orders of magnitude for both LHC injection and top energy. The ratio of BLM signal to total energy deposition in the jaws is nearly constant for negative angles and rises by a factor of about 2.5 [4.0] for IC's [SEM's]. This rise in signal ratio is due to two effects. Firstly, showers evolve only in the jaw-end of the collimator, thus there is no energy deposition in the upstream part of the collimator jaw. Secondly, the showers created in the jaw-end can propagate freely in direction of the detectors, unshielded by further jaw material. As SEM detectors are positioned closer to the beam axis, they are more exposed to the unshielded showers and the increase of their ratio is stronger compared to the increase of the ratios of the IC detectors.

6. Simulations for the LHC Collimation Setup

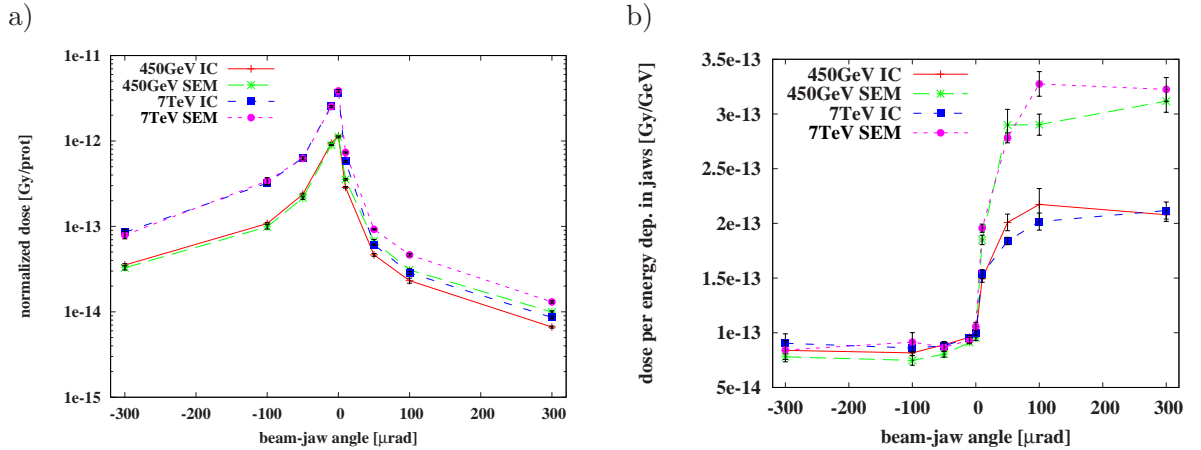


Fig. 6.9.: a) Normalized BLM signal is plotted for a TCP collimator versus beam-jaw angle between $\pm 300 \mu\text{rad}$.

b) Ratio of BLM signal to total energy deposition in the jaws is plotted for a TCP collimator versus beam-jaw angle.

6.4.4. Peak Energy Deposition

To estimate the ratio of BLM signal to peak energy deposition in the collimator jaws for failure cases, realistic impact parameter distributions on the collimator were assumed. Beam distributions on collimators for failures cases were calculated in [Alo06a, Alo06b]. They have the shape of a Gaussian tail for the horizontal impact depth, as the ones calculated in Section 5.3.6, Eq. 5.31. Mean impact parameters for those distributions range typically from $26 \mu\text{m}$ to $788 \mu\text{m}$. Further, it is found that they have an almost constant ratio of Gaussian parameters μ and σ which is about 1.0 [Alo08]. In the vertical direction a Gaussian with $\sigma_{\text{inj}} = 590 \mu\text{m}$ and $\sigma_{\text{nom}} = 160 \mu\text{m}$ was assumed for 450 GeV and 7 TeV, respectively. These are typical beam sizes at the collimators. Fig. 6.10 a) displays the peak energy deposition per proton on collimator N_{poc} as a function of the mean impact parameter. The peak energy deposition for a 450 GeV-beam [7 TeV-beam] decreases over the plot range by a factor of about 7 [4].

Fig. 6.10 b) shows the BLM signal-to-peak energy deposition ratio as a function of the mean impact parameter. This ratio increases over the range of the mean impact parameter for a 450 GeV-beam [7 TeV-beam] by a factor of about 10 [6] for both IC and SEM. The BLM signal-to-peak energy deposition ratio for a TCLA collimator is roughly about 25 [168] times higher for LHC injection [top] energy.

6.4.5. Secondary and Higher Order Particle Halos

Beam protons first impact on a primary collimator initiating hadronic showers. These showers and remaining beam protons then impinge on collimators and beam apertures further downstream. To estimate the BLM signal-to-energy deposition ratio of these *shower crosstalks*, the particle spectra leaving the simulated collimator-detector cells through the beam pipe were recorded and then propagated to the next cell. This was done with three horizontal collimators with a distance of 2 m (measured from the middle). A 7 TeV *pencil* proton beam

6. Simulations for the LHC Collimation Setup

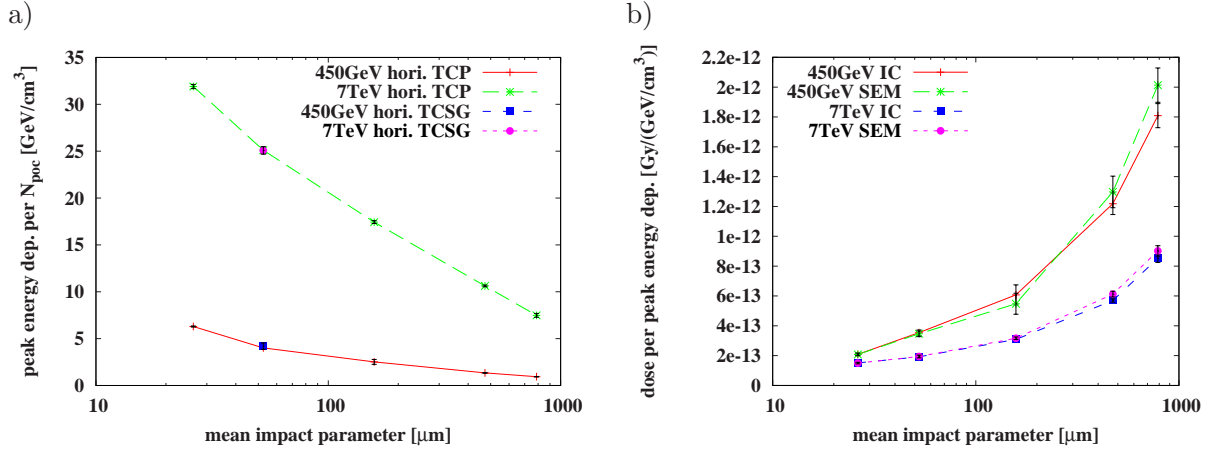


Fig. 6.10.: a) Peak energy deposition per proton on collimator N_{poc} as a function of the mean impact parameter is shown for a horizontal TCP and a horizontal TCSG collimator. b) BLM signal-to-peak energy deposition ratio as a function of the mean impact parameter for a horizontal TCP collimator.

Ratio	TCP 2	TCP 3
IC signal per energy dep. in jaws	-49.8%	-66.7%
SEM signal per energy dep. in jaws	-58.8%	-75.1%
Energy dep. in jaws per primary proton	378%	743%

Tab. 6.5.: Ratios of BLM signal per energy deposition in the collimator jaws, and energy deposition per proton on the first collimator (TCP 1) for LHC top energy. All values given as deviation in percentage from the ratios for the first collimator-detector cell (TCP 1, see Fig. 6.7 a)).

with an impact parameter of 1 μ m was directed on the first TCP and consequential spectra were then propagated through the next cells. Simulations done with particles which origin from collisions with collimators upstream underestimate the signals of the BLM's and result therefore in lower ratios of BLM response to energy deposition in the jaws. This is due to the fact that only particles inside the beam tube are propagated to the next collimator-detector cell. Particles leaving the previous simulation geometry outside the beam tube are neglected⁴. These particles would increase the response of the BLM detectors while only slightly augmenting the energy deposition in the collimator. Tab. 6.5 shows resulting BLM signal-to-energy deposition ratios for the collimators for a 7 TeV-beam. These ratios are smaller for higher order halos. At the same time energy deposition in the collimators is mostly due to higher order halos.

⁴Simulating those particles properly would require an implementation of the entire cleaning insertions. This is beyond the scope of this project. As mentioned before, simulations for the entire cleaning insertion are done by the FLUKA team

6.5. Results

The ratio of BLM signal to protons on collimator N_{poc} , or normalized BLM signal, and the ratio of BLM signal to total and peak energy deposition in the collimator jaws were investigated.

BLM signals of the IC and SEM detectors were found to differ by up to 132% for the two different positions, *normal* and *swapped position*, in which they are installed in the cleaning insertions. Misalignment studies of the BLM detectors, and an assessment of the impact on the BLM signals of omitting the geometry of the collimator support showed a maximum signal deviation of 22%.

The normalized BLM signal depends on the impact parameter of the protons (about 100% over the range from $1\ \mu\text{m}$ to $2\ \text{mm}$ for a TCP at 450 GeV and 7 TeV beam energy). On the contrary, the BLM signal divided by the total energy deposition in the collimator jaws remains for the graphite collimators, TCP and TCSG, almost constant; even for different beam energies. For the TCLA collimator (tungsten jaws) this ratio decreases over the simulated impact parameters by about 30% for larger impact parameters.

For a primary collimator and different beam-collimator jaw angles between $\pm 300\ \mu\text{rad}$, the normalized BLM signal varied for both LHC injection and top energies over approximately 2 to 3 orders of magnitude. The BLM signal divided by the total energy deposition in the collimator jaws increased for the same beam-jaw angles maximum by a factor of 4.

The ratio of BLM signal to total energy deposition is relevant to set BLM threshold values for damage prevention to the collimators for steady-state losses.

Peak energy deposition in the collimator jaws was predicted for LHC failure cases and related to the BLM signals. Corresponding ratios varied for the range of mean impact distributions for typical failure cases by a factor of about 10 [6] for 450 GeV [7 TeV]. These values are relevant for intense short-term losses.

For TCP collimators, the ratios of BLM signal to energy deposition from second and third order halos are lower by a factor of up to 4. The energy deposition in the collimator jaws is at the same time mostly due to these higher order halos.

6.5.1. Example of a BLM Threshold Value Calculation

Tab. 6.6 presents an example for a calculation of BLM thresholds for the vertically mounted primary collimators in the LHC cleaning insertions for steady-state losses. The calculation does not assume a safety margin⁵ and is done for BLM detectors mounted in the *normal position*. A minimal signal-to-energy deposition ratio is assumed for the TCP collimator, taking the lowest ratio of $0.85 \cdot 10^{-13}\ \text{Gy/GeV}$, and $0.95 \cdot 10^{-13}\ \text{Gy/GeV}$ for injection and top energy, respectively (see Fig. 6.7). The tilt of the collimator is taken into account (see Tab. 6.3). Values in the table are expressed in Joule. BLM threshold values in Gy/s have to be renormalized to the integration time of the corresponding running sum.

A more sophisticated calculation of BLM thresholds should take several arguments into account.

- ★ There is a delay of three to four turns between the detection of an increased radiation level and a safe beam extraction (see Section 1.2.2). Dangerous radiation levels for short time scales can be anticipated by including typical rates of loss increases due to failures,

⁵For instance, for the calibration of the BLM detector signals from Chapter 5. There is a safety margin assumed in the damage limits of the collimators.

6. Simulations for the LHC Collimation Setup

Beam energy	Damage limit	BLM signal-to-ED ratio		BLM threshold	
	TCP	IC	SEM	IC	SEM
GeV	kW in collimator jaws	Gy/J in collimator jaws		Gy/s	
450	87	$3.7 \cdot 10^{-4}$	$4.3 \cdot 10^{-4}$	32	37
7000	90	$3.8 \cdot 10^{-4}$	$5.3 \cdot 10^{-4}$	34	48

Tab. 6.6.: Example of BLM threshold values for steady-state losses at a vertically mounted TCP collimator. Values are calculated by multiplying the collimator damage limit with the BLM signal-to-energy deposition (ED) ratio. Damage limits for the collimator are taken from [Ass08].

see [Alo08]. BLM threshold values for short running sums (RS's) can be adequately rescaled. For instance, a damage limit for a component is given by a maximum dose D_{lim} in Gy in a time interval of 0.64 ms. This damage limit can be monitored by a shorter RS of 0.32 ms by assuming a certain, for example exponential growth rate, and initiating a safe extraction already when the rescaled BLM threshold for the 0.32 ms-interval is exceeded.

- ★ For fast losses, the “background” from slower losses might have to be taken into account. I.e., at the moment of an abnormally increased loss rate an LHC component has usually experienced prior radiation. This additional heat load might be significantly high, and thus, should be considered in the BLM threshold calculations. A simple approach would be to subtract dose rates from nominal steady-state losses, from shorter running sums.
- ★ Space-charge effects can be taken into account for the IC detectors. This allows to extend the valid range of loss rates for the IC detectors by rescaling thresholds adequately.

Conclusions

An experimental setup with an LHC secondary collimator (TCSG), two ionization chambers (IC's), and a secondary emission monitor (SEM) has been installed in the SPS. In the first part of this thesis beam losses measured by the LHC Beam Loss Monitoring (BLM) system at the collimator were compared to simulations in FLUKA. Additional simulations with only the geometry of the SEM detector were done (by D. Kramer) with GEANT4 to calculate the response of the SEM detectors more accurately. The geometry of the experimental setup was introduced in FLUKA to model the energy deposition in the BLM detector volumes. The ratio of BLM signal (in dose) to protons lost on collimator was calculated by simulations for the measurement conditions. Simulated and measured values agree for the IC's within $\pm 21\%$ and for the SEM within $\pm 40\%$ [73%] for FLUKA+GEANT4 [only FLUKA].

The SEM measurements showed a slight dependence on the intensity of 12% which is not understood. Measurements of the IC signals were partly in the regime of space-charge saturation of the IC detectors. Therefore only a few measurements were usable for a comparison with simulations.

Several parameters have a crucial impact on the results of the simulations. The influence of not precisely known model parameters on the BLM detector signals was assessed by variation studies. Varied parameters are:

- ★ the detail of the geometry (maximum change 15%),
- ★ FLUKA-internal particle threshold settings (no significant change),
- ★ misalignment (no significant change),
- ★ number of particles recycling after the initial passage at the collimator,
- ★ and different beam impact scenarios (maximum change 20% for beam-jaw angle).

The discrepancy of BLM signals between simulations and measurements and the BLM-signal variations for not precisely known parameters of the measurements are interpreted as a systematic uncertainty for determining BLM measurements at the collimators by simulations.

Below some suggestions are made to improve measurements and simulations and allow for a more precise comparison of measurements with simulations.

- ★ The beam-jaw angle should be accurately calibrated before the measurement session.
- ★ Simulations predict a large variation of the BLM signals for different beam-jaw angles. These predictions could be compared with measurements.
- ★ The fraction of beam protons returning after an initial passage at the collimator was approximated. An optical particle tracking program should be used to get a more accurate estimate, especially for settings with small impact parameters.

Conclusions

- ★ Measurements with lower beam intensities should be done, avoiding space-charge effects in the IC's.
- ★ A formalism for a space-charge correction of the IC signals considering the time structure of losses should be applied in the regime of space-charge effects.
- ★ Data acquisition devices should not have a time offset with respect to each other.

In the second part of this thesis BLM signals per impacting proton on collimator were predicted for the LHC collimation setup (at TCP, TCSG, and TCLA collimators) and related to the energy deposition in the collimator jaws. Particle spectra in the BLM detectors were found to be comparable to the ones from the experimental SPS setup. A comparison of BLM signals from simulations of this work with the IR7 simulation by the FLUKA team [Mag06] showed an agreement within 5%.

IC and SEM detectors may be installed in two different positions in the LHC cleaning insertions. The SEM detectors are very sensitive to the distance from the collimator in which they are installed. A shift of 30 cm between the two positions results in a SEM-signal increase of up to 132%. For IC detectors, which are installed further away from the beam axis, the change in signal between the two positions is smaller, at most about 37%.

Studies for different impact parameters were done. For a primary collimator (TCP) the signal increases for larger impact parameters by a factor of about 2 for both 450 GeV and 7 TeV. The ratio of BLM signal to energy deposition in the collimator jaws was found to be virtually constant for TCP and TCSG collimators for impact parameters between $0.9 \mu\text{m}$ and 2 mm for both LHC injection and top energy. For TCLA collimators the ratio increases over the simulated range for smaller impact parameters by maximum 50%.

Simulations with different beam-jaw angles showed a strong dependency of the BLM signal on the angle. This is due to the reduction of effective length of the collimator seen by impacting protons. For a TCP collimator inclined by maximum $\pm 300 \mu\text{rad}$ the BLM signals decreased by about 2 to 3 orders of magnitude. The ratio of BLM signal to energy deposition in the collimator jaws only increased by a factor of maximum 4 for a positive (for definition see Fig. 5.21) variation of the beam-jaw angle. There was no significant drop of the ratio for negative beam-jaw angles. As the ratio of BLM signal to energy deposition in the collimator jaws increases considerably for positive beam-jaw angles, it is recommendable to operate collimators with a slightly negative beam-jaw angle to absorb more energy in the collimators without a premature exceeding of BLM thresholds.

Summarizing the two studies above, the variation of the impact parameter and the beam-jaw angle for beam protons show that the ratio of BLM signal to energy deposition in the collimator jaws can be safely assessed for protons by using the lowest calculated ratios. The ratios vary over selected ranges at most by a factor of 4.

Not only beam protons but also secondary particles generated in upstream collimators impinge on a collimator. Ratios of BLM signal to energy deposition in the collimator jaws from mixed particle spectra, which origin from upstream collimators, were compared to ratios resulting from impinging protons. For the simulated cases it was found that the mixed particle spectra resulted in ratios which were at most by a factor of 4 lower compared to simulations with protons. The energy deposition in the collimators due to secondary particles from upstream collimators contributes significantly to the total energy deposition in a collimator (other than the first primary collimator). A few preliminary simulations for energy deposition due to upstream secondary particles have been done in this work. The ratios should be

Conclusions

systematically calculated by the implementation of the entire cleaning insertions in FLUKA, see [Mag06].

Peak energy densities in collimator jaws were investigated for beam impact distributions of typical failure cases. The ratios of BLM signal to peak energy deposition decrease for TCP's and TCSG's for smaller mean impact parameters by a factor of maximum 10 for both IC and SEM detector.

Uncertainties of BLM signals at LHC collimators have been investigated by comparing measured BLM signals with simulations and by simulating different impact scenarios and BLM misalignment. These uncertainties should be considered to assess BLM thresholds at LHC collimators conservatively.

A. Acronyms

ADC : Analog-to-Digital Converter

BLM : Beam Loss Monitoring

BLMTC : BLM Threshold Comparator card/data acquisition board

BPM : Beam Position Monitor

CC : Carbon Fiber-reinforced Graphite (also CFC)

CERN : Conseil Européen pour la Recherche Nucléaire – European Organization for Nuclear Research

CFC : Current-to-Frequency Converter

cms : Center-of-Mass System

EM : Electromagnetic

ED : Energy Deposition

FLUKA : Fluktuerende Kaskade – a multi-purpose Monte Carlo tracking code

hA : hadron-nucleus (interaction)

HEP : High Energy Physics

hN : hadron-nucleon (interaction)

IC : Ionization Chamber

IC1A : Ionization Chamber from series A located directly behind the LHC collimator, mounted vertical

IC1B : Ionization Chamber from series B located directly behind the LHC collimator, mounted parallel to the beam

IR : Insertion Region

LHC : Large Hadron Collider

LSS05 : SPS Long Straight Section No. 5

MD : Machine Development Session (for this work there were two in week 45 and 45 in 2007, and one in week 28 in 2008)

NN : nucleon-nucleon

A. Acronyms

PDF : Probability Density Function
ploc : Protons Lost On Collimator
pn : proton-neutron
poc : Protons (impacting) On Collimator
pp : proton-proton
RF : Radio Frequency
rms : Root Mean Squared
RS : Running Sum
SEM : Secondary Emission Monitor
SPS : Super Proton Synchrotron
TCLA : Absorber for Showers in Cleaning Insertions
TCP : Primary Collimator
TCSG : Secondary Graphite Collimator (Phase 1)
TCT : Tertiary Collimator
QFT : Quantum Field Theory
QPS : Quench Protection System

B. Hadronic and Intra Nuclear Interactions

This paragraph describes general aspects of the models for nuclear interactions in Monte Carlo particle codes. A more elaborate description can be found in literature such as [Fer96b, Fer96a, Bur95].

Using sophisticated, slow models for complex nuclear interactions to produce tabulated values of energy-angle spectra of all emitted particles for a fine and wide mesh of energies for all projectiles becomes soon very impracticable, due to storage size and the need of the complete recalculation of the tables for minor changes. Yet, tabulation can be convenient when applied to restricted energies and particle types, e.g. for low energy neutrons (see below).

An alternative approach to tabulation is the online simulation of interactions by Monte Carlo methods, predicting interactions for whatever projectile-target combination at a reasonable time without prior input.

Inelastic hadron-nucleus (hA) interactions are very complex processes. In Monte Carlo particle codes they are mostly modeled as a cascade of two-body interactions in the nucleus. Models of present-day Monte Carlo codes base often on extended and updated versions of the pioneering Bertini Intra Nuclear Cascade (INC) model, originating in the 40ties [Fer96b]. This type of modeling proved widely applicable for hadron-nucleon (hN) interactions ranging from the π -production threshold to high energies. Modern INC models enlarge their regime of validity by accounting for several quantum mechanical effects [Fer97].

Depending on the projectile energy there are generally two families of models employed for the excess hN interactions. There are those based on individual resonance particle production and decays, covering ranges up to some GeV, and the ones based parton/quark string models for higher energies. Additionally, there is a family of models used for the low-energy scale of hadronic interactions.

Resonance Particle Production

Pion-production is the first non-elastic channel to both π -nucleon and nucleon-nucleon interactions [Fer96b]. This is of course due to their small mass m_π of approximately 140 MeV. The nucleon-nucleon reaction, $N_1 + N_2 \rightarrow N'_1 + N'_2 + \pi$, has its threshold around 290 MeV¹, and starts to be important from about 700 MeV. The π -nucleon reaction, $\pi_1 + N \rightarrow \pi'_1 + \pi'_2 + N'$, starts at 170 MeV. These processes are often described via a fast-decaying intermediate Δ or N^* -resonance states, e.g.:

$$N_1 + N_2 \rightarrow N_1 + \Delta(1232) \rightarrow N'_1 + N'_2 + \pi . \quad (\text{B.1})$$

Multiple particle creation processes are consequently described by several resonance states.

¹More exactly, for a free nucleon it is around 290 MeV, for a bound one it is about 200 MeV due to Fermi motion.

B. Hadronic and Intra Nuclear Interactions

Generally speaking, all reactions can be thought to proceed via channels with fast-decaying resonances [Fer96b], such as:

$$h + N \rightarrow X \rightarrow x_1 + \dots + x_n \quad (\text{B.2})$$

$$h + N \rightarrow X + Y \rightarrow x_1 + \dots + x_n + y_1 + \dots + y_n \quad (\text{B.3})$$

...

Here, X, Y are resonances or stable particles, x_i, y_i are the particles leaving the reaction. Evidently, also elastic reactions or electromagnetic processes can be described in this scheme. For a systematic treatment of hN processes in such a scheme, all hN cross-sections must be decomposed in channels like the ones in Eqs. B.2 and B.3. Further, the relative angular distribution of the resonances in Eq. B.3, the decay branching ratios, and possibly anisotropic decay matrix elements must be known for all resonances [Fer96b]. Unfortunately, experimental data about exclusive channels is far from complete. A reasonable description can be achieved by supplementing the experimental information by isospin decomposition, see [Fer96b]. This kind of inelastic interaction modeling is valid up to a few GeV.

Quark/String theory-inspired Modeling

When the incident hadron energy exceeds a few GeV, the description of nonelastic interactions as a quasi two-body interaction with the formation of decay resonances starts to be less precise. The number of resonances which has to be considered growth exponentially and the exact properties of the resonances are often not precisely known. Produced particles start reflecting the motions of internal constituents, valence and sea quarks, of the hadrons. To describe this energy regime, generally phenomenologic methods with physical motivations are employed. The momentum-energy distributions of the constituents must be specified and string theory-inspired models, such as the Dual Parton Model (DPM) and the Quark-Gluon-String-Model plus an adequate hadronization model [Fer96a, Fer02] calculate the outcome of such interactions.

Preequilibrium, Evaporation, Fission, and Nuclear Break-up Stage

At energies below the π -production threshold so-called *preequilibrium* models are widely employed [Fer96b]. At the very end of a projectile reaction chain, the *evaporation, fission, and nuclear break-up stage*, nuclei are characterized by their excitation energies. This final stage is crucial for the amount of residual nuclei produced. The system is in an equilibrium state, where the excitation energy is shared by a large number of nucleons. When the excitation energy is higher than the separation energy of a nucleus, light fragments, such as α 's, d's, ^3H , and ^3He , can be emitted. With average energies of some MeV, these particles constitute the bulk of emitted particles. The process of emission can be well described as the evaporation from a hot system [Fer96a]. The residual excitation energy sometimes also leads to the collective deformation of a nucleus. When the potential energy of this deformation surpasses the energy of the fission barrier, mostly two heavy fragments are produced. The fission barrier roughly scales with the fissility parameter Z^2/A . Fission can be neglected for most practical calculations for nuclei with $Z < 70$. Probabilities for fission and evaporation can be described by relatively simple formulas [Fer02]. At this stage, due to the Coulomb barrier the production of neutrons is favored over charged particle emission, particularly for medium and heavy nuclei. For very light nuclei the excitation energy may easier exceed the total binding

B. Hadronic and Intra Nuclear Interactions

energy, this leads to the so-called Fermi Break-up which can be treated by a statistical fragmentation model [Fer96b, Fer97]. The evaporation process is generally continued as far as energetically possible. At the end of this energy scale, the branching ratio for de-excitation by γ -emission becomes more and more important.

Experimental Data

For hadronic interactions below about 150 MeV, and this restricts for most practical applications to neutrons, huge sets of highly precise measurements exist, often supplemented by sophisticated modeling (ENDF-B, JEF, JENDL, etc.). Nucleon interactions at this energy range can be accurately described either by models or experimental information. As mentioned in Chapter 2, a good description of these interactions is crucial for the accurate prediction of shower tails.

C. Random Numbers

Random numbers are at the very basis of every Monte Carlo simulation. In this work they were used for example to generate different initial beam distributions. There are basically two types of random variables: *true random numbers* and *pseudo-random numbers*. The first match the theoretical postulation, they follow no scheme and are unpredictable. For instance, they can be generated by the white noise of an electric circuit or by the decay of single radioactive atoms. For practical reasons computation relies heavily on *pseudo-random numbers*. These ones are generated by an implemented mathematical algorithm, starting with an initial set of random variables, the *seed*. Thus, they have a deterministic behavior and do not fulfill the strong requirements of *true random numbers*. Yet, if the used mathematical algorithm is good, *pseudo-random numbers* show the same statistical properties as real ones. Both low correlation and the possibility of generating a virtually infinite number of random variables are assured by such algorithms. For most practical purposes, such as Monte Carlo applications, *pseudo-random numbers* are favorable over *true random numbers* since they do not require an external acquisition hardware, which would also involve routine checks for the quality of such variables, as they could be biased by technical defects. Moreover, the algorithmic generation of random numbers is computationally less demanding and allows for reproducibility of simulations (using the same *seed*), yielding tremendous simplifications in debugging a simulation code.

Monte Carlo codes need to sample random numbers distributed according to some, a priori arbitrary, probability density function (PDF). To do so, usually a *pseudo-random number generator* is employed sampling uniformly distributed random numbers between 0 and 1. These uniform random numbers then have to be converted into random numbers distributed according to the PDF's determined by the problem. Let R be the uniformly distributed random number between 0 and 1, and $f(x)$ an arbitrary PDF, thus having the properties $0 \leq f(x) \leq 1$ and $\int_{-\infty}^{\infty} f(x) = 1$. Further, let $F(x)$ be its cumulative distribution function, i.e., its integral. $F(x)$ is an increasing function with values between 0 and 1. By setting

$$F(x) = R \tag{C.1}$$

and solving for x , one obtains a random number x distributed in the desired way. The plausible proof is sketched in the following. Assuming Eq. C.1, one can show that for a fixed x_0 , the probability of $x < x_0$ is equal $F(x_0)$ according to following chain of equations:

$$P[x < x_0] = P[F(x) < F(x_0)] = P[R < F(x_0)] = F(x_0) . \tag{C.2}$$

The first equality follows from the fact that $F(x)$ is monotonically increasing, the second one simply by assuming Eq. C.1, and the last one is because R is uniformly distributed between 0 and 1.

It is shown that starting with uniformly random numbers from generators one can obtain by simple mathematic operations arbitrarily distributed random numbers, provided that the inverse of Eq. C.1 is analytically obtainable. Even if this is not the case, there is a repertoire

C. Random Numbers

of transformations leading to the wanted PDF's, yet these are beyond the scope of this paragraph and can be found in dedicated literature.

D. Gaussian Distributions

A normalized Gaussian function is given by

$$G(x) = \frac{1}{\sigma\sqrt{2\pi}} e^{-(x-\mu)^2/2\sigma^2}, \quad (\text{D.1})$$

with the mean value μ and the standard deviation σ .

To obtain the half-maximum points of $G(x)$, one has to solve the equation

$$G(x_{1/2}) = G(\mu) \quad (\text{D.2})$$

for $x_{1/2}$ and finds

$$x_{1/2} = \pm\sqrt{2\ln 2}\sigma + \mu. \quad (\text{D.3})$$

Thus, the full width at half maximum is given by

$$\text{FWHM} \equiv 2|x_{1/2} - \mu| = 2\sqrt{2\ln 2}\sigma \approx 2.3548\sigma. \quad (\text{D.4})$$

Double Gaussian

We look at two superimposed unnormalized Gaussians with the same mean value μ given by the formula

$$G_2(x) = R \cdot e^{-(x-\mu)^2/2\sigma_1^2} + (1-R) \cdot e^{-(x-\mu)^2/2\sigma_2^2}, \quad (\text{D.5})$$

where R is the ratio of the two Gaussians, and $\sigma_{1,2}$ their respective standard deviations.

The overall standard deviation σ of G_2 is then given by

$$\sigma = \frac{A_1\sigma_1 + A_2\sigma_2}{A_1 + A_2}, \quad (\text{D.6})$$

where $A_i = \sqrt{2\pi}\sigma_i R_i$ is the area under each Gaussian, with $R_1 = R$, and $R_2 = (1-R)$. Thus, we find that

$$\sigma = \frac{R\sigma_1^2 + (1-R)\sigma_2^2}{R\sigma_1 + (1-R)\sigma_2}. \quad (\text{D.7})$$

F. Conversion of the BLM Detector Signals

The signal of the BLM's is given by the CFC front-end electronics in number of digitalization intervals (bits) $N_{\text{bit}}^{\text{RS}i}$ in a RS time interval Δt_i (see Tab. 4.2). The number of charges deposited in a BLM per bit are [Sto07]

$$\Delta Q = 1.95 \cdot 10^{-13} \frac{\text{C}}{\text{bit}} . \quad (\text{F.1})$$

Thus, bits given by the electronics in a time interval are converted in dose in this time interval by

$$D_{\text{IC,SEM}}^{\text{RS}i} = \left(\frac{dD}{dQ} \right)_{\text{IC,SEM}} \cdot \Delta Q \cdot N_{\text{bit}}^{\text{RS}i} . \quad (\text{F.2})$$

For an IC, the ratio of dose per charge is given by

$$\left(\frac{dD}{dQ} \right)_{\text{IC}} = \frac{E_{\text{W}}}{\rho_{\text{N}_2} \cdot V_{\text{sen}} \cdot e_o} = 18.5 \pm 1.9^3 , \quad (\text{F.3})$$

with the density of the detector gas ρ_{N_2} , the sensitive volume of the chamber V_{sen} , the W-factor E_{W} (see Sec. 4.1), and the elementary charge e_o . For the SEM chamber an equivalence of dose-per-charge ratio of

$$\left(\frac{dD}{dQ} \right)_{\text{SEM}} = 1.31 \pm 0.14 \cdot 10^9 \quad (\text{F.4})$$

was determined by calibrating its response with an air-filled chamber of the same size, see [Kra08].

The bits-to-dose factors evaluate to

$$D_{\text{IC}}^{\text{RS}i} = 3.62 \cdot 10^{-9} \frac{\text{Gy}}{\text{bit}} \cdot N_{\text{bit}}^{\text{RS}i} , \quad (\text{F.5})$$

$$D_{\text{SEM}}^{\text{RS}i} = 2.56 \cdot 10^{-4} \frac{\text{Gy}}{\text{bit}} \cdot N_{\text{bit}}^{\text{RS}i} . \quad (\text{F.6})$$

G. Beam Optics and TWISS Functions

This paragraph gives a quick summary of formulas describing accelerator physics for transverse beam dynamics as they are of concern for this work. Complementary information can be found in [Syp04, Wie07, Cha06].

In the following a beam reference system where the s -axis points downstream, the x_2 -axis lies in the vertical plane, and the x_1 -axis lies in the horizontal plane pointing away from the center of the ring will be used as illustrated in Fig. G.1. In case that no coordinate indices are given, formulas are valid for both x_1 and x_2 -direction, e.g. x refers to x_1 and x_2 , ϵ refers to ϵ_1 and ϵ_2 . $\Delta x(s)$ denotes the deviation from the central orbit at point s .

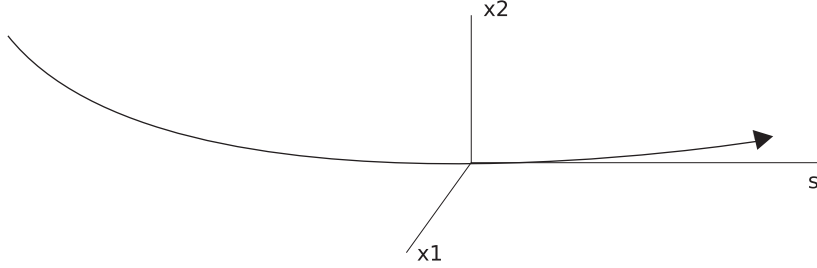


Fig. G.1.: Beam reference coordinate system.

The trajectory of a particle traveling along the center orbit with an amplitude $x(s)$ is given by

$$x(s) = \sqrt{\beta(s)}\sqrt{\epsilon} \sin(\psi(s) + \delta) , \quad (\text{G.1})$$

where β is the well known betatron function, δ is the phase offset, and $\psi(s)$ is the phase advance.

The rms normalized emittance is denoted by

$$\epsilon_N \equiv \epsilon_N^{\text{rms}} = \epsilon^{\text{rms}} \cdot (\gamma_L \beta_L) \quad (\text{G.2})$$

Assuming a particle with a momentum deviation of Δp (emittance is zero), the relation defining the *dispersion function* $D(s)$ is given by

$$\Delta x(s) = D(s) \frac{\Delta p}{p} , \quad (\text{G.3})$$

where $\frac{\Delta p}{p}$ is the momentum spread.

Assuming no dispersion in x_2 , the standard deviation σ at a point s is given by

$$\langle x_1^2 \rangle^{\frac{1}{2}} = \sigma_1 = \sqrt{\frac{\epsilon_{N,1} \beta_1}{\pi (\gamma_L \beta_L)} + D_1^2 \left(\frac{\Delta p}{p} \right)^2} \quad (\text{G.4})$$

G. Beam Optics and TWISS Functions

and

$$\langle x_2^2 \rangle^{\frac{1}{2}} = \sigma_2 = \sqrt{\frac{\epsilon_{N,2}\beta_2}{\pi(\gamma_L\beta_L)}}, \quad (\text{G.5})$$

where β_L is the velocity as a fraction of the speed of light and $\gamma_L = (1 - \beta_L^2)^{1/2}$.

H. Beam Profile by Scraping: Dispersive Case

Considering also dispersion the functional form of the beam profile is more complicated. The scraping element will remove all particles that have a maximum excursion larger than the distance r_0 between scraper and beam center. The fraction of particles scraped by a collimator, which is a distance $r - x_0 = n_\sigma \sigma_x$ from the beam center, is given by the following integral:

$$F_{L,\text{disp}}(n_\sigma) = 1 - \left(\int_{x_0}^{\sigma_x n_\sigma + x_0} dr \int_0^{\frac{\sigma_x n_\sigma + x_0 - r}{D}} dr_p \cdot \rho_\beta(r) \rho_p(r_p) \right). \quad (\text{H.1})$$

When we assume that the synchrotron amplitude distribution ρ_p is Gaussian of the form

$$\rho_p(r_p) = \frac{r_p}{\sigma_p^2} e^{-\frac{1}{2}(r_p)^2/\sigma_p^2}, \quad (\text{H.2})$$

the integral can be expressed analytically in terms of error functions.

Bibliography

- [Alo06a] A. Gómez Alonso, *Most probable failures in LHC magnets and time constants of their effects on the beam*, CERN-LHC-Proj.-Note-389, 2006
- [Alo06b] A. Gómez Alonso, *Impact distribution of the beam losses at the LHC collimator in case of magnet failures*, CERN-LHC-Proj.-Note-410, 2006
- [Alo08] A. Gómez Alonso, *Private communications*, Dissertation in prep., CERN, 2008
- [Ass06] R. Assmann, *et al.*, *The final collimation system for the LHC*, CERN-LHC-Proj.-Report-919, 2006
- [Ass08] R. Assmann, *Private communications*, CERN, 2008
- [Blu93] W. Blum, E. Rolandi, *Particle detection with drift chambers*, Springer Verlag, ISBN 978-3-540-76683-4, 1993
- [Boc98] R.K. Bock, A. Vasilescu, *The particle detector briefbook*, European Physical Society, ISBN 978-3-540-64120-9, 1998
- [Boc08] D. Bocian, *Private communications*, Technical notes in prep., CERN, 2008
- [Bru08] M. Brugger, *Private communications*, CERN, 2007-08
- [Bur95] W.E. Burcham, M. Jobes, *Nuclear and particle physics*, Prentice Hall, ISBN 978-0-582-45088-2, 1995
- [Bur04] H. Burkart, R. Schmidt, *Intensity and luminosity after beam scraping*, CERN-AB-2004-032-ABP, 2004
- [Cha06] A. Wu Chao, M. Tigner, *et al.*, *Handbook of accelerator physics and engineering*, 3rd Printing, World Scientific, ISBN 978-981-02-3500-3, 2006
- [Col] LHC Collimation Homepage, <http://lhc-collimation-project.web.cern.ch/lhc-collimation-project/>
- [Deh02] B. Dehning, *et al.*, *LHC Beam loss monitor system design*, Proceedings of the Beam Instrumentation Workshop 2002: Tenth Workshop, American Institute of Physics, p.229, 2002
- [Flu] FLUKA Homepage, <http://www.fluka.org/>
- [Fas03] A. Fassò, A. Ferrari, J. Ranft, P.R. Sala, *The physics models of FLUKA: status and recent developments*, Computing in High Energy and Nuclear Physics 2003 Conference (CHEP2003), USA, 2003

Bibliography

- [Fas05] A. Fassò, A. Ferrari, J. Ranft, P.R. Sala, *FLUKA: a multi-particle transport code*, CERN-2005-10, INFN/TC_05/11, SLAC-R-773, 2005
- [Fer96a] A. Ferrari, P.R. Sala, *Physics of showers induced by accelerator beams*, Lecture, INFN, Italy, 1996
- [Fer96b] A. Ferrari, P.R. Sala, *The physics of high energy reactions*, Expanded lecture, INFN, Italy, 1996
- [Fer97] A. Ferrari, A. Fassò, *et al.*, *New developments in FLUKA modelling of hadronic and EM interactions*, in Proceedings of SARE-3, KEK-Tsukuba, KEK Report Proceedings 97-5, 32, 1997
- [Fer02] A. Ferrari, P.R. Sala, *Nuclear reactions in Monte Carlo codes*, 13th Symposium on Microdosimetry, Stresa, 2002
- [Fil05] R. Filippini, B. Dehning, *et al.*, *Reliability assessment of the LHC machine protection system*, CERN-LHC-Proj.-Report-812, 2005
- [Fri02] W. Friesenbichler, *Development of the readout electronics for the beam loss monitors of the LHC*, CERN-THESIS-2002-28, 2002
- [Ges02] E. Gschwendtner, *et al.*, *The beam loss detection system of the LHC ring*, CERN-SL-2002-021-BI, 2002
- [Hol05] E.B. Holzer, *et al.*, *Beam loss monitoring system for the LHC*, NSS Conference Record, IEEE, Vol.2:1052-56, 2005
- [Kai05] V. Kain, *Machine protection and beam quality during the LHC injection process*, CERN-THESIS-2005-047, 2005
- [Kno00] G.F. Knoll, *Radiation detection and measurement*, John Wiley & Sons, ISBN 978-0471073383, 2000
- [Kra07] D. Kramer, *et al.*, *Very high radiation detector for the LHC BLM system based on secondary electron emission*, NSS Conference Record, IEEE, Vol.3:2327-2330, 2007
- [Kra08] D. Kramer, *Design and implementation of a detector for high flux mixed radiation fields*, Dissertation in prep., CERN, 2008
- [Kur03] I.A. Kurochkin, J.B. Jeanneret, *et al.*, *Simulation of a signal in the beam loss monitors of the momentum cleaning for the new collimator design*, Internal note, CERN, 2003
- [LHC03] CERN, *The LHC design report, vol. I: the LHC main ring*, Technical Report CERN-2004-003, 2003
- [Mag06] M. Magistris, *et al.*, *FLUKA simulations for the optimization of the beam loss monitors*, CERN-AB-Note-2008-038, 2006
- [Mni04] J. Mnich, *Elementarteilchenphysik*, <http://www.physik.rwth.aachen.de/~roth/eteilchen/ETeilchen.pdf>, 2004

Bibliography

- [PDG06] Particle Data Group, *Review of particle physics*, Institute of Physics Publishing, <http://pdg.lbl.gov>, 2006
- [Rob06] G. Robert-Demolaize, *Design and performance optimization of the LHC collimation system*, CERN-THESIS-2006-069, 2006
- [RPP92] *Review of Particle Properties*, Phys. Rev. D45, 1992
- [RUM79] Seventh International Commission on Radiation Units and Measurements, *Average energy required to produce an ion pair*, ICRU Report 31, USA, 1979
- [Sar07] L. Sarchiapone, *et al.*, *FLUKA Monte Carlo simulations and benchmark measurements for the LHC beam loss monitors*, Nucl. Instrum. Methods Phys. Res., A 581 (2007) 511-516, 2007
- [Sal07] P.R. Sala, M. Brugger, *Private communications & notes*, CERN, 2007
- [Sch06] R. Schmidt, R. Assmann, B. Dehning, *et al.*, *Protection of the CERN Large Hadron Collider*, New Journal of Physics 8, 290, 2006
- [Sei94] M. Seidel, *The Proton Collimation System of HERA*, Dissertation, DESY 94-103, 1994
- [Sto07] M. Stockner, *Beam loss calibration studies for high energy proton accelerators*, Dissertation, CERN, 2007
- [Syp04] D.A. Edwards, M.J. Syphers, *An introduction to the physics of high energy accelerators*, Wiley-VCH, ISBN 978-0-471-55163-8, 2004
- [Ver03] A. Vergara-Fernandez, *Reliability of the quench protection system for the LHC superconducting elements*, CERN-THESIS-2004-019, 2003
- [Wei07] Th. Weiler, R. Assmann, *et al.*, *Beam loss response measurements with an LHC prototype collimator in the SPS*, Internal note, CERN, 2007
- [Wie07] H. Wiedemann, *Particle accelerator physics I&II*, Springer, ISBN 978-3540490432, 2007
- [Zam05] C. Zamantzas, E. Effinger, G. Feroli, *et al.*, *The LHC beam loss monitoring system's real-time data analysis card*, CERN-AB-2005-082, 2005
- [Zam06] C. Zamantzas, *The real-time data analysis and decision system for particle flux detection in the LHC accelerator at CERN.*, CERN-THESIS-2006-037, 2006